Sigve Hovda

New Doppler-Based Imaging Methods in Echocardiography with Applications in Blood/Tissue Segmentation

Thesis for the degree philosophiae doctor

Trondheim, May 2007

Norwegian University of Science and Technology
Faculty of Information Technology, Mathematics
and Electrical Engineering
Department of Computer and Information Science

NTNU
Norwegian University of Science and Technology

Thesis for the degree philosophiae doctor

Faculty of Information Technology, Mathematics and Electrical Engineering
Department of Computer and Information Science

ISBN 978-82-471-2047-7 (printed version)
ISBN 978-82-471-2050-7 (electronic version)
ISSN 1503-8181

Doctoral theses at NTNU, 2007:93

Printed by NTNU-trykk

Abstract

This document is laid out as follows: Part I contains a general introduction to echocardiography. Part II and III cover new material in this thesis and their abstracts are listed below. The material in part II and part III are basically the same as the material in the two papers in part V. Both papers are accepted for publication in conference proceedings of Medical Imaging and Informatics in Beijing, China. This conference takes place in August this year and I am pleased to be invited to deliver an oral presentation. In part II and III, text, figures, and equations are given more space. In part IV four appendices are listed; Appendix A covers a derivation of spectral parameters of the ultrasound Doppler signal, Appendix B covers a discussion of the classification criteria, Appendix C covers a discussion of the effect of reverberations from previous shots and Appendix D contains some images of the new imaging modes. For your convenience, a list of symbols used in this thesis is added after the bibliography.

Part II: The bandwidth of the ultrasound Doppler signal is proposed as a classification function of blood and tissue signal in transthoracial echocardiography of the left ventricle. The new echocardiographic mode, Bandwidth Imaging, utilizes the difference in motion between tissue and blood. Specifically, Bandwidth Imaging is the absolute value of the normalized autocorrelation function with lag one. Bandwidth Imaging is therefore linearly dependent on the the square of the bandwidth estimated from the Doppler spectrum. A 2-tap Finite Impulse Response high-pass filter is used prior to autocorrelation calculation to account for the high level of DC clutter noise in the apical regions. Reasonable pulse strategies are discussed and several images of Bandwidth Imaging are included. An in vivo experiment is presented, where the apparent error rate of Bandwidth Imaging is compared with apparent error rate of Second-Harmonic Imaging on 15 healthy men. The apparent error rate is calculated from signal from all myocardial wall segments defined in [1]. The ground truth of the position of the myocardial wall segments is determined by manual tracing of endocardium in Second-Harmonic Imaging. A hypotheses test of Bandwidth Imaging having lower apparent error rate than Second-Harmonic Imaging is proved for a p-value of 0.94 in 3 segments of end diastole and 1 segment in end systole on non averaged data. When data is averaged by a structural element of 5 radial, 3 lateral and 4 temporal samples, the numbers of segments are increased to 9 in end diastole and to 6 in end systole. These segments are mostly located in apical and anterior wall regions. Further, a global measure GM is defined as the proportion

of misclassified area in the regions close to endocardium in an image. The hypothesis test of Second-Harmonic Imaging having lower GM than Bandwidth Imaging is proved for a p-value of 0.94 in the four-chamber view in end systole in any type of averaging. On the other side, the hypothesis test of Bandwidth Imaging having lower GM than Second-Harmonic Imaging is proved for a p-value of 0.94 in long-axis view in end diastole in any type of averaging. Moreover, if images are averaged by the above structural element the test indicates that Bandwidth Imaging has a lower apparent error rate than Second-Harmonic Imaging in all views and times (end diastole or end systole), except in four-chamber view in end systole. This experiment indicates that Bandwidth Imaging can supply additional information for automatic border detection routines on endocardium.

Part III: Knowledge Based Imaging is suggested as a method to distinguish blood from tissue signal in transthoracial echocardiography. This method utilizes the maximum likelihood function to classify blood and tissue signal. Knowledge Based Imaging uses the same pulse strategy as Bandwidth Imaging, but is significantly more difficult to implement. Therefore, Knowledge Based Imaging and Bandwidth Imaging are compared with Fundamental Imaging by a computer simulation based on a parametric model of the signal. The rate apparent error rate is calculated in any reasonable tissue to blood signal ratio, tissue to white noise ratio and clutter to white noise ratio. Fundamental Imaging classifies well when tissue to blood signal ratio is high and tissue to white noise ratio is higher than clutter to white noise ratio. Knowledge Based Imaging classifies also well in this environment. In addition, Knowledge Based Imaging classifies well whenever blood to white noise ratio is above 30 dB. This is the case, even when clutter to white noise ratio is higher than tissue to white noise ratio and tissue to blood signal ratio is zero. Bandwidth Imaging performs similar to Knowledge Based Imaging, but blood to white noise ratio has to be 20 dB higher for a reasonable classification. Also the highpass filter coefficient prior to Bandwidth Imaging calculation is discussed by the simulations. Some images of different parameter settings of Knowledge Based Imaging are visually compared with Second-Harmonic Imaging, Fundamental Imaging and Bandwidth Imaging. Changing parameters of Knowledge Based Imaging can make the image look similar to both Bandwidth Imaging and Fundamental Imaging.

Preface

This thesis is submitted to the Faculty of Information Technology, Mathematics and Electrical Engineering at the Norwegian University of Science and Technology NTNU, in partial fulfillment of the degree; PhD. The work has primarily been done at the Department of Computer and Information Science at NTNU. A collaboration with General Electric Vingmed Ultrasound AS has been present, allowing the use of Ultrasonic devices such as scanners and software. The start time of the thesis was may 1999, although the main focus of the thesis changed dramatically during 2003. The present material is therefore from the work carried out during the four last years. The work has been financially supported by the Research Council of Norway and Department of Computer and Information Science at NTNU.

Acknowledgement

There are many people who need to be acknowledged for their support and guidance. First of all, Associate Professor Bjørn Olstad has been my supervisor and had the overall responsibility. He has contributed with his enthusiasm and ideas. His guidance has been invaluable, especially in the design of the in vivo validation experiment.

Professor Håvard Rue has been co supervisor in the project and he has been very helpful on the statistical parts of the thesis. I also thank him for his advises on how to structure the writing process.

There are many at both GE Vingmed Ultrasound AS and at Department of Circulation and Medical Imaging that have been very helpful in making this thesis possible. In particular, I mention Sigmund Frigstad at GE Vingmed Ultrasound AS for his support and guidance related to the scanner. His help has extended for many years. Further, I thank PhD stipendiate Brage Høyem Amundsen for clinical advises and for performing the echocardiographic examinations in the in vivo experiment.

At the Department of Computer and Information Science, I particularly thank Kjell Bratbergsengen, Bård Kjos and Jørn Hokland. I also thank Tore Jørgensen and Solfrid Bergsmyr at the faculty for their special follow-up.

There are also many colleagues that have contributed on both professional and personal level. I mention here Bjarne Bergheim, Siri Malm, Marius Grannæs, Asbjørn Djupdal, Morten Hardman, Fredrik Orderud and Magnus Jahre.

Several personal friends have been important to me in this period as well. I mention here in no particular order, Benn Folkvord, Hansi Nilsen, Pål Dåstøl, Tor Erik Nysæter, Ingrid Kåsi, Line Wulfsberg, Tarek Yousef, Stian Solbakken, Peter Johansson, Morten Bjorland, Lena Kvalevåg, Audun Aspelund, Keith Munkejord and Kurt Freewald from USA, who tragically died in January 2006.

Further, I thank my girlfriend's family Anne Marie, Knut and Ørjan Pettersen and Hans Christian Myhre with family for their support and care.

I thank my father Ola, mother Ruth, brother Johan and sister Anne Lovise for their support and care. Finally, I thank Trine Merete Myhre, who I live, and share everything with. Her love makes me carry on.

Contents

Part I

Introduction

The field of echocardiography is broad, and this introduction covers a selected subset of the field that this thesis is build on. In section 1.1 an overview of the most important echocardiographic modes is given and the signal chains are described by flowcharts. The clinical aspects of echocardiography is limited to standard imaging views and the diagnose criteria ejection fraction. Finding ejection fraction involves defining endocardium either by manual tracing or by automatic routines. A brief overview of automatic endocardium tracking routines is given in section 1.3. In section 1.4 a software for handling ultrasound data is discussed briefly.

1.1 Echocardiography

The first use of ultrasound in medical applications was reported in the early fifties by Wild [2], Howrey and Bliss [3] and Edler and Hertz [4]. Echocardiography has evoluted enormously since then, motivated by the fact that heart failure and heart deceases are the most common causes of death in western countries.

In transthoracial echocardiography the probe has a center frequency ranging from 2.5 to 3.5 MHz, since the region of interest is up to 12-15 cm into the body. Bones and air in lungs are not penetrated by ultrasound at these frequencies. The view points are therefore limited dramatically and probes providing sector scan are usually preferred.

Various echocardiographic modes are available on conventional scanners. Examining the cardiac muscle, the amplitude of the pulse echo along one beam is visualized in motion-mode. The two dimensional image is called the beam-mode. In amplitude imaging, the modes Fundamental Imaging and Second-harmonic Imaging are available. Blood flow in the heart is examined by Continuous Wave Doppler, Pulsed Wave Doppler or Color Flow Imaging. Movement of myocardium is examined by Tissue Velocity Imaging (Tissue Doppler Imaging).

The next two subsections describes flowcharts for sector scan beam-mode amplitude imaging and Color Flow Imaging.

1.1.1 Amplitude imaging

The basic principle of ultrasound imaging is as follows; a voltage signal of a few oscillations in the MHz range is applied to a piezo-electric material, causing it to vibrate. For a multi element transducer each element transmits sphere pressure waves (sound waves) and in the far-field these sphere waves add up to a focused beam. After one pulse transmission the same elements absorbs the sound waves of the echoes of the transmitted pulse. Since the speed of sound is relatively constant in tissue and blood the time delay after pulse emission is used to distinguish signal from different depths. The radial resolution is half the pulse length and the lateral resolution is the beam width. The beam width can be shown to be linearly dependent of center frequency and depth. The beam width is also inversely dependent of the

transducer width. An electronically steered transducer controls the phase delays on each element, allowing control of the focal point along the beam and steering the beam in different directions. Modern systems can focus on every depth on reception, while only few focal points (usually one or two) can be used on transmission.

A flowchart of how the signal is processed is shown in Fig. 1.1(a). After the transducer elements have received a pulse and thereby created a voltage signal, the signal is digitalized. The beam former adds up time delayed signals from every element to obtain the desired focus. A bandpass filter with passband equal to the bandwidth of the emitted pulse is used to improve signal to noise ratio. In Second-Harmonic Imaging [5] the center frequency of this bandpass filter is doubled causing only the signal from non-linear scattering to pass. This type of imaging is reported to have better quality than Fundamental Imaging [6]. In particular, Second-Harmonic Imaging has lower side lobe levels and less reverberation noise.

The next step in the process is the time gain compensation TGC, which compensates for the attenuation from different depths. A detection algorithm finds the envelope of the signal and a quasi logarithmic amplifier increases the amplitude of the weaker signal. This is done so strong signal can be visualized with weak signal.

The flowchart has so far shown how signal from one range cell is channeled through the system. In order to show a two dimensional image, the signal from each range cell and from each beam is stored in a two dimensional array. When the array is filled up, the data is scan converted, meaning that the physical dimensions become correct. For a sector scan this involves a polar coordinate transformation. The data is color coded from black to white and then displayed. Fig.1.2(a) shows a transthoracial cardiac Second-Harmonic Image of a healthy mature male. The image consists of 193 reception beams at 400 depths and the frame rate was 44 frames per second.

1.1.2 Ultrasound Doppler measurements

When a sound wave is reflected from a moving scatterer the frequency of the reflected signal is changed from the transmitted frequency. The Doppler equation gives a relation between this frequency shift f_d and the velocity along the beam v_z;

$$v_z = -\frac{c}{2f_0} f_d \tag{1.1}$$

where c is speed of sound and f_0 is the center frequency of the probe. The first use of this effect was reported in 1957 by Satomura et. al. [7]. Jensen's book [8] and Angelsen's book [9] gives a thorough discussion of Doppler methods for blood velocity estimates on modern systems.

In Continuous Wave Doppler, this shift is measured directly. Typically one part of the transducer emits a continuous sound wave and the other part of the transducer receives the echoes of the emitted wave. The Doppler shift is small compared with the center frequency of the probe, since the speed of blood is small compared with

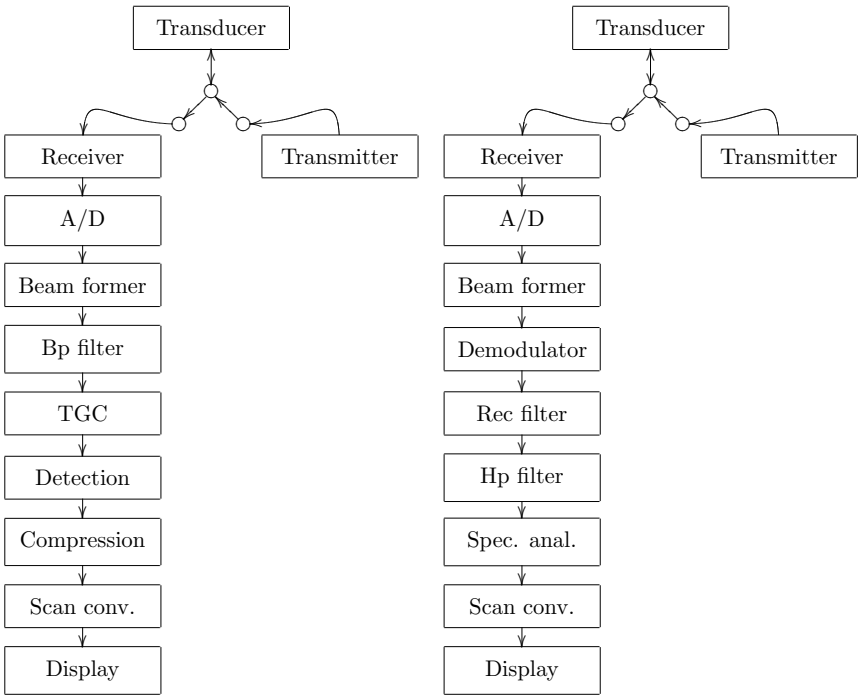

(a) Amplitude Imaging

(b) Tissue Velocity Imaging and Color Flow Imaging

Figure 1.1: Flowchart for amplitude imaging and Tissue Velocity Imaging/Color Flow Imaging systems. After the transducer elements have received a pulse and thereby created a voltage signal, the signal is digitalized. The beam former adds up signals from every element which are time delayed to obtain the desired focus. In amplitude imaging a bandpass filter with passband equal to the bandwidth of the emitted pulse is used to improve signal to noise ratio. The time gain compensator TGC, compensates for the attenuation from different depths and a detection algorithm finds the envelope of the signal and a quasi logarithmic amplifier increases the amplitude of the weaker signal. In Color Flow Imaging and Tissue Velocity Imaging the signal goes through the same process as in amplitude imaging until it is beam-formed. Afterward, the signal is complex demodulated and filtered through a rectangular receiver filter. The signal is highpass filtered before the spectral parameters ω_1, B, P is calculated. In Tissue Velocity Imaging ω_1 is calculated after a weak highpass filter. In order to show a two dimensional image, the signal from each range cell from every depth and every beam has to be stored in a two dimensional array. When this array is filled up, the data is scan converted, meaning that the physical dimensions become correct. The data is color coded and displayed.

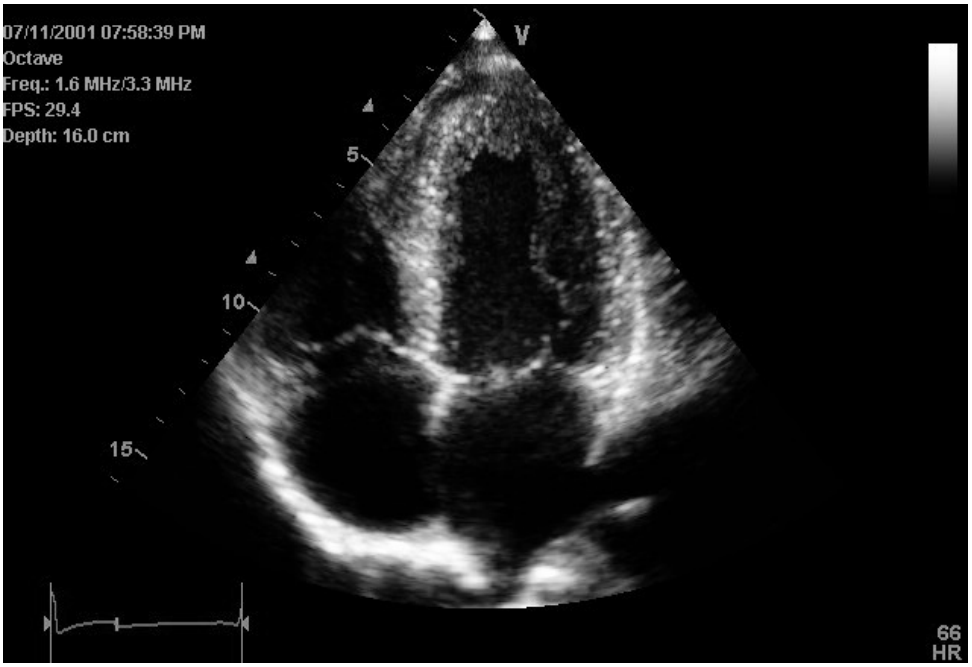

(a) Second-Harmonic Imaging

Figure 1.2: Second-Harmonic Imaging of a mature male.

speed of sound. Complex demodulation is done to transfer the passband signal to a baseband signal. A high pass filter removes the components from tissue and the desired blood velocities can be measured from the spectrum.

In Pulse Wave Doppler the transducer alternates from emitting and receiving pulses in the same manner as in amplitude imaging. Radial resolution is therefore possible. Since the transmitted pulses are short, the bandwidth is much broader than for Continuous Wave Doppler, and the frequency dependent attenuation distorts the signal more than the Doppler shift. In Pulse Wave Doppler the frequency shift is not measured directly. In fact signals from a number of pulses, consecutively shot in the same direction, are used to estimate the Doppler shift. Pulse Wave Doppler was first suggested by Baker and Watkins [10] in 1967.

Color Flow Imaging is essentially Pulsed Wave Doppler swept over a two dimensional sector. Color Flow Images was first shown by Namakawa [11] and Kasai [12].

The estimation techniques for blood velocities can be divided into narrow band and wide band methods. Narrow band methods use relatively long pulses and estimate the parameters from one range gate. Examples of this are the autocorrelation technique [12], Fourier based techniques and autoregressive modeling [13]. Wide band techniques use a train of short pulses to track a group of red blood cells using

the intensity of their echoes. Data from many range gates is used. Examples are the cross correlation routine [14], the sum absolute difference technique [15] and the wide band maximum likelihood estimator [16].

A flowchart for a typical narrow band Color Flow Imaging system is shown in Fig. 1.1(b). After the signal is received, digitalized and focused in the beam former, it is complex demodulated. This places the signal into the baseband and the directional information is kept. The receiver filter maximizes signal to noise ratio by having a rectangular impulse response with duration equal to the pulse length [17]. The radial length of the sample volume is increased by this filter.

At this point the data is stored in a buffer until all pulses in one beam direction have arrived this buffer. If eight pulses were used, meaning packet size eight, then eight samples are available for further processing. In fact these pulses are high pass filtered to remove clutter noise from slowly or non moving tissue. Torp [18] and Bjærum [19] have given a thorough discussion of highpass filters when the samples are few. After the estimators for power, bandwidth and mean frequency are calculated, the data is scanconverted and displayed. In Color Flow Imaging, velocities toward the probe is conventionally shown red and velocities away is shown blue. The intensity of the colors are dependent on the mean frequency shift. Broad bandwidth indicates disturbed flow and is visualized green. Fig.1.3(a) shows an Color Flow Image.

In Tissue Velocity Imaging, the flowchart is basically the same as for Color Flow Imaging. The pulse strategy is different and also the high pass filter prior to the calculation of the autocorrelation is much weaker or not present. The signal to noise ratio is significantly higher than in Color Flow Imaging, since the signal from tissue is much stronger than signal from blood. This allows a much shorter pulse transmission which increases radial resolution. Also a low packet size (often three) is sufficient and enables high frame rate. This is important for imaging the rapid movement of myocardium in the end systole. Furthermore, a beam interleaving method is used to keep a pulse repetition frequency low while frame rate high. Further, a low pulse repetition frequency enables non dangerously to emit more energy into the body per pulse resulting in stronger echoes. In some cases a weak high pass filter is used to subtract DC clutter noise from reverberations along the beam. Tissue Velocity Imaging and Color Flow Imaging are usually duplex, meaning that they are both shown together with an amplitude image (usually Second-Harmonic Image). An example of an Tissue Velocity Image is shown in Fig. 1.3(b).

1.2 Standard echo Doppler examination

Due to the fact that ultrasound can not penetrate oxygen in the lungs and bones, the positions of the probe placements are limited. The standard transthoracial imaging views of the left ventricle are left para-sternal, right para-sternal, supra-sternal, subcostal and apical positions. Explaining the diagnostic benefits of these views are

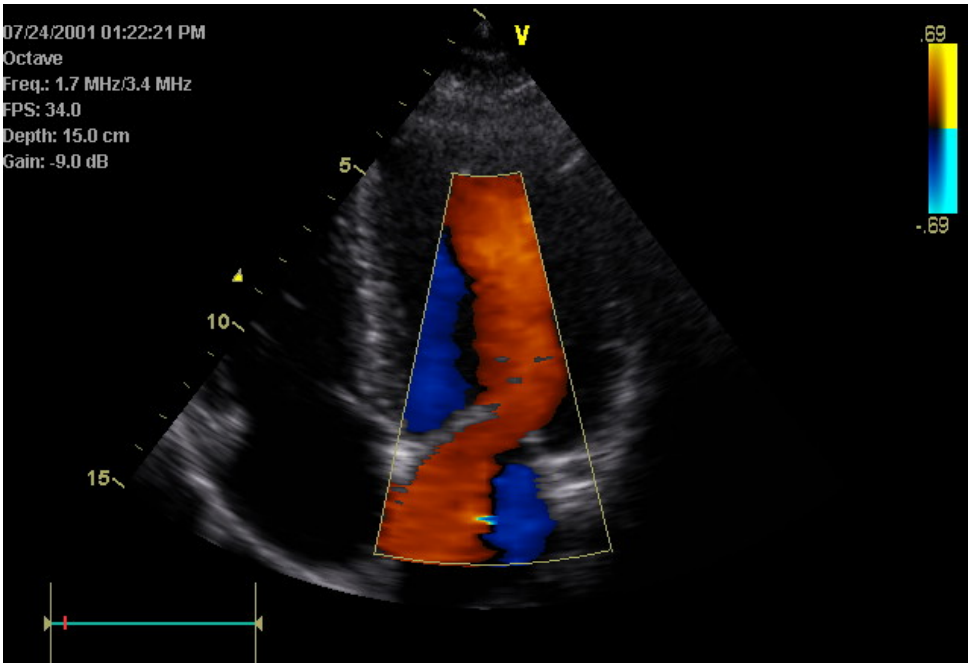

(a) Color Flow Image

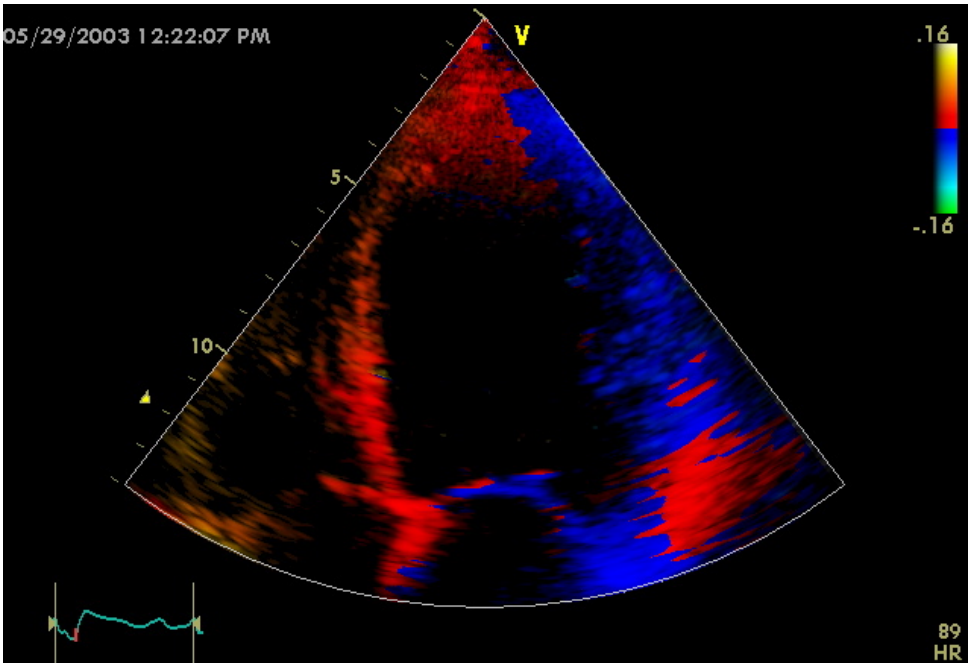

(b) Tissue Velocity Image

Figure 1.3: Ultrasound Color Flow Imaging and Tissue Velocity Imaging of a mature male.

not the scope of this thesis, but an overview is found in [20]. Particularly, the three apical views are interesting in this thesis. The three standard apical views are the four-chamber view, the two-chamber view and the long-axis view. These three views contain the long axis of the left ventricle and are rotated around the long axis with 60 degrees to each other. Together they give a very good overview of the heart.

Three simple sketches of the human heart, seen from four-chamber view, two-chamber view and long-axis view, are shown in Fig. 1.4(b), 1.4(c) and 1.4(d). These sketches are found in the documentation of GcMat described in section 1.4, and later manipulated. Here, left ventricle LV, right ventricle RV, left atria LA and right atria RA are marked. The valve between left ventricle and the atrial-ventricular plane AV is called the mitral valve and the valve between left ventricle and aorta AO is called the aortic valve.

Cerqueira et. al. [1] have given recommendations for nomenclature and standardized segmentation of myocardium. The sixteen segmentation model for echocardiography is shown in the bulls-eye diagram in Fig. 1.4(a).

The segments are found by slicing the ventricle into three thirds. The parallel slices have equal space between each other and are perpendicular to the left ventricle long-axis. These three slices are further divided into the final myocardial wall segments. The mid- and basal slices consist of six equally sized segments, while the apical slice consists of four segments. This can be seen in Fig. 1.4.

Ultrasonic imaging of the two-chamber view accesses basal anterior, mid anterior, apical anterior, apical inferior, mid inferior and basal inferior segments. The four-chamber view accesses basal inferoseptal, mid inferoseptal, apical septal, apical lateral, mid anterolateral and basal anterolateral segments. And the long-axis view accesses the basal anteroseptal, mid anteroseptal, apical septal, apical lateral, mid inferolateral and basal inferolateral. This segmentation model is used in chapter 3 in part II.

1.2.1 The ejection fraction

One of the most important diagnose criterias of coronary heart decease, valve deceases and heart failure is the ejection fraction. This is the ejected volume divided by the maximum volume of the left ventricle. Echocardiography is the most common tool to measure ejection fraction since it is noninvasive, cheap, accessible and thoroughly tested. The stress echo examination involves continuous imaging of the heart as the heart pulse is increased either by medicine or by activity. By stressing the heart the examiner measures ejection fraction at different levels of stress. To do this, the examiner has to draw the endocardial border manually in end diastole and in end systole in at least two scan planes. The volume estimate is obtained by the Simpson method, which is implemented on most conventional scanners.

This means that the examiner has to draw the endocardium four times, for every stress-level she wants to examine. The normal procedure is to use three stress-levels. Consequently, endocardium has to be traced at least twelve times. This is obviously

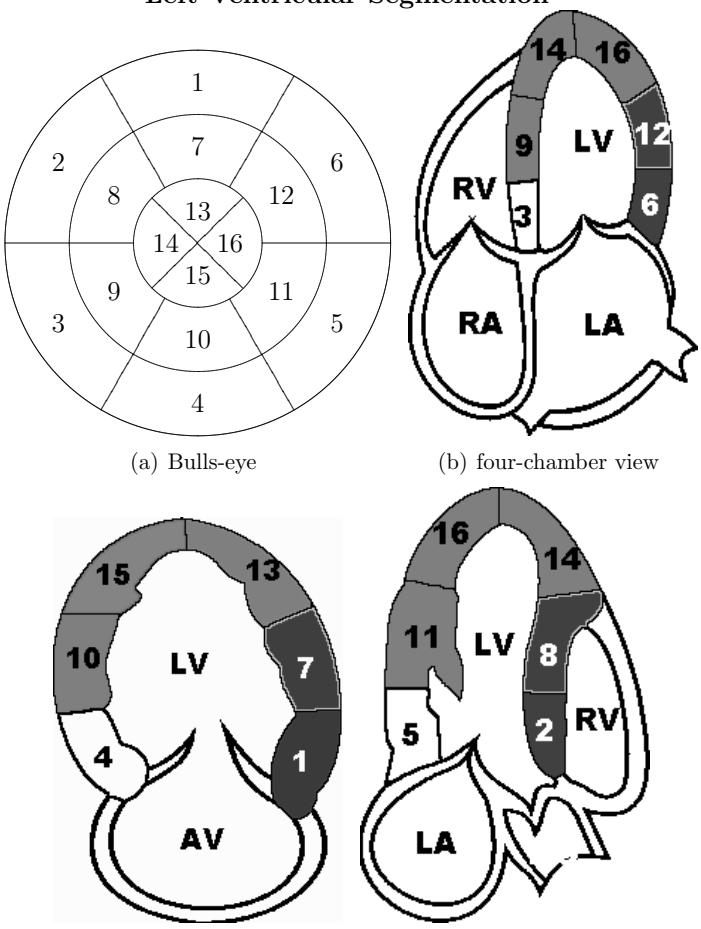

(a) Bulls-eye (b) four-chamber view

(c) two-chamber view (d) long-axis view

1. basal anterior
2. basal anteroseptal
3. basal inferoseptal
4. basal inferior
5. basal inferolateral
6. basal anterolateral
7. mid anterior
8. mid anteroseptal
9. mid inferoseptal
10. mid inferior
11. mid inferolateral
12. mid anterolateral
13. apical anterior
14. apical septal
15. apical inferior
16. apical lateral

Figure 1.4: Fig. (a) Display, on circumferential polar plot, of the 16 myocardial segments and recommended nomenclature recommended for echocardiography. Fig. (b) to (d) are planes through the heart according to the ultrasound four-chamber view, two-chamber view and long-axis view

very time-consuming and a reliable endocardium detection routine is needed to make the whole procedure fully automatic. The next section covers an introduction to this field.

1.3 Tracking algorithms of endocardium

Various automatic and semi-automatic methods have been implemented on scanners to track endocardium. Also, several authors have reported post-processing algorithms to detect endocardium. Here is a short resume of existing methods for extracting endocardium border.

1. Hand-crafted methods: Flexible models can be built up from simple subcomponents such as circles, arcs, lines etc, which are allowed a certain degree of freedom. The algorithm searches through the image for these features one at the time. Yuille et. al. [21] model parts of the face such as the eyes and the mouth in this way. Lipton et. al. [22] modeled the left ventricle using a handcrafted method in combination with Generic Algorithms from echocardiograms.

2. Articulated methods: A number of authors consider articulated models built from rigid bodies connected by sliding and rotating joints. Beinglass and Wolfson [23] describe a scheme of locating such objects using the generalized Hough transform with the point of articulation as the reference point for each sub-part. Connected sub-parts vote for the same reference point. Malassiotis and Strintzis [24] use the Hough transform in combination with an active shape model to track the endocardium from ultrasound images.

3. Active Contour Models (snake): Kass et al. [25] describe flexible contours, which are attached to image features. These energy minimization spline curves are modeled as having stiffness and elasticity and they are attracted toward features such as lines and edges. Constraints can be applied to ensure smoothness and continuity. The snake algorithm is a parametrized model, where the parameters are the control points of the spline. This method has been widely implemented on ultrasound scanners in various ways [26] to [30]. Also GE Vingmed Ultrasound AS Vivid 7 has a snake algorithm using the atrial-ventricular valve plane and apex detection scheme to find endocardium.

4. Active Shape Models: Initial estimates of shape, scale and orientation are made. Shape parameters are then changed in a scheme evaluated by principal component analysis. The model searches for high gradients normal to the initial shape. This model is expanded to yield the motion of the shape by Bosch et al. [31]. This model is called active appearance motion-model. This is a promising border detection algorithm, where the shape parameters are

evaluated from expert cardiologist drawings. Other references on active shape models are [32] to [34].

5. Region growing method: This method divides the image into sub-regions, which have certain properties. Sub-regions that lie next to each other are merged when they have similar properties. The regions can also be split, when properties are not spatially uniform. Dove et al. [35] combined a region-growing scheme with a Fuzzy Hough Transform to detect endocardium on ultrasonic images.

1.4 Software interface for ultrasound data

General Electric Vingmed Ultrasound AS, Horten has provided a software interface that handles images from their Idunn scanner system. The program is called GcMat and communicates with Matlab (The MathWorks Inc.) and a display subsystem of Idunn. Matlab's libraries are directed towards research and various toolboxes such as signal processing, image processing, spline and symbolic mathematics are frequently used in this environment. Matlab is interactive and allows Just In Time compilation and communicates with other computer languages such as C, C++ and Fortran. GcMat controls the communication between Matlab and GcViewer using the Microsoft ActiveX COM-component. GcMat is therefore unfortunately restricted to Windows platforms only.

GcMat is made for product development and research. All signal and image processing libraries of the Idunn scanner are available. Images can basically be taken out of the signal chain at any point and be manipulated further using Matlab's libraries. Finally, the images can be written back to GcMat for visualization. The user can also add graphics such as points, curves and transparent jpg images into the GcMat environment.

Part II

Bandwidth of the Ultrasound Doppler Signal with Applications in Blood/Tissue Segmentation in the Left Ventricle

Abstract

The bandwidth of the ultrasound Doppler signal is proposed as a classification function of blood and tissue signal in transthoracial echocardiography of the left ventricle. The new echocardiographic mode, Bandwidth Imaging, utilizes the difference in motion between tissue and blood. Specifically, Bandwidth Imaging is the absolute value of the normalized autocorrelation function with lag one. Bandwidth Imaging is therefore linearly dependent on the the square of the bandwidth estimated from the Doppler spectrum. A 2-tap Finite Impulse Response highpass filter is used prior to autocorrelation calculation to account for the high level of DC clutter noise in the apical regions. Reasonable pulse strategies are discussed and several images of Bandwidth Imaging are included. An in vivo experiment is presented, where the apparent error rate of Bandwidth Imaging is compared with apparent error rate of Second-Harmonic Imaging on 15 healthy men. The apparent error rate is calculated from signal from all myocardial wall segments defined in [1]. The ground truth of the position of the myocardial wall segments is determined by manual tracing of endocardium in Second-Harmonic Imaging. A hypotheses test of Bandwidth Imaging having lower apparent error rate than Second-Harmonic Imaging is proved for a p-value of 0.94 in 3 segments of end diastole and 1 segment in end systole on non averaged data. When data is averaged by a structural element of 5 radial, 3 lateral and 4 temporal samples, the numbers of segments are increased to 9 in end diastole and to 6 in end systole. These segments are mostly located in apical and anterior wall regions. Further, a global measure GM is defined as the proportion of misclassified area in the regions close to endocardium in an image. The hypothesis test of Second-Harmonic Imaging having lower GM than Bandwidth Imaging is proved for a p-value of 0.94 in the four-chamber view in end systole in any type of averaging. On the other side, the hypothesis test of Bandwidth Imaging having lower GM than Second-Harmonic Imaging is proved for a p-value of 0.94 in long-axis view in end diastole in any type of averaging. Moreover, if images are averaged by the above structural element the test indicates that Bandwidth Imaging has a lower apparent error rate than Second-Harmonic Imaging in all views and times (end diastole or end systole), except in four-chamber view in end systole. This experiment indicates that Bandwidth Imaging can supply additional information for automatic border detection routines on endocardium.

Chapter 1

Introduction

The ejection fraction is one of the most commonly measured parameters in diagnosis and follow up of coronary heart decease, valve decease and heart failure. The ejection fraction is the ejected volume divided by the maximum volume of the left ventricle, and measuring ejection fraction involves defining the endocardial border, either automatically or by manual tracing.

In ejection fraction calculation, the endocardial border has to be traced in at least two scan planes in both end diastole and end systole. In stress echo examination, ejection fraction is commonly calculated at three levels of stress. A robust routine for detecting endocardium automatically is needed to save examination time.

Many approaches have been suggested to solve the endocardium tracking problem. We mention here briefly; active contour models (snakes) [26], [27], [28], [29] and [30] , active shape models [31], [32], [33] and [34] , region-growing scheme [35] and Hough transform [24]. Common for all these approaches is that they are all applied on Second-Harmonic Imaging data.

However, GE Vingmed Ultrasound AS Vivid 7 has an automatic routine that uses Tissue Velocity Imaging data in addition to Second-Harmonic Imaging data. Prior to the border detection, the atrial ventricular plane and apex are detected using an algorithm that searches for points with desired gray scale intensity and tissue movement. A simple version of this apex and atrial ventricular plane detection algorithm is presented in Storaa et al. [36]. This is an interesting example of how robustness can be achieved by using other data sets than Second-Harmonic Imaging.

It is an important point, that Bandwidth Imaging is not the same as the Variance-mode, available on most conventional Color Flow Imaging systems. In the Variance-mode, the variance of the blood flow estimate is estimated by the square of the bandwidth divided by the packetsize [9] (page 10.20). Prior to the variance estimates, the signal is highpass filtered to remove clutter noise from surrounding tissue. This improves the variance estimates in the blood pool. Hence in tissue, the signal ends up containing mostly white noise, which is not at all related to the motion of the scatterers in the actual range cell. The variance estimates are therefore not suited for blood pool definition in Color Flow Imaging systems. In general, only the power

of the highpass filtered Doppler signal is used for this purpose.

In Bandwidth Imaging contradictory, signal from tissue is only partially attenuated before the bandwidth estimate. The signal from tissue has therefore a narrow bandwidth, while signal from blood has broader bandwidth, since this signal is a mixture of blood signal and clutter noise. Bandwidth Imaging is therefore used as a classification function.

In Power Doppler the packetsize has to be at least 6 to achieve a useful stop-band in the highpass filter [18]. However in Bandwidth Imaging, a 2-tap Finite Impulse Response highpass filter is sufficient and this filter is available with a packetsize of 3. The temporal resolution is proportional to the packetsize and this gives an important resolution gain compared to Power Doppler. Further, spatial resolution and framerate are increased by using Multi-Line acquisition. Multi-Line acquisition is reconstruction of multiple scan lines from sparsely transmitted scan lines. This means that Bandwidth Imaging is available at a temporal and spatial resolution that is interesting in endocardial border detection.

In order to discuss the usefulness of Bandwidth Imaging, an in vivo experiment on 15 healthy male is introduced. A similar experiment is suggested by Spencer et. al. in [6]. Here, the visualization of Second-Harmonic Imaging and Fundamental Imaging were rated by expert cardiologists in all myocardial segments outlined in [1]. However, the visual differences between Bandwidth Imaging and Second-Harmonic Imaging are more radical than the visual differences between Fundamental Imaging and Second-Harmonic Imaging. Therefore, a test which is less dependent on visual perception is introduced in this part .

Chapter 2

Bandwidth Imaging

The bandwidth estimator is found to be

$$B^2 = 2 - 2\frac{|r(1)|}{r(0)} \tag{2.1}$$

in [9] and [8]. Here the autocorrelation function $r(m)$ is estimated from the signal z_n by

$$r(m) = \frac{1}{N}\sum_{n=0}^{N-m-1} \overline{z_n} z_{n+m} \qquad \text{for} \qquad 0 \leq m \leq N-1 \tag{2.2}$$

In Bandwidth Imaging the packet size N is set to 3. A derivation of estimators of the bandwidth, mean frequency shift and power of the Doppler signal with packetsize 3 is given in Appendix A. Notice that the signal dependent part of B^2, is dependent on the absolute value of the normalized autocorrelation function with lag one. For simplicity Bandwidth Imaging is defined as:

$$\text{Bandwidth Imaging} = \frac{|r(1)|}{r(0)} \tag{2.3}$$

Bandwidth Imaging is therefore high when bandwidth is small and visa verse. This is because Bandwidth Images should be white in tissue and black in blood, similar to Second-Harmonic Images.

The appearance of white noise biases the estimate downward, while clutter noise biases the estimate upward. To compensate for the effect of clutter noise, a 2-tap Finite Impulse Response highpass filter prior to autocorrelation calculation is introduced

$$\begin{aligned} x_1 &= z_2 - 10^{-\frac{\text{AF}}{20}} z_1 \\ x_2 &= z_3 - 10^{-\frac{\text{AF}}{20}} z_2 \end{aligned} \tag{2.4}$$

where AF is the attenuation factor at zero frequency in dB. When AF is high the filter can be regarded as a stationary canceling filter and the transfer function is

given in [8] (page 209). In apical views, the clutter noise level is high in the near field and the white noise level increases by depth due to depth gain compensation. We have therefore found it reasonable to let AF decrease linearly from 40 dB to 15 dB in images from apical views with depth 15 cm.

2.1 Instrumentation of Bandwidth Imaging

The strategy for implementation of Bandwidth Imaging is by trial and error of various pulse strategies on a scanner (Vivid 7, GE Vingmed Ultrasound AS (Horten)). A reasonable pulse strategy for Bandwidth Imaging is given in Table 2.1. The pulse strategy for Second-Harmonic Imaging, which is used in chapter 3, is shown for comparison.

The center frequency for Bandwidth Imaging is a trade off between lateral resolution and penetration and is set to 2.5 MHz. The pulse length of 0.7 mm is chosen as a trade off between radial resolution and sensitivity. The pulse repetition frequency is set to 3750 and this choice is augmented for in subsection 3.4.4. The packet size is 3, which is the lowest possible for calculating Bandwidth Imaging with the filter given by equation (2.4).

Note that the pulse length is about 50 % longer in Bandwidth Imaging than in Second-Harmonic Imaging. Also, Bandwidth Imaging contains approximately 33 % less beams per frame than Second-Harmonic Imaging. This is because the framerate of Bandwidth Imaging is equal to the framerate of Second-Harmonic Imaging, the packet size is three times higher, the Multi-Line acquisition parameter is doubled and pulse repetition frequency is about the same.

The In Quadrature (signal after complex demodulation in the signal chain) data is recorded and saved to a file for further post-processing in Matlab (The MathWorks Inc.). In Bandwidth Imaging, signal is highpass filtered by equation (2.4) and then calculated by equation (2.3). Second-Harmonic Imaging is calculated by log compressing the square root of $r(0)$. The images are then scan converted to get physical scale and histogram equalized to get comparable contrast.

Table 2.1: Parameters related to the transducer for Bandwidth Imaging and Second-Harmonic Imaging

	Parameter	Value
Bandwidth Imaging	Center frequency	2.5 MHz
	Pulse repetition frequency	3.75 kHz
	Multi-Line acquisition	4
	Packetsize	3
	Radial resolution	$6.67 \cdot 10^{-4}$ m
	Aperture	$2.2 \cdot 10^{-3} \times 2.0 \cdot 10^{-3}\,\mathrm{m}^2$
	Depth	0.15 m
	Focal point (single)	0.15 m
	Framerate	44
	Number of beams	127
Second-Harmonic Imaging	Center frequency trans./rec.	1.7/3.4 MHz
	Pulse repetition frequency	4.25 kHz
	Multi-Line acquisition	2
	Packet size	1
	Radial resolution	$4.6 \cdot 10^{-4}$ m
	Aperture	$2.2 \cdot 10^{-3} \times 2.0 \cdot 10^{-3}\,\mathrm{m}^2$
	Depth	0.15 m
	Focal point (single)	0.09 m
	Framerate	44
	Number of beams	193

Chapter 3

Experiment for comparing Bandwidth Imaging with Second-Harmonic Imaging

3.1 Methods

The test included 15 healthy male persons aged 24 to 32. The image qualities were acceptable, which means that decent agreement with Magnetic Resonance Images [37] were expected. The three standard apical views, four-chamber, two-chamber and long-axis view were recorded in one loop each. The pulse strategy and the instrumentation details were the same as given in section 2.1.

The depth was set to 15 cm and a single transmit focus was chosen in both Second-Harmonic Imaging and Bandwidth Imaging to get better resolution. In this study all depth gain compensations were equalized for all depths to eliminate for this variability.

The subjects were asked to hold their breath and keep still during recording. This enabled the examiner to compare Second-Harmonic Imaging and Bandwidth Imaging from the same positions. Afterwards, the images were re-examined in a GE Vingmed Ultrasound AS (Horten) application called GcMat. This application communicates with Matlab Inc. for post-processing data. The examiner traced endocardium in the Second-Harmonic Images in both end systole and end diastole in all three views. Immediately after tracing in the Second-Harmonic Images, the same traces were shown in the corresponding Bandwidth Images. In cases where the subject moved under the examination, the examiner retraced on the Bandwidth Images.

In article [1], recommendations for nomenclature and standardized segmentation of myocardium are given. The sixteen segmentation model for echocardiography is shown in the bulls-eye diagram in Fig. 3.1(a).

The segments are found by slicing the ventricle into three thirds. The parallel slices have equal space between each other and are perpendicular to the left ventri-

cle long-axis. These three slices are further divided into the final myocardial wall segments. The mid- and basal slices consist of six equally sized segments, while the apical slice consists of four segments. This can be seen in Fig. 3.1. Echocardiographic images from four-chamber view, two-chamber view and long-axis view are shown in Fig. 3.1(b), 3.1(c) and 3.1(d). The four-chamber view assesses basal inferoseptal, mid inferoseptal, apical septal, apical lateral, mid anterolateral and basal anterolateral segments. The two-chamber view accesses basal anterior, mid anterior, apical anterior, apical inferior, mid inferior and basal inferior segments. Finally, the long-axis view accesses the basal anteroseptal, mid anteroseptal, apical septal, apical lateral, mid inferolateral and basal inferolateral.

From the manual traces of endocardium, the shape and position of myocardial segments are calculated. This is done by first finding the left ventricle long-axis. Then three perpendicular lines to the long axis line are calculated. These three lines intersect the long-axis at the bottom, one third up and two thirds up. These three lines also intersect the endocardium trace at six points. A seventh point is found as the intersection between the endocardium trace and the long-axis view trace. These seven points define the corner points of the myocardial segments along endocardium. The width of each myocardial segment is set to 20 % of the myocardial short axis. These segments are seen in figure 3.1(b), 3.1(c) and 3.1(d). Here corresponding blood segments are shown on the inside of endocardium. The number labels are denoted in the blood segments, corresponding to the myocardial segments.

All recorded data inside each myocardial segment and each blood segment were stored in an array, with labels of subject number, segment name, segment type (blood or tissue), method (Second-Harmonic Imaging of Bandwidth Imaging) and time instance (end diastole or end systole).

3.1.1 Evaluation criteria for classification functions

A comprehensive discussion of classification theory can be found in [38]. The quantity apparent error rate is chosen to evaluate the performance of the classification functions Bandwidth Imaging and Second-Harmonic Imaging. Advantages of apparent error rate are that it is easy to implement and not dependent of the form of the parent populations.

$$\text{Apparent error rate} = \frac{n_{bM} + n_{tM}}{n_b + n_t} \tag{3.1}$$

Here, n_t and n_b are the sizes of measured data from tissue π_t and blood π_b. Further, n_{tM} and n_{bM} are the number of misclassifications of π_t and π_b. Apparent error rate is simply the proportion of misclassifications of the total dataset. In Bandwidth Imaging and Second-Harmonic Imaging blood and tissue are classified by thresholding. A discussion of this is found in Appendix B. In this experiment the best threshold is chosen, and apparent error rate is therefore independent of any monotone transformations of π_t and π_b. The definition of apparent error rate is changed

to;

$$\text{Apparent error rate} = \min_{T} \left(\frac{n_{bMT} + n_{tMT}}{n_b + n_t} \right) \tag{3.2}$$

where the number of misclassifications with threshold T are denoted n_{tMT} and n_{tMT}. Moreover, a significant problem with this criteria is related to the resolution inhomogeneity in sectorscan images. In apical segments, the spatial resolution close to the probe is much higher than the spatial resolution further down. Therefore, a third version of apparent error rate is proposed,

$$\text{Apparent error rate} = \min_{T} \left(\frac{\sum_{i=1}^{n_{bMT}} c_{bMTi} + \sum_{i=1}^{n_{tMT}} c_{tMTi}}{\sum_{i=1}^{n_b} c_{bi} + \sum_{i=1}^{n_t} c_{ti}} \right) \tag{3.3}$$

Here, the cost of sample i in π_b or π_t are c_{bi} or c_{ti}. For a threshold T, the costs of misclassifications in blood and tissue are c_{bMTi} and c_{tMTi}. The values of c_{bi}, c_{ti}, c_{bMTi} and c_{tMTi} are equal to the areas the measurements are representing in the image. Apparent error rate is therefore the proportion of misclassified area, given the best possible threshold. It is important to emphasize that the threshold is constant only inside one segment.

In this experiment, a more global measure is also introduced, where histogram variations within an image is taken into account. Here all data from the six myocardial segments in one image is stored into Π_t. Also, the corresponding blood data is stored in Π_b. The global measure GM is defined as

$$\text{GM} = \min_{T} \left(\frac{\sum_{i=1}^{N_{bMT}} C_{bMTi} + \sum_{i=1}^{N_{tMT}} C_{tMTi}}{\sum_{i=1}^{N_b} C_{bi} + \sum_{i=1}^{N_t} C_{ti}} \right) \tag{3.4}$$

where the sizes of Π_b and Π_t are N_b and N_t. Numbers of misclassification at threshold T are N_{bMT} and N_{tMT}, in blood and tissue respectively. Further, C_{bi} is cost of sample i in Π_b and C_{ti} is cost of sample i in Π_t. Also, C_{bMTi} and C_{tMTi} are costs of misclassifications in Π_b and Π_t. GM is therefore the proportion of misclassified area in an image, given the best possible threshold.

In order to discuss GM we have found it instructive to define another measure in this experiment. The local measure LM is defined as

$$\text{LM} = \sum_{j=1}^{6} \left(\min_{T} \left(\frac{\sum_{i=1}^{n_{bMTj}} c_{bMTij} + \sum_{i=1}^{n_{tMTj}} c_{tMTij}}{\sum_{i=1}^{N_b} C_{bi} + \sum_{i=1}^{N_t} C_{ti}} \right) \right) \tag{3.5}$$

where j denotes the segment number in the image, ranging from 1 to 6. Moreover, C_{bMTij} and C_{tMTij} are costs of misclassifications of a sample i at threshold T for segment j in blood and tissue. The numbers of misclassification for segment j are n_{tMTj} and n_{bMTj}, in tissue and blood, respectively. LM is basically the mean of the apparent error rates for all the segments in an image. In LM the threshold level can vary from segment to segment, while in GM the threshold level is constant for the whole image. Therefore, if GM and LM differ a lot, the histograms between

the segments also differ a lot. Note that this ratio is independent of any monotone transformation of the data. This ratio is therefore a good measure of the histogram uniformity HUM:

$$\mathrm{HUM} = \frac{\mathrm{GM}}{\mathrm{LM}} \tag{3.6}$$

Prior to apparent error rate, GM and HUM calculation the images have either been non averaged, moderately averaged or strongly averaged. In moderate averaging, the structural element is 3 radial, 2 lateral and 3 temporal samples in Second-Harmonic Imaging. To account for the resolution loss in Bandwidth Imaging, the structural element in moderate averaging is reduced to 2 radial, 2 lateral and 2 temporal samples. In strong averaging, the structural element is 5 radial, 3 lateral and 4 temporal samples in Second-Harmonic Imaging and 4 radial, 2 lateral and 4 temporal samples in Bandwidth Imaging.

3.2 Results

The occasions where the apparent error rate of Bandwidth Imaging is smaller than apparent error rate of Second-Harmonic Imaging are counted in all segments. This number ranges from 0 to 15, since 15 subjects attended the study. The result is shown in Fig. 3.2. If numbers are 11 or above, the p-values are higher than 0.94 on the hypothesis test; true apparent error rate of Bandwidth Imaging is equal or lower than true apparent error rate of Second-Harmonic Imaging.

This means that if we assume that true apparent error rate of Second-Harmonic Imaging is lower than or equal to true apparent error rate of Bandwidth Imaging, then there is less than 6 percent chance that the result of this test would occur. If we had assumed that true apparent error rate of Second-Harmonic Imaging is higher than true apparent error rate of Bandwidth Imaging, then the outcome of this experiment is more likely than 6 percent to occur.

This indicates that Bandwidth Imaging classifies better than Second-Harmonic Imaging in these segments, and these segments are therefore marked green. Segments with numbers four and below are marked red, because the test indicates that Second-Harmonic Imaging has a lower apparent error rate than Bandwidth Imaging in these segments. The left column shows results of end diastole and the right column shows results of end systole.

In apical septal and in apical lateral segments a super-index and a sub-index are given. The super-index tells us which view has the lowest mean apparent error rate taken over subjects in Bandwidth Imaging. Correspondingly, the sub-index shows the best view of Second-Harmonic Imaging. Here 4 means four-chamber view and L means long-axis view. In these segments, the test compares the apparent error rate of Second-Harmonic Imaging and the apparent error rate of Bandwidth Imaging from their respective best views.

The top row shows apparent error rate calculated from not averaged data. In

end diastole, the test indicates that Second-Harmonic Imaging has a smaller apparent error rate than Bandwidth Imaging in basal inferoseptal, basal inferior, basal inferolateral, basal anterolateral, mid inferoseptal and mid inferior. Contradictory, the test indicates that Bandwidth Imaging has a smaller apparent error rate than Second-Harmonic Imaging in mid anterior, mid anterolateral and apical lateral. The test can not indicate which method has the smallest apparent error rate in the other segments. In end systole, the high scores of Second-Harmonic Imaging are found in basal anteroseptal, basal inferoseptal, basal inferior, basal inferolateral, basal anterolateral, mid inferoseptal, mid inferior, mid inferolateral and mid anterolateral. The only high score of Bandwidth Imaging is found in the mid anterior segment. The test can not indicate which method has the lowest apparent error rate in the other segments.

In the mid and bottom row of Fig. 3.2 the test is performed on moderately and strongly averaged data, respectively. In end systole with moderate averaging, the basal anterior, mid anteroseptal, apical anterior and apical septal becomes green in addition to the green segments of the non averaged data. The basal anterolateral segment however, goes from red to undecidable. In strong averaging also basal anteroseptal and apical inferior become green, while mid inferior and basal inferolateral go from red to undecidable.

In end systole with moderate averaging, the apical anterior segment becomes green, while basal anteroseptal, basal inferolateral, mid inferolateral and mid anterolateral segments go from red to undecidable. In strong averaging basal anterior, mid anteroseptal, apical inferior and apical lateral go from undecidable to green. The mid inferior segment goes from red to undecidable.

The effect of averaging is therefore that the number of green segments is increased from 3 to 7 to 9 in end diastole and from 1 to 2 to 6 in end systole. Also, the number of red segments is reduced from 6 to 5 to 3 in end diastole and from 9 to 5 to 4 end systole.

The top row of Fig. 3.3 shows the mean apparent error rate (in percent) taken over subjects for Bandwidth Imaging (top number) and for Second-Harmonic Imaging (bottom number). The results for end diastole are shown in the left column and the results for end systole are shown in the right column. In apical septal and apical lateral segments the minimum means are shown, corresponding to sub- and superindexes of Fig. 3.2. The next two rows show the corresponding numbers when data is moderately and strongly averaged. Note that the apparent error rate decreases with averaging in every segment at any time instance (end diastole or end systole).

In Fig. 3.3, we see that the apparent error rate is very different in various segments. On non averaged data, the apparent error rate of Bandwidth Imaging, varies from 0.21 to 0.37 in end diastole and 0.27 to 0.38 in end systole, while apparent error rate of Second-Harmonic Imaging, varies from 0.11 to 0.38 in end diastole and 0.16 to 0.40 in end systole. The smallest numbers of the apparent error rate are found in segments where Second-Harmonic Imaging works best, and the largest numbers of apparent error rate are found in segments where Bandwidth Imaging works best.

This effect is further investigated by grouping the segments. The segments with green numbers in Fig. 3.3(a) are the best Bandwidth Imaging segments in end diastole BEDS. Similarly we have HEDS, which are the best Second-Harmonic Imaging segments in end diastole and the undecidable end diastole segments UEDS. In the systole we have correspondingly defined BESS, HESS and UESS from Fig. 3.3(b).

Fig. 3.4(a) and 3.4(b) show mean apparent error rate of Second-Harmonic Imaging and Bandwidth Imaging, taken over subjects and segments in the above groups. The x axes of the figures show the level of averaging. It is clear that the Bandwidth Imaging groups are more collected than the Second-Harmonic Imaging groups. This indicates that the great regional differences seen in Fig. 3.2 are more a matter of regional differences of Second-Harmonic Imaging, rather than regional differences of Bandwidth Imaging. Furthermore, we see that Bandwidth Imaging decreases more rapidly by averaging than Second-Harmonic Imaging.

The result of GM is shown in the Table 3.1. Here, the occasions where GM of Bandwidth Imaging is smaller than GM of Second-Harmonic Imaging are counted for each view. This is done in end diastole and in end systole without averaging, with moderate averaging and with strong averaging. Similarly to the result shown in Fig. 3.2, values above 11 are marked green and the values below 4 are marked red.

The test indicates that Second-Harmonic Imaging has a smaller GM than Bandwidth Imaging in four-chamber view in end systole in any type of averaging. On the other side, Bandwidth Imaging has a smaller GM in long-axis view in end diastole in any type of averaging. In moderate averaging two-chamber view and long-axis view are marked green in end diastole and two-chamber view is marked green in end systole. In strong averaging all views are marked green except the four-chamber view in end systole.

In Table 3.2 the results of HUM are plotted in the same manner as for GM. The test indicates that Bandwidth Imaging has a lower HUM in all views without and with moderate averaging. In strong averaging the test is indecisive in all views, except four-chamber view in end systole. This number is green.

Furthermore, in Fig. 3.5(a), 3.5(b), 3.5(c), 3.5(d), 3.5(e) and 3.5(f) both GM and LM are plotted from four-chamber view, two-chamber view and long-axis view in end diastole and end systole as functions of averaging. It is an important result that GM and LM decrease by averaging in both methods. This makes it fair to compare similarly averaged images. Obviously the LM lines lies below the GM lines. The gap between GM and LM is larger in Second-Harmonic Imaging than in Bandwidth Imaging. This explains the HUM results.

3.3 Discussion of the comparison experiment

In comparing Second-Harmonic Imaging and Bandwidth Imaging, the ground truth of the endocardial borders are found by manual traces on Second-Harmonic Images.

It can be objected that there is a flaw in comparing two methods, when the ground truth is determined by one of them. On the other side, manual traces of endocardium on images of reasonable image quality as basis for ejection fraction measurements are reported to have reasonable agreement with ejection fraction measurements of Magnetic Resonance Imaging [37]. In this study the subjects had reasonable image qualities, and this votes for more trust to the manual traces as ground truth of endocardium. Moreover, if the manual traces are biased, it can be argued that they are biased in favor of Second-Harmonic Imaging, since they are drawn on Second-Harmonic Images. This would therefore only strengthen the results in favor of Bandwidth Imaging.

We have selected apparent error rate as the quantitative evaluation criteria of Bandwidth Imaging and Second-Harmonic Imaging. This measure is intuitive because it calculates the proportion of misclassified area, given the best threshold. In a practical clinical setting this threshold level is not known. However, automatic border detection routines are in general more dependent on a good tissue to blood contrast, rather than evenly distributed intensity levels in an image. We therefore postulate that the apparent error rate is related to the potential of an automatic detection routine of endocardium.

Further, one may argue that the threshold level is evaluated by the measured data, and therefore apparent error rate is underestimating the true optimal error rate. On the other side, it is suggested in [38] that apparent error rate is approaching the true optimal error rate when the sample sizes are high. In this experiment the sample sizes are above 1000 in all segments. And, even if apparent error rate is underestimating the true optimal error rate, the comparison of Bandwidth Imaging and Second-Harmonic Imaging may still be valid. This provides that apparent error rate is biased equally in Bandwidth Imaging and Second-Harmonic Imaging. The results of the hypothesis test, Bandwidth Imaging having lower apparent error rate than Second-Harmonic Imaging, is therefore emphasized in this manuscript.

In the experiment we found the lowest values of apparent error rate in segments where Second-Harmonic Imaging worked best, and the largest values of apparent error in segments where Bandwidth Imaging worked best. This indicates that the great regional differences seen in Fig. 3.2 are more a matter of regional differences in Second-Harmonic Imaging, rather than regional differences in Bandwidth Imaging. This is also seen in Fig. 3.4(a) and 3.4(b).

Since the traces of endocardium in end diastole and end systole are needed for ejection fraction calculation, only these time instances are considered in this experiment. Notice also the difference between end diastole and end systole in Fig. 3.4 and 3.5. These differences are greater in Bandwidth Imaging than in Second-Harmonic Imaging.

Many automatic detection routines involve using several or all frames in a heart beat. Therefore averaged images have been considered in this study. It is important to notice from Fig. 3.2 that apparent error rate decreases with averaging in every segment at any time instance (end diastole or end systole). If this was not the

case, it would not be fair to compare averaged data of Second-Harmonic Imaging with averaged data of Bandwidth Imaging. The result that averaging seems to favor Bandwidth Imaging can be taken as an argument for employing Bandwidth Imaging data in detection routines that use many frames.

In the experiment GM was introduced as the apparent error rate, with constant threshold value in the whole image. In prescreening methods, such as finding left ventricle center, atrial ventricular plane, apex or other features, an image with small regional variance in intensity and few dropouts are desired. We postulate that there is a relation between GM and the efficiency of prescreening algorithms in left ventricle. Here, robustness is often more important than accuracy.

Next, histogram uniformity measure HUM is introduced to investigate the histogram variations between segments. It is defined as GM/LM and is obviously close to one when the optimal threshold is equal for all segments. HUM increases, when the optimal thresholds differ more between segments. In general the test indicates that HUM is lower in Bandwidth Imaging than in Second-Harmonic Imaging when data is not or moderately averaged.

These differences even out when data is averaged. The reason for this is that rapid myocardial movements have the effect of blurring the endocardial border on averaged images. In LM, this effect is accounted for by the adjustment of the threshold to an optimum level. In GM the threshold is not so adaptive, and blurring of the border results in a higher GM.

In this experiment we have discussed Bandwidth Imaging with one instrumentation strategy. We have indicated differences between myocardial segments, image views and time instances (end diastole and end systole). In the next section a discussion of other pulse strategies and parameter settings of Bandwidth Imaging is included.

3.4 Discussion of instrumentation of Bandwidth Imaging

In the process of instrumenting Bandwidth Imaging, we tried a variety of pulse repetition frequencies, pulse lengths, center frequencies and beam sizes. Also a great number of filter coefficients AF were tested. We found these effects important in instrumenting Bandwidth Imaging:

3.4.1 Transit time effect

In Fig. 3.6 six Second-Harmonic Images from two-chamber view are shown. These images correspond to 6 time steps, equally sparsed during one heart cycle. Image 1 shows end diastole and image 4 shows end systole.

In Fig. 3.7 an unfiltered version of Bandwidth Imaging is shown. The transit time effect is the effect of decorrelation of signal due to movement of scatterers inside

the range cell. In the systole (image 4), tissue is darker in the anterior wall segments (right side of the image), because this tissue moves faster than surrounding tissue. Note that the histogram equalization process is done on the dataset of a whole cardiac cycle. This is done so the transit time effect becomes easier to see. When viewing a movie of images, the myocardium is flickering. When pulse repetition frequency is turned down this effect becomes even stronger.

3.4.2 Clutter filter effect

In Fig. 3.8 the In Quadrature data is filtered with AF equal 40 dB, prior to calculation of the autocorrelation function. Here, the clutter noise of Fig. 3.7 is strongly reduced in the apex region. Notice that tissue is brightest in image 4, where the cardiac muscle is moving the most. This is because the clutter filter impulse response is velocity dependent [8] (page 209). This effect is stronger further down in the image, since the movement here is more rapid and the white noise level is higher. It is interesting to see that the clutter filter has the opposite effect of the transit time effect, where moving tissue is darker than stationary tissue.

In Fig. 3.9 this effect is accounted for by letting the attenuation factor AF of equation (2.4) be depth dependent. Here the attenuation factor decreases linearly from 40 to 15 dB. This is motivated from the fact that the DC clutter level is strongest in the apical region.

3.4.3 Other visual effects in Bandwidth Imaging

In Fig. 3.9 we see that tissue surrounding the cardiac muscle is more similar to tissue in the cardiac muscle in Bandwidth Imaging than in Second-Harmonic Imaging. This is most likely because Bandwidth Imaging is more dependent on motion of scatterers, while Second-Harmonic Imaging is more dependent on the reflection coefficient of the scatterers.

Next, the mitral valve and apparatus are not visible in Fig. 3.9. This can be explained by two factors. First, the signals from these features are mixtures of blood and tissue signals and therefore have broader bandwidths. Second, signal from vibrating muscles, such as in mitral apparatus, is known to have a broader bandwidth than signal from other tissue [39].

Also, the speckle pattern of Bandwidth Imaging differs from Fundamental Imaging. Bandwidth Imaging has s noise type that is often referred to as salt and pepper noise. Therefore a simple median filter is used with a neighborhood of 2 radial and 3 temporal samples in Fig. 3.10.

3.4.4 Factors influencing the choice of pulse repetition frequency

The transit time effect and clutter filter effect, are arguments for a higher pulse repetition frequency. Theoretically, pulse repetition frequency is limited upward by the speed of sound and by the penetration depth. In practical instrumentation setup, the effect of reverberations building up from shot to shot limits pulse repetition frequency upward before the theoretical limit.

In Second-Harmonic Imaging, the pulse repetition frequency is limited upward by reverberations from previous shots. This results in a pulse repetition frequency depending on focus of the transmitted beam, the center frequency and the pulse length. This problem is omitted in Color Flow Imaging, since the reverberation noise from earlier shots is removed by the clutter filter. In Bandwidth Imaging however, the clutter filter is only partial, and this effect has to be accounted for. In this study we found that a pulse repetition frequency of 3750 compromised these effects. This is further discussed in Appendix C.

3.5 Conclusion

A new echocardiographic mode has been proposed, where the difference in Doppler signal from blood flow and tissue motion is utilized. A reasonable instrumentation setup of Bandwidth Imaging is outlined in this manuscript. A major difference between Bandwidth Imaging and conventional Power Doppler and Variance-modes on Color Flow Imaging systems is that Bandwidth Imaging does not require a long stop-band highpass filter. Bandwidth Imaging can therefore be implemented with a packetsize 3. This means that Bandwidth Imaging can be implemented with a temporal and spatial resolution that is interesting for endocardial border detection.

An experiment is added, where apparent error rate of Bandwidth Imaging is compared with apparent error rate of Second-Harmonic Imaging. The results indicate that Bandwidth Imaging can compete with Second-Harmonic Imaging in some segments, especially in apical and anterior regions. The test suggests that Bandwidth Imaging has less differences between segments, improves more by averaging and has a more uniform histogram throughout the image. This votes for automatic routines using several time frames. In particular, we suggest using Bandwidth Imaging for prescreening methods for finding left ventricle features.

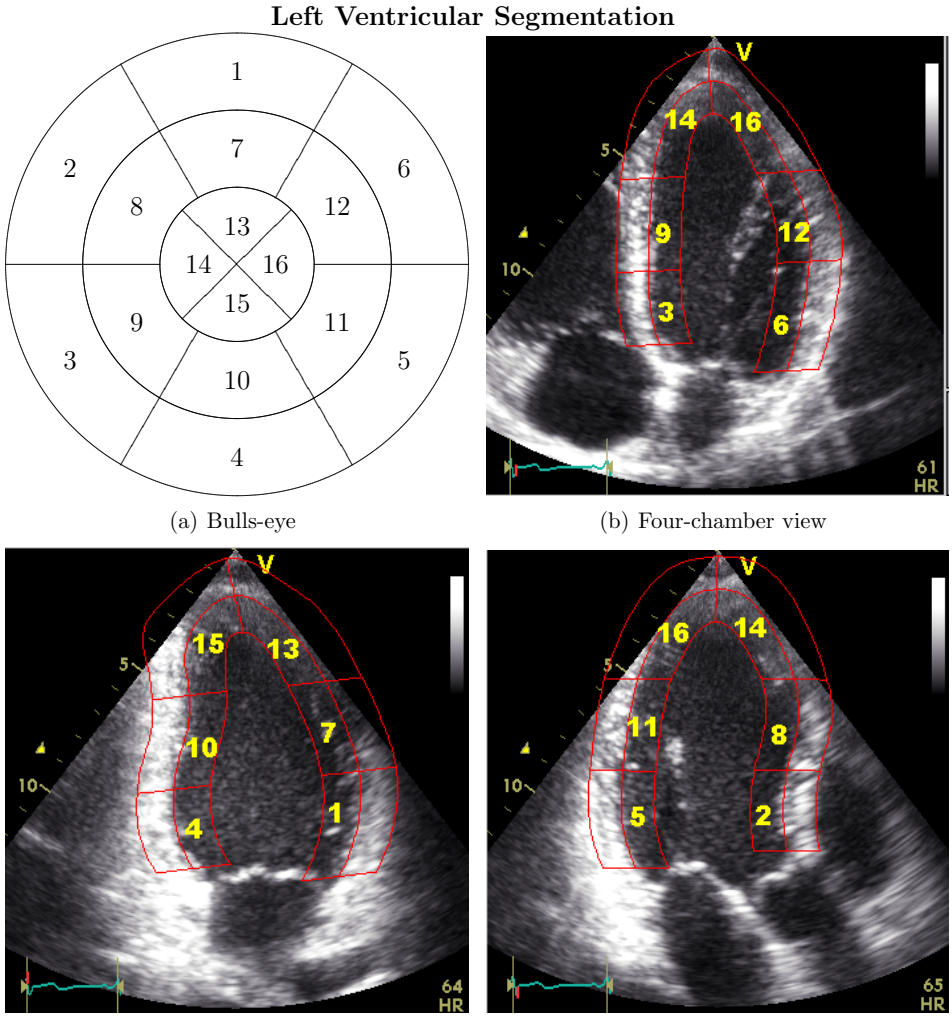

(a) Bulls-eye

(b) Four-chamber view

(c) Two-chamber view

(d) Long-axis view

1. basal anterior
2. basal anteroseptal
3. basal inferoseptal
4. basal inferior
5. basal inferolateral
6. basal anterolateral
7. mid anterior
8. mid anteroseptal
9. mid inferoseptal
10. mid inferior
11. mid inferolateral
12. mid anterolateral
13. apical anterior
14. apical septal
15. apical inferior
16. apical lateral

Figure 3.1: Display, on circumferential polar plot, of the 16 myocardial segments and recommended nomenclature recommended for echocardiography.

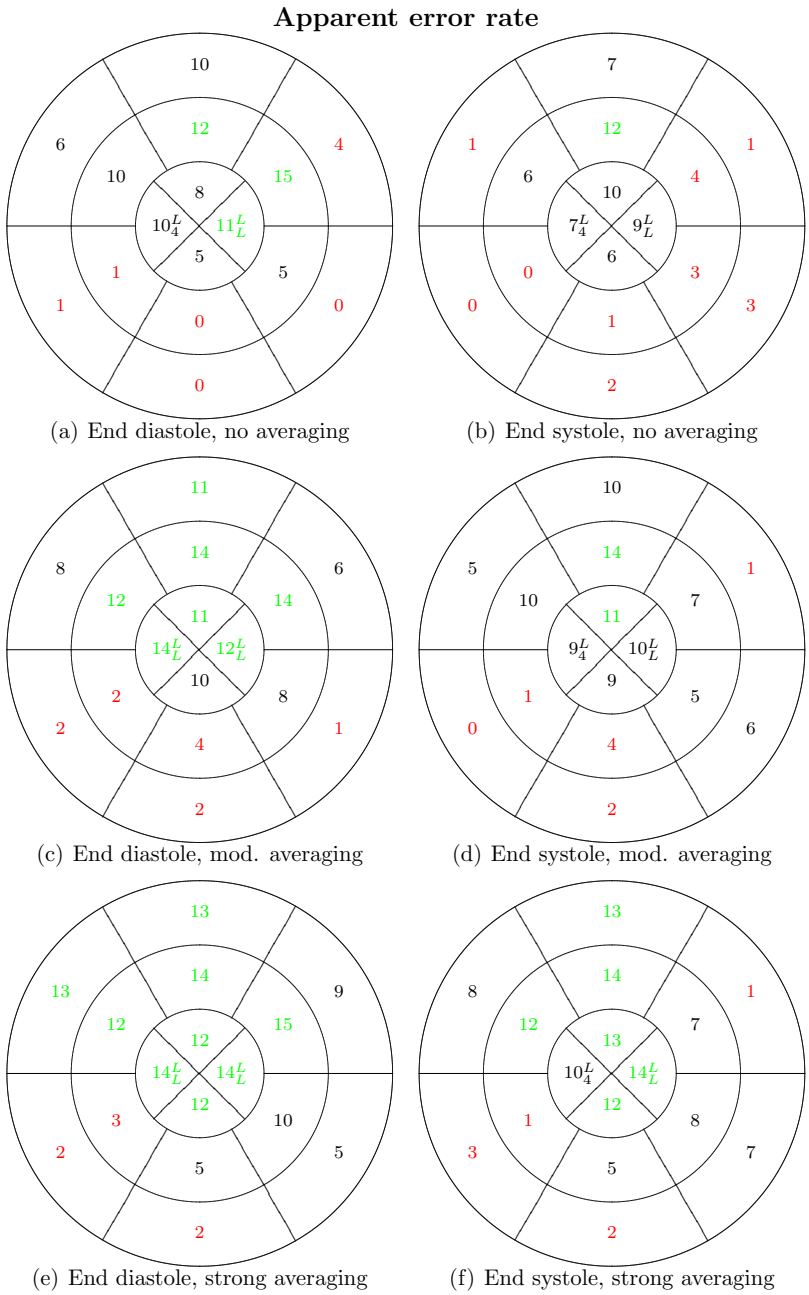

Figure 3.2: The results show the number out of 15 where apparent error rate is lower in Bandwidth Imaging than in Second-Harmonic Imaging in end diastole (left) and end systole (right) in all myocardial segments. Numbers of 11 and above are marked green, indicating that Bandwidth Imaging works best and numbers of 4 and below are marked red, indicating that Second-Harmonic Imaging works best. The three rows show result when images are not averaged, moderately averaged and strongly averaged, respectively.

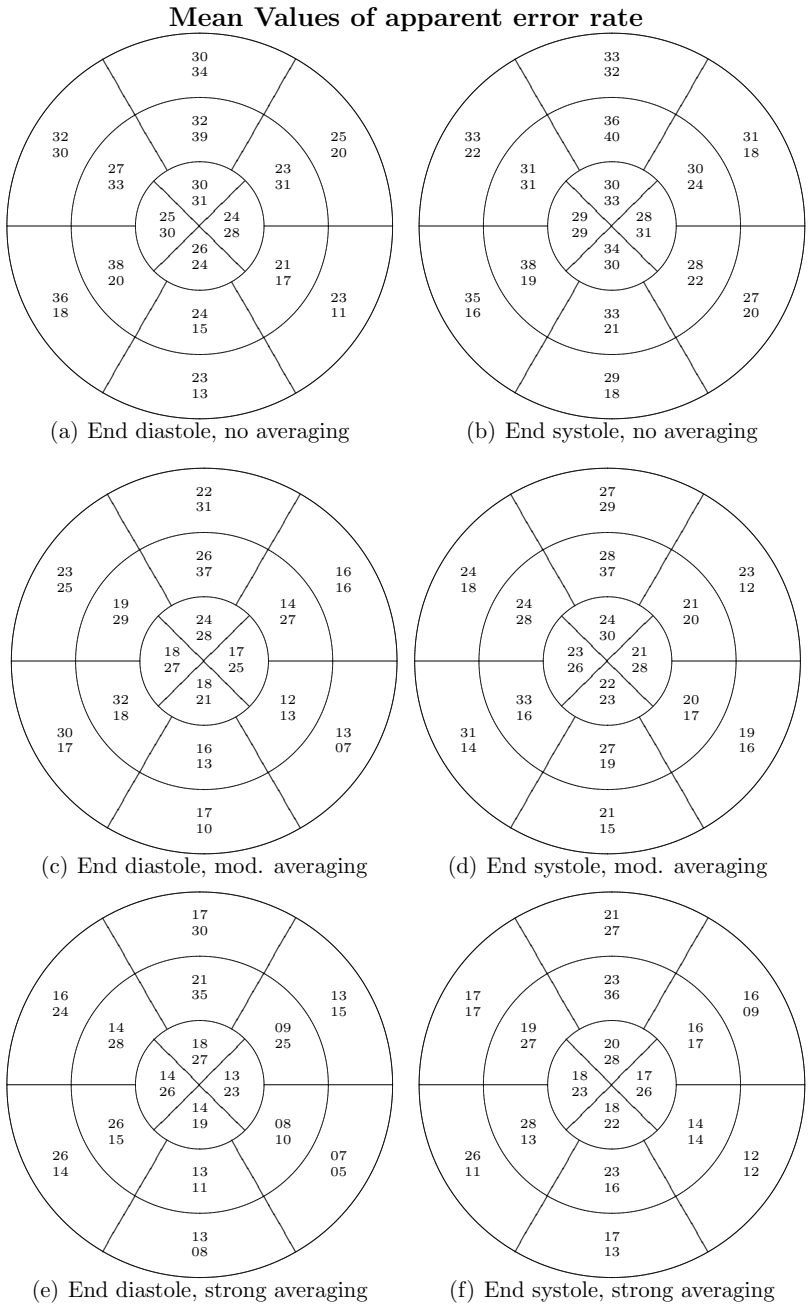

Figure 3.3: Mean values of the apparent error rate in percent, of Bandwidth Imaging segment (top) and Second-Harmonic Imaging segments (bottom). The results of the end diastole and the end systole are shown in the left and the right column at three levels of averaging. In apical septal and apical lateral segments the minimum value is shown, corresponding to sub- and super-indexes of Fig. 3.2.

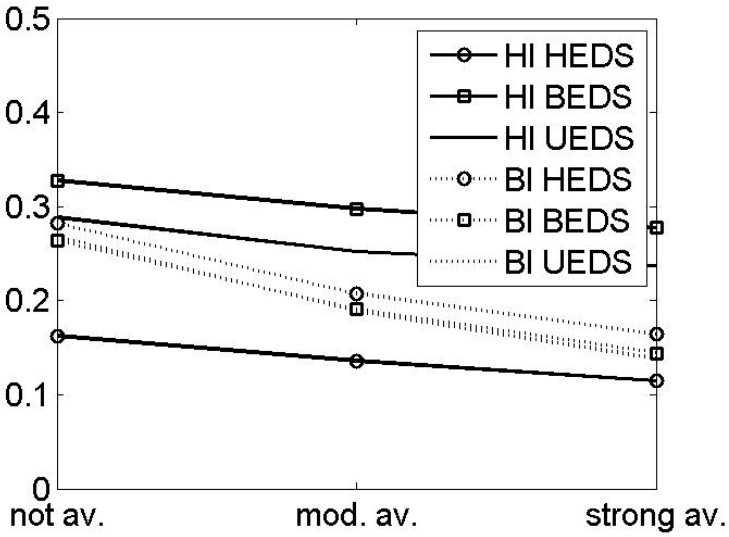

(a) End diastole, segm.

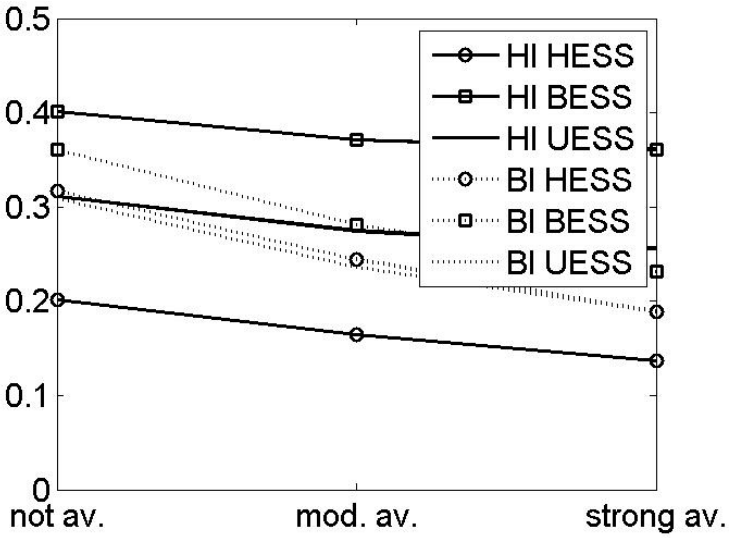

(b) End systole, segm.

Figure 3.4: Fig. 3.4(a) and 3.4(b) show how apparent error rate of Second-Harmonic Imaging HI and Bandwidth Imaging BI in HEDS, BEDS, UEDS, HESS, BESS and UESS behave in various averaging. Notice that the apparent error rate of the Bandwidth Imaging segments are more collected and decreases faster in averaging.

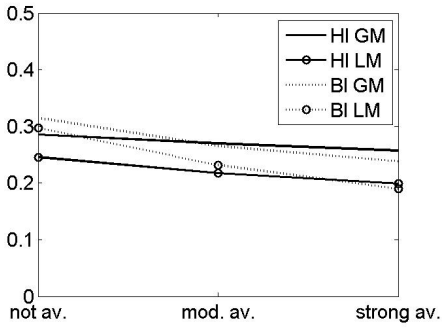

(a) End diastole, four-chamber

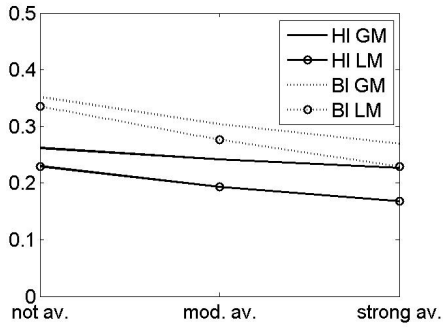

(b) End systole, four-chamber

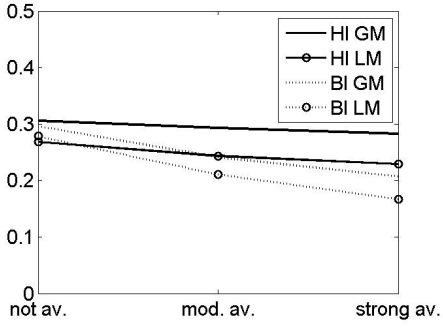

(c) End diastole, two-chamber

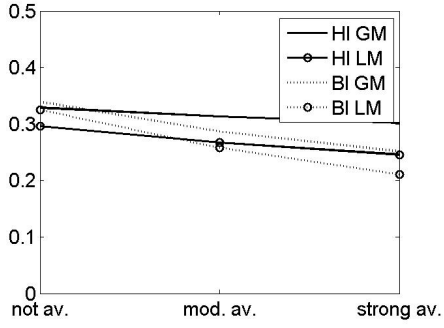

(d) End systole, two-chamber

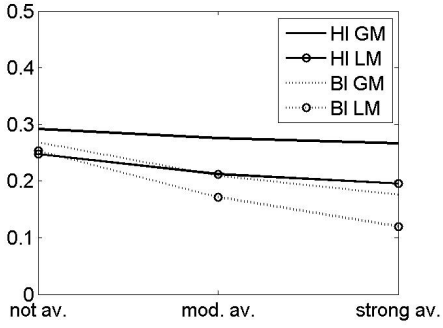

(e) End diastole, long-axis

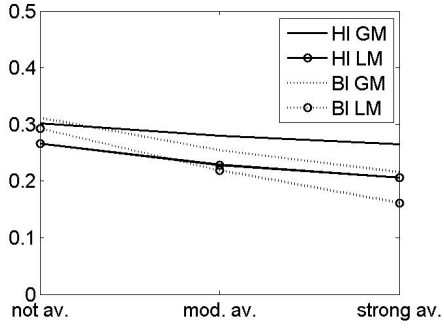

(f) End systole, long-axis

Figure 3.5: The figures show difference between LM and GM in four-chamber, two-chamber and long-axis view in end diastole and end systole, in various averaging. All lines decrease in averaging. If that was not the case, it would not be fair to discuss GM and LM in various averaging.

Table 3.1: Numbers of subjects where GM is lower in Bandwidth Imaging than in Second-Harmonic Imaging

		Four-chamber	Two-chamber	Long-axis
End diastole	Raw	5	6	12
	Mod. av.	8	12	14
	Strong av.	11	15	14
End systole	Raw	0	6	7
	Mod. av.	1	14	10
	Strong av.	3	13	11

Table 3.2: Numbers of subjects where HUM is lower in Bandwidth Imaging than in Second-Harmonic Imaging

		Four-chamber	Two-chamber	Long-axis
End diastole	Raw	14	12	15
	Mod. av.	11	12	11
	Strong av.	10	7	6
End systole	Raw	13	14	15
	Mod. av.	12	12	11
	Strong av.	12	7	8

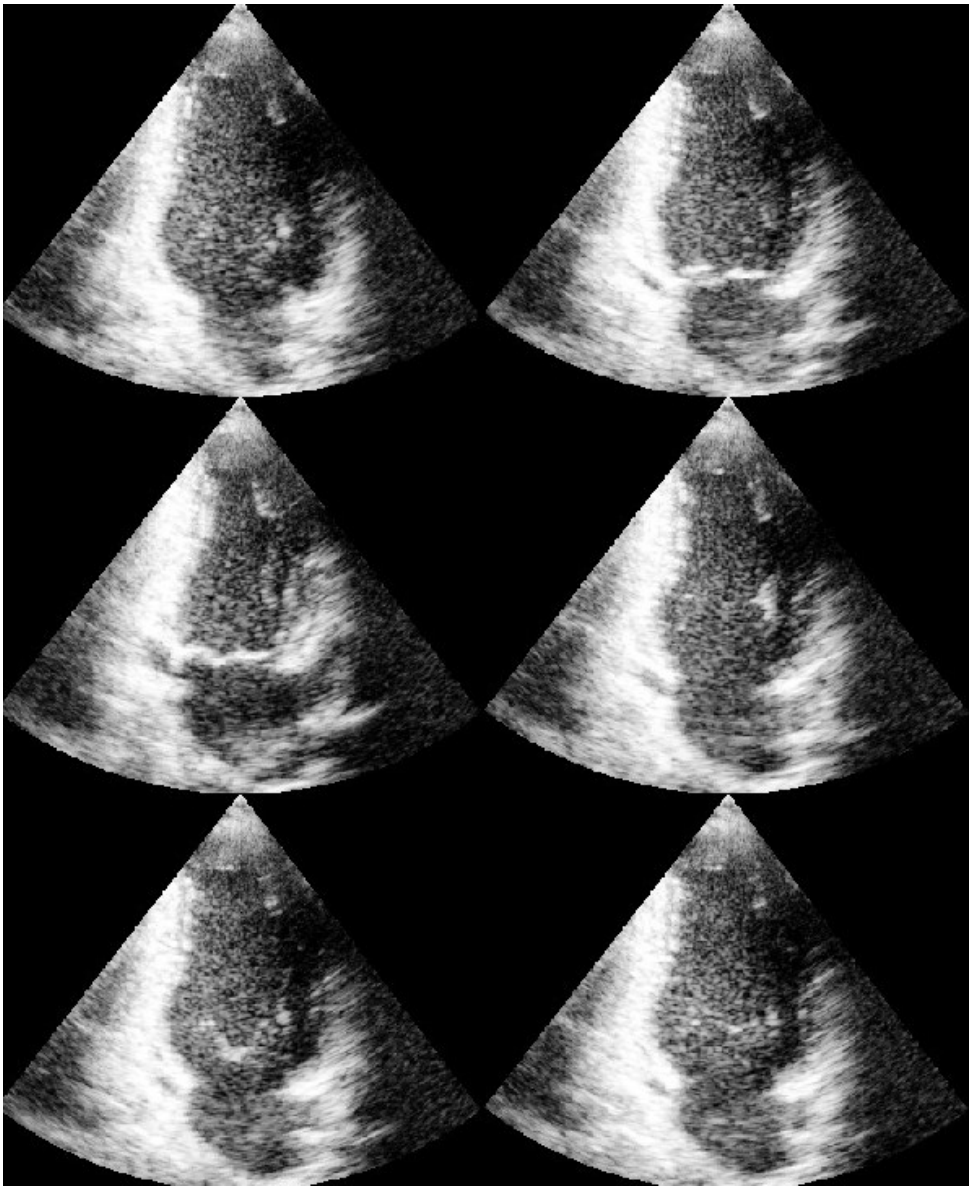

Figure 3.6: Second-Harmonic Images from two-chamber view at six equally spaced time steps in the cardiac cycle.

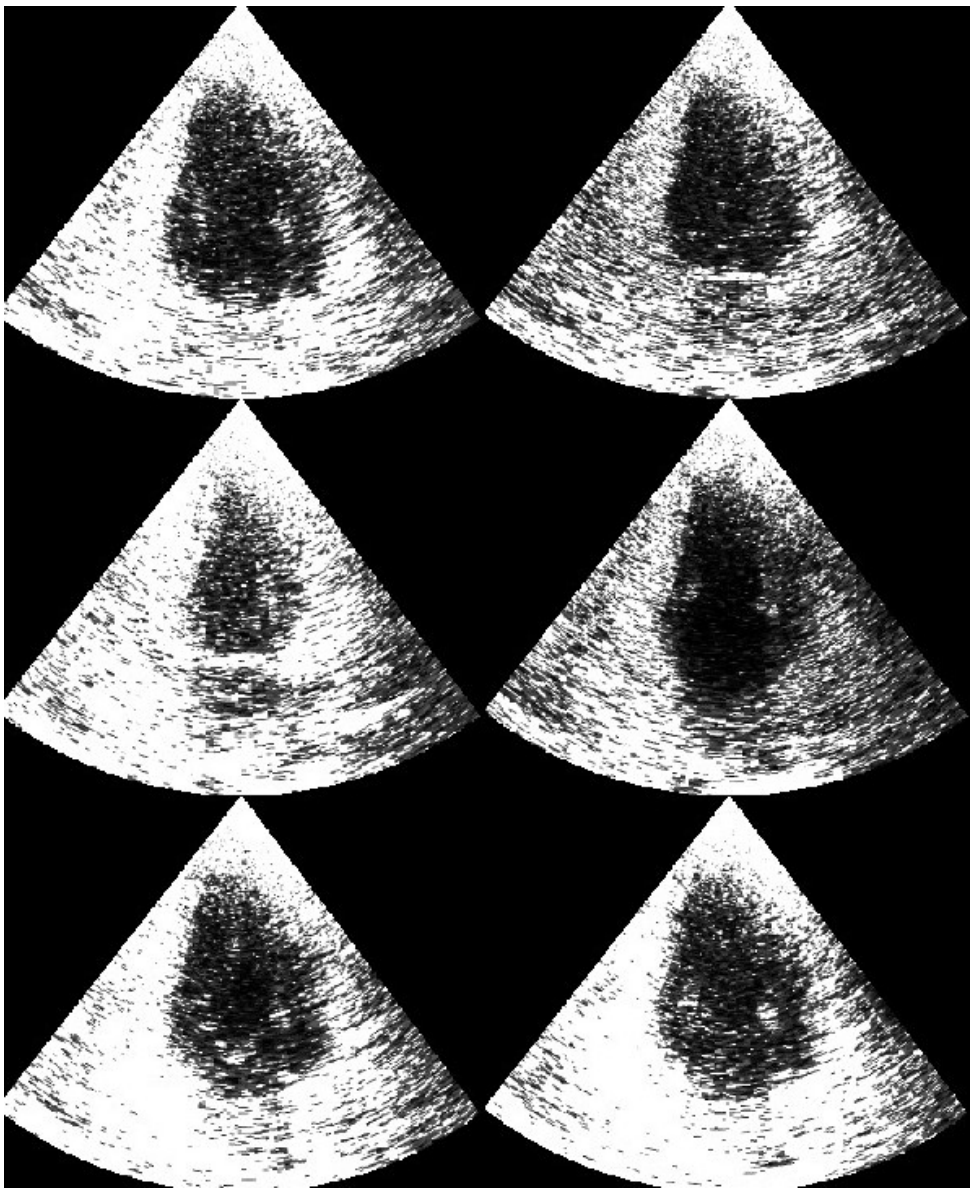

Figure 3.7: Bandwidth Images with no highpass filter prior to the autocorrelation estimate.

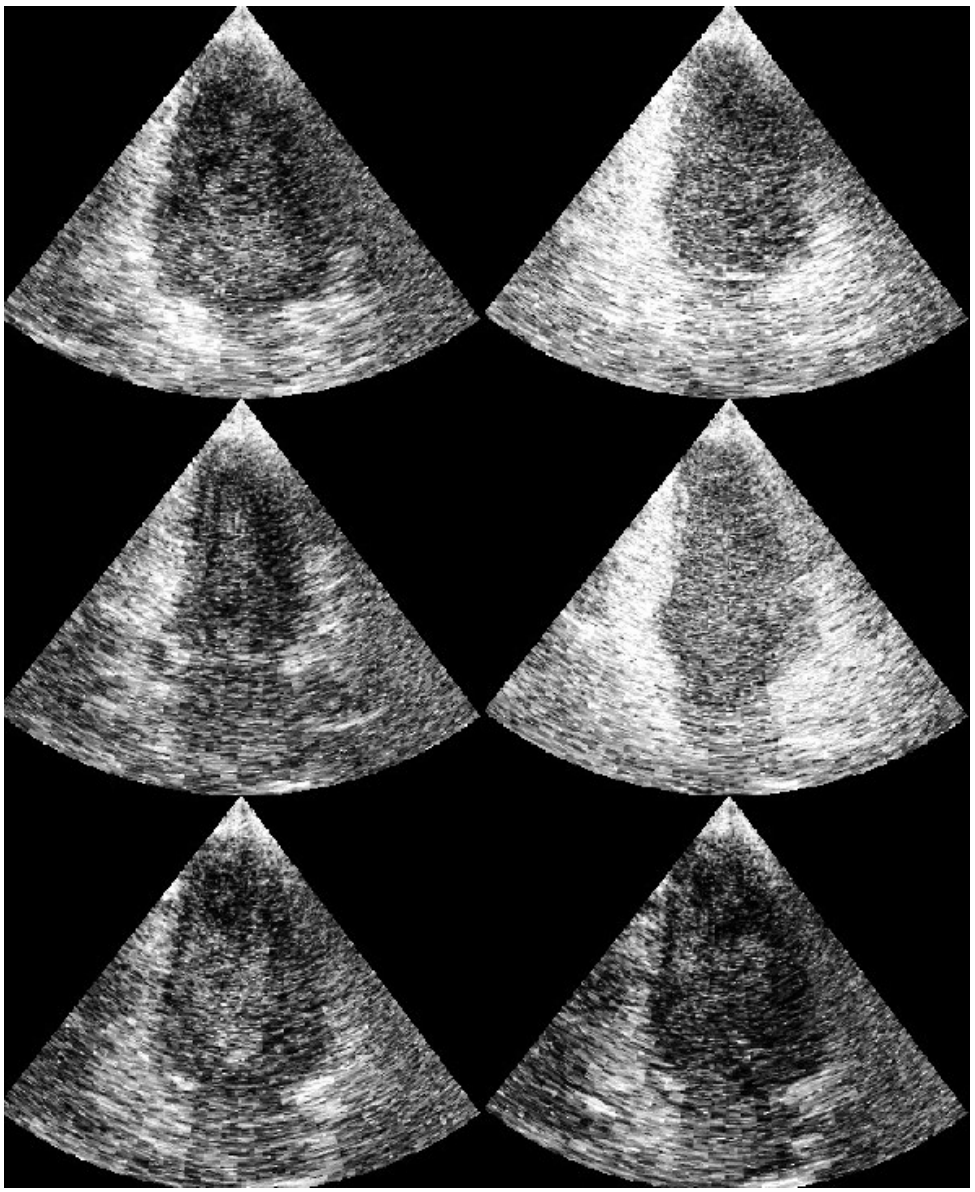

Figure 3.8: Bandwidth Images that are highpass filtered with an attenuation factor of 40 dB.

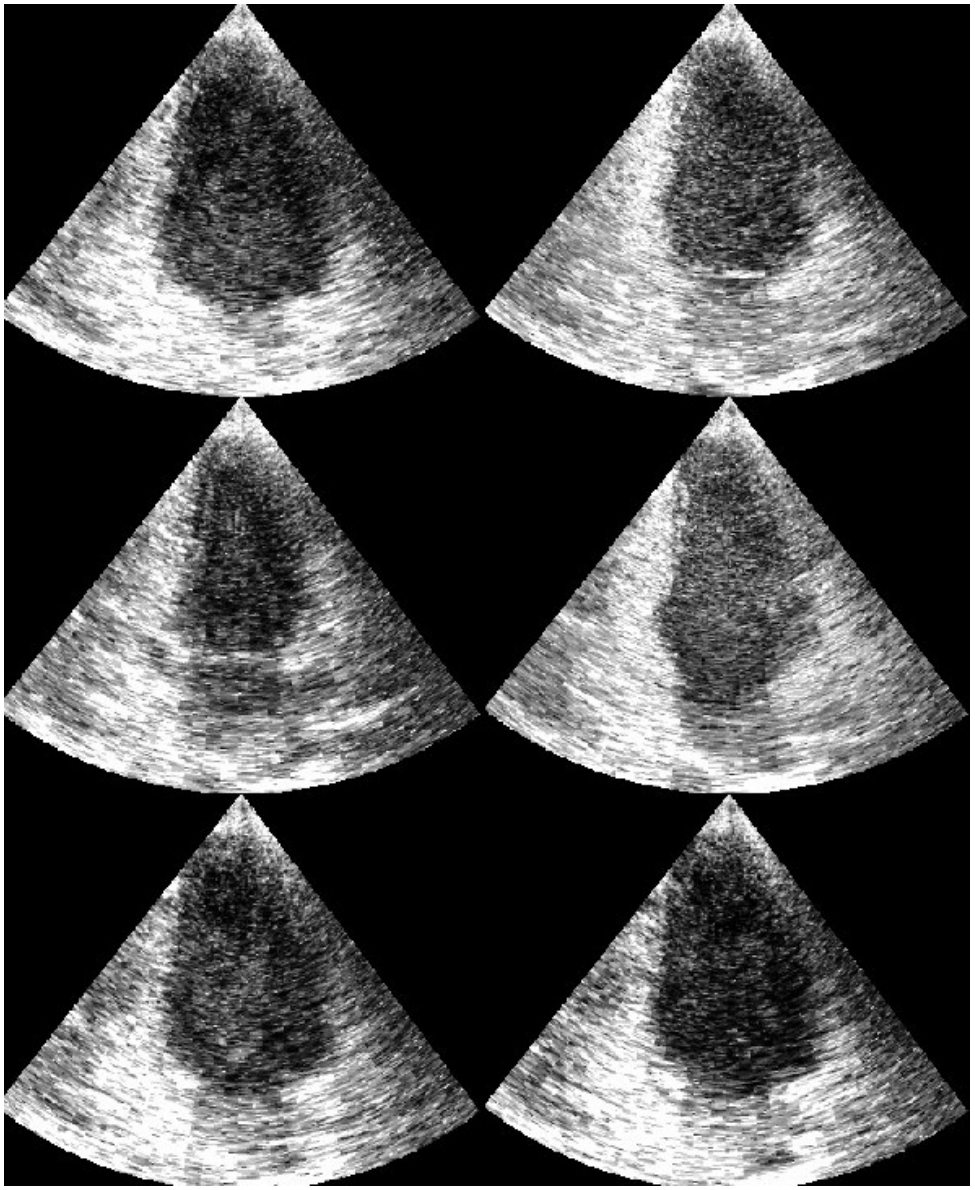

Figure 3.9: Bandwidth Images that are highpass filtered with an attenuation factor that decreases linearly from 40 dB to 15 dB.

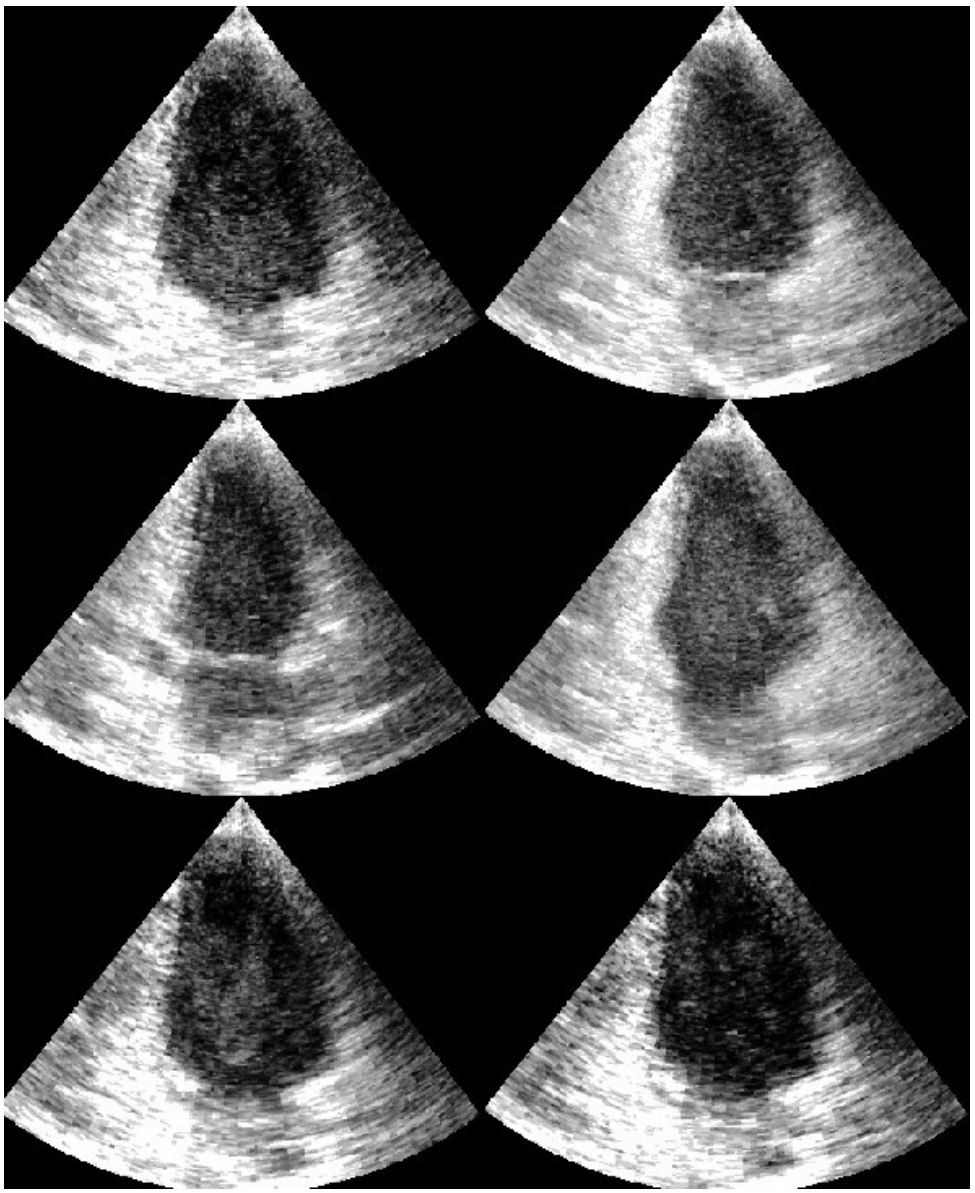

Figure 3.10: The images from Fig. 3.9 are median filtered with a structural element of 3 temporal and 2 radial samples. Here, some of the salt and pepper noise are removed.

Part III

New Doppler-Based Imaging Method in Echocardiography with Applications in Blood/Tissue Segmentation

Abstract

Knowledge Based Imaging is suggested as a method to distinguish blood from tissue signal in transthoracial echocardiography. This method utilizes the maximum likelihood function to classify blood and tissue signal. Knowledge Based Imaging uses the same pulse strategy as Bandwidth Imaging, but is significantly more difficult to implement. Therefore, Knowledge Based Imaging and Bandwidth Imaging are compared with Fundamental Imaging by a computer simulation based on a parametric model of the signal. The apparent error rate is calculated in any reasonable tissue to blood signal ratio, tissue to white noise ratio and clutter to white noise ratio. Fundamental Imaging classifies well when tissue to blood signal ratio is high and tissue to white noise ratio is higher than clutter to white noise ratio. Knowledge Based Imaging classifies also well in this environment. In addition, Knowledge Based Imaging classifies well whenever blood to white noise ratio is above 30 dB. This is the case, even when clutter to white noise ratio is higher than tissue to white noise ratio and tissue to blood signal ratio is zero. Bandwidth Imaging performs similar to Knowledge Based Imaging, but blood to white noise ratio has to be 20 dB higher for a reasonable classification. Also the highpass filter coefficient prior to Bandwidth Imaging calculation is discussed by the simulations. Some images of different parameter settings of Knowledge Based Imaging are visually compared with Second-Harmonic Imaging, Fundamental Imaging and Bandwidth Imaging. Changing parameters of Knowledge Based Imaging can make the image look similar to both Bandwidth Imaging and Fundamental Imaging.

Chapter 1

Introduction

The state of art echocardiographic modes for defining endocardium of left ventricle of the human heart are; Fundamental Imaging, Second-Harmonic Imaging and Left Ventricle Opacification. These methods distinguish blood signal from tissue signal by their differences in power [9].

Alternatively, Doppler signal from blood flow differs from tissue motion, since it is less coherent with depth. In Power Doppler, blood is distinguished from tissue signal by the power of the highpass filtered Doppler signal. Here a packetsize of above 6 is required to achieve the desired filter characteristics [18].

In part II, Bandwidth Imaging was introduced and the experiment indicated that tissue and blood could be distinguished with a packetsize as small as 3. The small packetsize enables a resolution that is interesting for endocardial border definition. In this part, we seek to discuss the theoretical potential of Knowledge Based Imaging and Bandwidth Imaging, where the pulse strategy of the optimized Bandwidth Imaging method is taken as a starting point.

In chapter 2 a parametric models for signal from blood and tissue are outlined and Knowledge Based Imaging is defined. In chapter 3, the apparent error rates of Knowledge Based Imaging, Bandwidth Imaging and Fundamental Imaging are calculated from computer generated signals in various types of noise. In section 3.4, some premature Knowlege based Images with different parameter settings are compared with a Fundamental Image, a Bandwidth Imaging and a Second-Harmonic Image.

Chapter 2

Signal model and definition of Knowledge Based Imaging

Torp et. al. [40] introduced a parametric model for the autocorrelation functions in regions with rectilinear flow, under the assumption that signal is a complex Gaussian process. In this chapter, this model is expanded to yield turbulent flow as well. The signal model is also further expanded to include additive white noise and clutter noise in a similar manner as in Heimdal et. al. [41]. This is the theoretical framework for defining, instrumenting and discussing Knowledge Based Imaging and Bandwidth Imaging.

2.1 Parametric model for the autocorrelation function of signal from blood and tissue

As mentioned above the signal model of [40] is used. Here the authors assume a random continuum model for blood scattering [42]. The spatial fluctuation in mass density and compressibility, which determine the incoherent part of the scattering, is assumed proportional to the fluctuation of blood cell concentration $n_b(\mathbf{r}, t)$, where $\mathbf{r}$ is position and t is time. Here, $n_b(\mathbf{r}, t)$ is a zero mean random process. For a short correlation in space, for a fixed time and neglecting diffusion, the autocorrelation function of $n_b(\mathbf{r}, t)$ is approximated in [42] by

$$\begin{aligned} < n_b(\mathbf{r}, t), n_b(\mathbf{r} + \xi, t + \tau) > &= \boldsymbol{\Upsilon}(\mathbf{r}, t)\, \delta(\xi - \zeta(\mathbf{r}, t, \tau)) \\ \boldsymbol{\Upsilon}(\mathbf{r}, t) &= \frac{var(n_b(\mathbf{r})) \cdot \Delta V}{\Delta V} \end{aligned} \tag{2.1}$$

where $\zeta(\mathbf{r}, t, \tau)$ is the displacement of the fluid element in position $\mathbf{r}$ during the time interval t to $t + \tau$. The function $\boldsymbol{\Upsilon}(\mathbf{r}, t)$ is the variance per unit volume in numbers of blood cells inside a small volume ΔV, and this quantity is proportional to the backscattering coefficient in blood.

Assuming a Gaussian shaped beam profile and a rectangular shaped receiver filter impulse response, the authors outline an expression for the expected value of the two dimensional autocorrelation function for any time and radial lag. In general it is necessary to assume rectilinear flow, but in the case of no radial lag, this assumption has to be valid inside only one range cell. The expected value of the autocorrelation function with only time lag for an electronically steered probe is

$$\begin{aligned} r(m) &= r(0)\beta(m)e^{2\mathrm{i}\,m\;k\,v_1\,T} \\ \beta(m) &= e^{-\frac{3}{2}\,m^2\left[\left(\frac{v_1\,T}{L}\right)^2+\left(\frac{v_2\,T}{\Theta_1}\right)^2+\left(\frac{v_3\,T}{\Theta_2}\right)^2\right]} \end{aligned} \tag{2.2}$$

according to [40]. Here the respective velocity components are v_1, v_2, v_3. Further, L is pulse length, and Θ_1 and Θ_2 are the lateral and elevation resolutions corresponding to -3.25 dB opening angle. The repetition time is T and k is the wave number, which is equal to 2π divided by the wavelength. This model yields for laminar flow. Moreover, flow in left ventricle is turbulent [43], and in the next subsection this model is expanded to yield for turbulent flow as well.

2.2 Model for turbulent blood flow

For turbulent flow we assume that the autocorrelation function for $n_b(\mathbf{r},t)$ is

$$< n_b(\mathbf{r},t), n_b(\mathbf{r}+\xi,t+\tau) >= \boldsymbol{\Upsilon}(\mathbf{r},t)\,\frac{1}{(2\pi)^{\frac{3}{2}}\sigma_1\sigma_2\sigma_3}\,e^{-\frac{1}{2}\left(\frac{(\xi_1-\zeta_1)^2}{\sigma_1^2}+\frac{(\xi_2-\zeta_2)^2}{\sigma_2^2}+\frac{(\xi_3-\zeta_3)^2}{\sigma_3^2}\right)} \tag{2.3}$$

where ζ_1, ζ_2 and ζ_3 are mean displacements and σ_1, σ_2 and σ_3 are standard deviations of displacements. Here we assume a Gaussian shaped velocity profile to describe turbulent flow. With this extra assumption, the development of the expected value of the autocorrelation function $r(m)$ can follow the same path as in paper [40]. The difference is to multiply $r(m)$ with the Gaussian probability density function of velocities and integrate over all velocities.

$$\begin{aligned} r(m) &= r(0)\int_{-inf}^{inf} \partial v_x,\,\partial v_y\,\partial v_z \\ &\beta(m)\,e^{\mathrm{i}\,m\,2\,k\,v_1 T}\,e^{-\frac{1}{2}\left(\frac{(v_x-v_1)^2}{\sigma_1^2}+\frac{(v_y-v_2)^2}{\sigma_2^2}+\frac{(v_z-v_3)^2}{\sigma_3^2}\right)} \end{aligned} \tag{2.4}$$

Here σ_1, σ_2 and σ_3 are redefined as the standard deviations of the velocity components. Further, v_1, v_2 and v_3 refer to the means of the velocity components.

Integrating this gives

$$
\begin{aligned}
r(m) &= r(0)\hat{\beta}(m)\hat{\alpha}(m)\, e^{\mathrm{i}\frac{m\,2\,k\,v_1\,T}{a_1}} \qquad \text{where} \\
\hat{\alpha}(m) &= e^{-\frac{2\,m^2\,k^2\,T^2\,\sigma_1^2}{a_1^2}}, \qquad \hat{\beta}(m) = \frac{1}{a_1\,a_2\,a_3}\, e^{-\frac{3}{2}m^2\left[\left(\frac{v_1\,T}{L\,a_1}\right)^2+\left(\frac{v_2\,T}{\Theta_1\,a_2}\right)^2+\left(\frac{v_3\,T}{\Theta_2\,a_3}\right)^2\right]}, \\
a_1 &= \sqrt{3m^2\frac{\sigma_1^2\,T^2}{L^2}+1}, \quad a_2 = \sqrt{3m^2\frac{\sigma_2^2\,T^2}{\Theta_1^2}+1} \quad \text{and} \quad a_3 = \sqrt{3m^2\frac{\sigma_3^2\,T^2}{\Theta_2^2}+1}
\end{aligned}
\tag{2.5}
$$

The coefficients a_1, a_2 and a_3 are close to one when $\sigma_1 T$ is small compared to L, $\sigma_2 T$ is small compared to θ_1 and $\sigma_3 T$ is small compared to θ_2. Therefore $\hat{\beta(m)}$ is close to $\beta(m)$. A simplified model for turbulent flow is therefore

$$
r(m) = r(0)\beta(m)\alpha(m)\, e^{\mathrm{i}\,m\,2\,k\,v_1\,T} \quad \text{where} \quad \alpha(m) = e^{-2\,m^2\,k^2\,T^2\,\sigma_1^2} \tag{2.6}
$$

The effect of turbulence is covered in the $\alpha(m)$ parameter, which is a function of the radial velocity distribution alone.

2.3 Model including white noise and clutter noise

Signal is assumed to be described by three components in Heimdal's model [41]. These three components are the signal from the range cell, additive white noise with power σ_n^2 and DC clutter noise from stationary echo with power σ_c^2. We assume the same, and the autocorrelation estimate for blood $r_b(m)$ and for tissue $r_t(m)$ is modeled as:

$$
\begin{aligned}
r_b(0) &= \sigma_b^2 + \sigma_c^2 + \sigma_n^2 \\
r_b(1) &= \sigma_b^2\,\beta(m)\alpha(m)\, e^{\,2\,k\,v_1\,T} + \sigma_c^2 \\
r_b(2) &= \sigma_b^2\,\beta(m)^4\alpha(m)^4\, e^{\,4\,k\,v_1\,T} + \sigma_c^2 \\
\\
r_t(0) &= \sigma_t^2 + \sigma_c^2 + \sigma_n^2 \\
r_t(1) &= \sigma_t^2\,\beta(m)\, e^{\,2\,k\,v_1\,T} + \sigma_c^2 \\
r_t(2) &= \sigma_t^2\,\beta(m)^4\, e^{\,4\,k\,v_1\,T} + \sigma_c^2
\end{aligned}
\tag{2.7}
$$

Notice that the power terms of white noise are zero for $r_b(1)$, $r_t(1)$, $r_b(2)$ and $r_t(2)$. This is because white noise from different shots are uncorrelated. Transversing velocities are neglected in the tissue model and taken into account by the turbulent parameter in the blood model.

The probability density function for a signal $\mathbf{z}$ in blood is P_b and the probability

density function for a signal $\mathbf{z}$ in tissue P_t is

$$\begin{aligned} P_b(\mathbf{z}|\sigma_b,\, \sigma_c,\, \sigma_n,\, v_b,\, \sigma_{v_b}) &= \frac{1}{\pi^N\, |\mathbf{C_b}|}\, e^{\bar{\mathbf{z}}\, \mathbf{C_b^{-1}}\, \mathbf{z}} \\ P_t(\mathbf{z}|\sigma_t,\, \sigma_c,\, \sigma_n,\, v_t) &= \frac{1}{\pi^N\, |\mathbf{C_t}|}\, e^{\bar{\mathbf{z}}\, \mathbf{C_t^{-1}}\, \mathbf{z}} \end{aligned} \tag{2.8}$$

where v_b and v_t are the radial velocity components in blood and tissue and σ_{v_b} is the standard deviation of the velocity profile inside one range cell in blood. Here $\mathbf{C_b}$ and $\mathbf{C_t}$ are:

$$\begin{aligned} \mathbf{C_b} &= \begin{bmatrix} r_b(0) & \overline{r_b(1)} & \overline{r_b(2)} \\ r_b(1) & r_b(0) & \overline{r_b(1)} \\ r_b(2) & r_b(1) & r_b(0) \end{bmatrix} \\ \mathbf{C_t} &= \begin{bmatrix} r_t(0) & \overline{r_t(1)} & \overline{r_t(2)} \\ r_t(1) & r_t(0) & \overline{r_t(1)} \\ r_t(2) & r_t(1) & r_t(0) \end{bmatrix} \end{aligned} \tag{2.9}$$

In general the parameters defining P_b and P_t are not known. If their distributions are known then

$$\begin{aligned} P_b(\mathbf{z}) &= \int_{-\inf}^{\inf} \mathrm{d}\sigma_b, \mathrm{d}\sigma_c, \mathrm{d}\sigma_c, \mathrm{d}v_b, \mathrm{d}\sigma_{v_b} P_b(\mathbf{z}|\sigma_b,\, \sigma_c,\, \sigma_n,\, v_b,\, \sigma_{v_b})\, P_{\sigma_b}\, P_{\sigma_c}\, P_{\sigma_n}\, P_{v_b}\, P_{\sigma_{v_b}} \\ P_t(\mathbf{z}) &= \int_{-\inf}^{\inf} \mathrm{d}\sigma_t, \mathrm{d}\sigma_c, \mathrm{d}\sigma_c, \mathrm{d}v_t, P_t(\mathbf{z}|\sigma_t,\, \sigma_c,\, \sigma_n,\, v_t)\, P_{\sigma_t}\, P_{\sigma_c}\, P_{\sigma_n}\, P_{v_t} \end{aligned} \tag{2.10}$$

where $P_{\sigma_b}\, P_{\sigma_c}\, P_{\sigma_n}\, P_{v_b}\, P_{\sigma_{v_b}}\, P_{\sigma_t}$ and P_{v_t} are the probability density functions for the σ_b, σ_c, σ_n, v_b, σ_{v_b}, σ_t and v_t. In practice, these probability density functions can potentially be found from a priory knowledge, estimation or experimental trial and error.

2.4 Knowledge Based Imaging

The echocardiographic mode Knowledge Based Imaging is proposed as

$$\text{Knowledge Based Imaging} = 20 \cdot \log_{10}\left[\ln\left(\frac{P_t(\mathbf{z}) + P_b(\mathbf{z})}{P_t(\mathbf{z})}\right)\right] \tag{2.11}$$

Here $\mathbf{z}$ is the measured complex signal vector with length equal to packet size. Knowledge Based Imaging is basically a histogram manipulated version of the maximum likelihood ratio of a signal sample. The maximum likelihood ratio is $P_t(\mathbf{z})/P_b(\mathbf{z})$, and this is described in Van Trees [44].

The histogram manipulation can be argued for in the following way: The expression $(P_t(\mathbf{z}) + P_b(\mathbf{z}))/P_t(\mathbf{z})$ is close to 1 when $P_t(\mathbf{z})$ is dominating, equal to 2 when $P_t(\mathbf{z}) = P_b(\mathbf{z})$ and approaches infinity when $P_b(\mathbf{z})$ is dominating. The natural logarithm of this becomes a number between zero and infinity. Notice that this number is dominated by the difference of the exponents in equation (2.8). These exponents are dominated by the power of the signal, and this motivates for the final log compression. This histogram becomes reasonably uniform.

Another interesting method is the generalized likelihood ratio test that is also described in Van Trees. In the case of Knowledge Based Imaging, this is the same as calculating Knowledge Based Imaging from equation (2.11), where $P_t(\mathbf{z})$ and $P_b(\mathbf{z})$ are substituted with $\hat{P}_t(\mathbf{z})$ and $\hat{P}_b(\mathbf{z})$;

$$\begin{aligned}\hat{P}_b(\mathbf{z}) &= \max_{R_b}(P_b(\mathbf{z}|\sigma_b, \sigma_c, \sigma_n, v_b, \sigma_{v_b})) \quad \text{where} \quad (\sigma_b, \sigma_c, \sigma_n, v_b, \sigma_{v_b}) \,\epsilon\, R_b \\ \hat{P}_t(\mathbf{z}) &= \max_{R_t}(P_t(\mathbf{z}|\sigma_t, \sigma_c, \sigma_n, v_t)) \quad \text{where} \quad (\sigma_t, \sigma_c, \sigma_n, v_t) \,\epsilon\, R_t\end{aligned} \tag{2.12}$$

Obviously, Knowledge Based Imaging requires definition of parameter space in tissue R_t and blood R_b. In this manuscript, this is done by defining the upper and lower limits of the parameters. This is hereby referred to as Knowledge Based Imaging with box constraints.

2.5 Fundamental imaging

In the computer simulation, Fundamental Imaging is defined as

$$\text{Fundamental Imaging} = 20\log_{10}(r(0)) \quad \text{where} \quad r(m) = \frac{1}{3}\sum_{n=0}^{3-m-1} \overline{z_n} z_{n+m} \tag{2.13}$$

Note that no highpass filter is used prior to Fundamental Imaging calculation.

2.6 Bandwidth Imaging

A derivation of estimators of the bandwidth, the mean frequency shift and power of the Doppler signal for packetsize 3 is given in Appendix A. In part II Bandwidth Imaging is defined as

$$\text{Bandwidth Imaging} = \frac{|r(1)|}{r(0)} \tag{2.14}$$

and prior to the autocorrelation estimate the signal is filtered with this 2-tap Finite Impulse Response filter

$$\begin{aligned}x_1 &= z_2 - 10^{-\frac{\text{AF}}{20}} z_1 \\ x_2 &= z_3 - 10^{-\frac{\text{AF}}{20}} z_2\end{aligned} \tag{2.15}$$

where AF is the attenuation factor at zero frequency.

Table 2.1: Parameters related to the transducer for Fundamental Imaging, Knowledge Based Imaging and Bandwidth Imaging

Parameter	Value
Center frequency	2.5 MHz
pulse repetition frequency	3.75 kHz
Multi-Line acquisition	4
Packet size	3
Radial resolution	$6.67 \cdot 10^{-4}$ m
Aperture	$2.2 \times 2.0 \cdot 10^{-6}\,\mathrm{m}^2$
Depth	0.15 m
Focal point (single)	0.15 m
Framerate	44
Number of beams	127

2.7 Pulse strategy

The pulse strategy of Bandwidth Imaging, Knowledge Based Imaging and Fundamental Imaging is given in Table 2.1. The center frequency for Bandwidth Imaging, Knowledge Based Imaging and Fundamental Imaging is a trade off between resolution and penetration and is set to 2.5 MHz. The pulse length (0.7 mm) is chosen as a trade off between radial resolution and sensitivity. The pulse repetition frequency is set to 3750 and this choice is argued for in subsection 3.4.4 in part II. The packet size is 3, which is the lowest possible for calculating Bandwidth Imaging with the filter given by equation (2.15).

Chapter 3

Evaluation of Knowledge Based Imaging, Bandwidth Imaging and Fundamental Imaging by computer simulation

3.1 Methods

In this chapter the classification functions Knowledge Based Imaging, Bandwidth Imaging and Fundamental Imaging are evaluated and compared using the quantity apparent error rate. A comprehensive discussion of classification theory can be found in [38]. Here apparent error rate is defined as

$$\text{Apparent error rate} = \frac{n_{bM} + n_{tM}}{n_b + n_t} \tag{3.1}$$

where, n_t and n_b are the sizes of measured data from tissue π_t and blood π_b. Further, n_{tM} and n_{bM} are the numbers of misclassifications of π_t and in π_b. Apparent error rate is simply the proportion of misclassifications of the total dataset. Obviously, the numbers of misclassifications are a function of the threshold level. In this experiment the best threshold is used, and apparent error rate is therefore independent of any monotone transformations of π_t and π_b. The definition of apparent error rate is changed to;

$$\text{Apparent error rate} = \min_T \left(\frac{n_{bMT} + n_{tMT}}{n_b + n_t} \right) \tag{3.2}$$

where the number of misclassifications in blood and tissue with threshold T, are denoted n_{bMT} and n_{tMT}, respectively.

In this experiment, 2000 signal samples from blood and 2000 signal samples from tissue are generated from a random generator. Here the pulse strategy is given in Table 2.1, which is the same pulse strategy as in chapter 3 in part II. Speed of

sound c is 1540m/s. Blood signal $\mathbf{z_b}$ and tissue signal $\mathbf{z_t}$ are created by

$$\begin{aligned} \mathbf{z_b} &= \mathbf{L_b}\,\mathbf{x_1} \qquad \mathbf{C_b} = \mathbf{L_b}^T\mathbf{L_b} \\ \mathbf{z_t} &= \mathbf{L_t}\,\mathbf{x_2} \qquad \mathbf{C_t} = \mathbf{L_t}^T\mathbf{L_t} \end{aligned} \tag{3.3}$$

where $\mathbf{x_1}$ and $\mathbf{x_2}$ are normalized complex Gaussian signal created by the random generator. Moreover, $\mathbf{L_t}$ and $\mathbf{L_b}$ are the lower triangular matrices, obtained by Cholesky factorization of $\mathbf{C_b}$ and $\mathbf{C_t}$ given in equation (2.9). Fundamental Imaging is calculated by equation (2.13), Knowledge Based Imaging by equation (2.11), and Bandwidth Imaging by equation (2.14).

For simplicity $\mathbf{C_b}$ and $\mathbf{C_t}$ are divided by σ_n^2, so that apparent error rate is discussed for various blood to white noise ratio, tissue to white noise ratio, and clutter to white noise ratio. It is also interesting to discuss the ratio between tissue and blood signal.

The parameters v_t and v_b are picked randomly from two Gaussian distributions with mean zero and standard deviation 0.025 m/s and 0.25 m/s, respectively. The parameter σ_{v_b} is set to zero in simulations where laminar flow is assumed. In simulations where turbulent flow is assumed σ_{v_b} is chosen to 0.1 m/s.

3.2 Results

In Fig. 3.1 and in the first column of Fig. 3.2, apparent error rate is color coded to show its level at any tissue to white noise ratio, clutter to white noise ratio and tissue to blood signal ratio. The color bar goes from 0 (red) to 0.5 (blue). All these subplots show tissue to white noise ratio (y-axis) versus clutter to white noise ratio (x-axis) from 0 to 140 dB. In the bottom row tissue to blood signal ratio is 0 db, and this ratio increases by increment of 10 dB in the next rows.

In the first column, blood and tissue signal are separated by Fundamental Imaging. Obviously apparent error rate is dependent on tissue to blood signal ratio, and it is necessary that clutter to white noise ratio is lower than tissue to white noise ratio for reasonable classification.

In column two, blood and tissue signal are separated by Knowledge Based Imaging. Here the velocity distributions of tissue and blood have standard deviations of 0.025 m/s and 0.25 m/s, respectively. The turbulence parameter is set to zero. We see that Knowledge Based Imaging classifies better than Fundamental Imaging everywhere. Note that a reasonable classification is possible whenever blood to white noise ratio is above 30 db, regardless of tissue to blood signal ratio and clutter to white noise ratio. This can be seen by noting the relation tissue to white noise ratio = tissue to blood signal ratio + blood to white noise ratio. This effect is even stronger in the third column, where the turbulence parameter in blood is turned up to 0.1 m/s.

In the case of Bandwidth Imaging, only one parameter has to be set, namely AF. The same signal as in third column of 3.1 , is highpass filtered by different

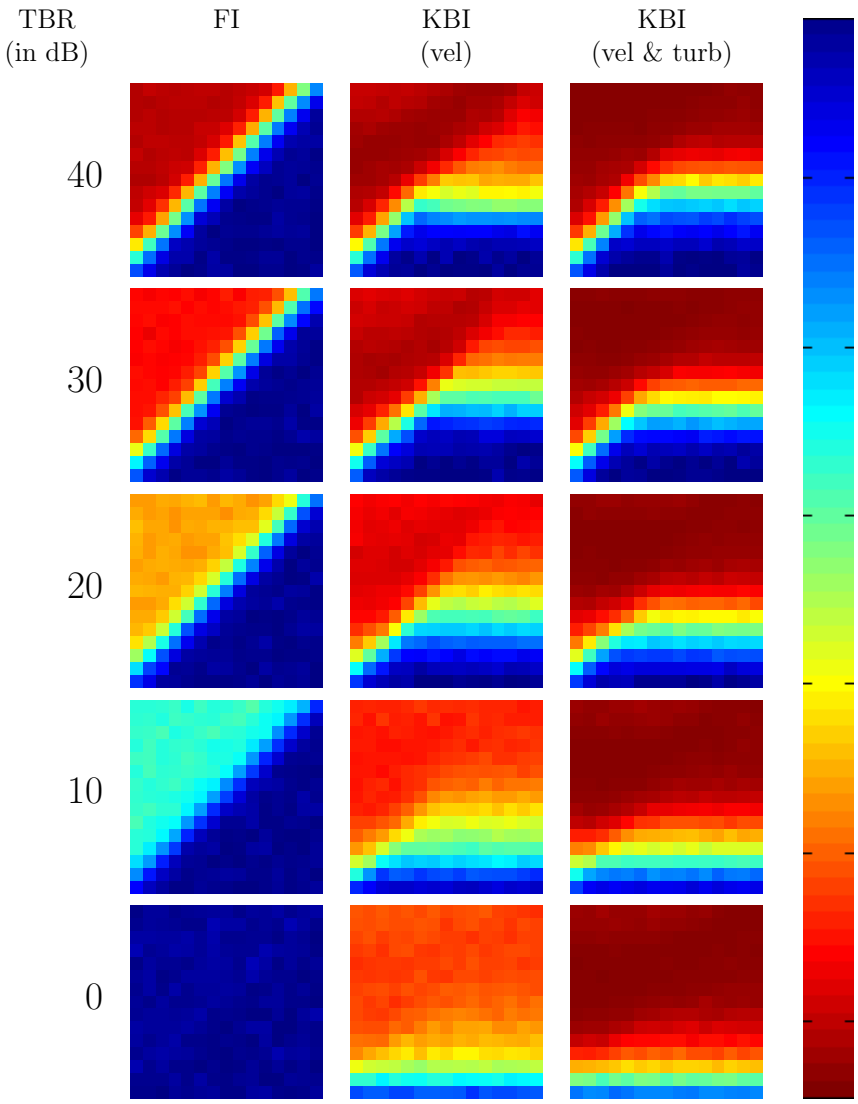

Figure 3.1: Apparent error rate is color coded from 0 (red) to 0.5 (blue). All subplots show tissue to white noise ratio (x-axis) versus clutter to white noise ratio (y-axis) from 0 to 140 dB. In the first row tissue to blood signal ratio TBR is 0 db and in the next rows this ratio increases by increment of 10 dB to 40 dB. In the first column blood and tissue signals are separated by Fundamental Imaging FI. Apparent error rate is dependent on tissue to blood signal ratio and that clutter to white noise ratio is lower than tissue to white noise ratio. In column the separation is done by Knowledge Based Imaging KBI. Here the velocity distributions of tissue and blood have standard deviations of 0.025 m/s and 0.25 m/s, respectively. KBI classifies well as long as blood to white noise ratio is above 30 dB. This effect is stronger in the next column, where the turbulence parameter in blood is set to 0.1 m/s.

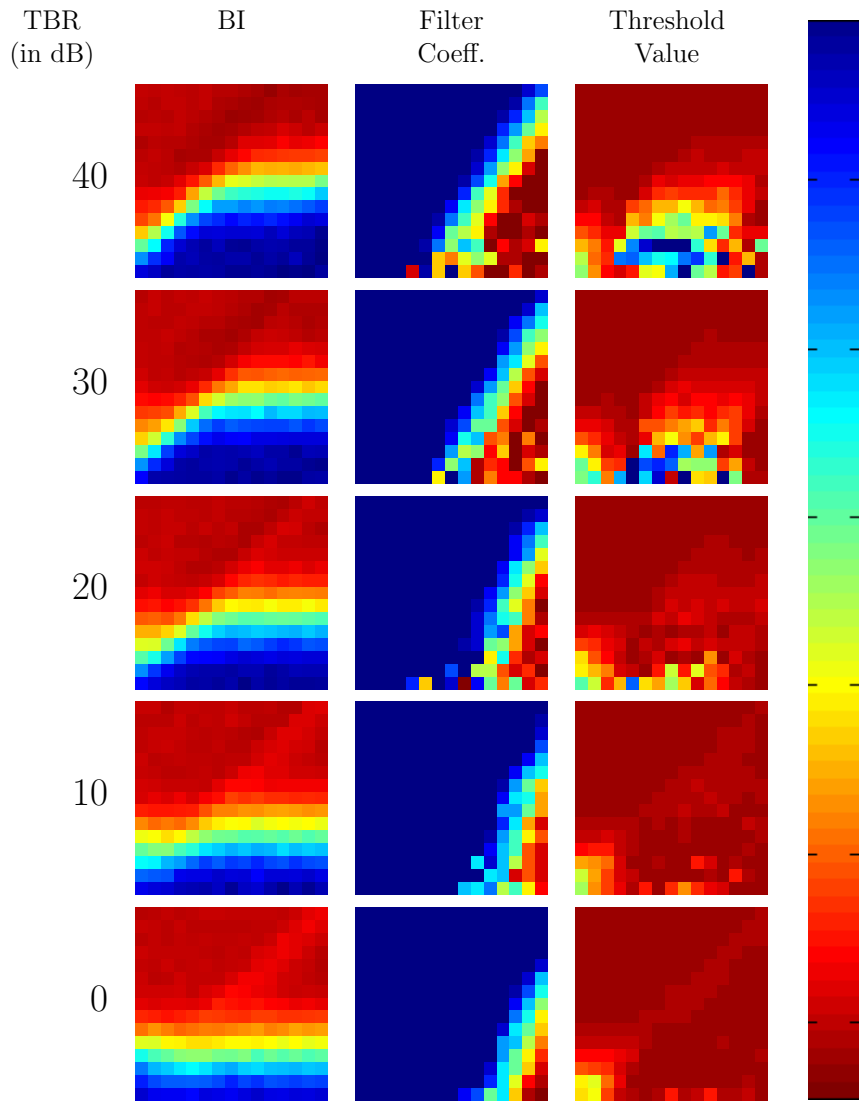

Figure 3.2: The table shows color coded apparent error rate of Bandwidth Imaging BI in the first column. Here the signal has the same parameters as in Fig. (3.1). The second column shows attenuation factor at zero frequency from 0 dB (blue) to 50 dB (red). The attenuation factor seems linearly dependent on clutter to white noise ratio and blood to white noise ratio. The last column shows the best threshold level for Bandwidth Imaging classification. The scale is 0 (blue) to 1 (red). It is important to see that this level is quite uniform in the regions where Bandwidth Imaging classify well.

AF ranging from 0 to 50 dB. The AF that minimizes apparent error rate is chosen, and the best value of apparent error rate is shown in the first column in Fig. 3.2. Bandwidth Imaging performs similar to Knowledge Based Imaging, but the general trend is that blood to white noise ratio has to be 20 dB higher for the same level of apparent error rate. It is also important to mention that Bandwidth Imaging performs worse than Fundamental Imaging in regions where tissue to blood signal ratio is high, tissue to white noise ratio low and clutter to white noise ratio smaller than tissue to white noise ratio.

The second column of Fig. 3.2 shows the best possible AF on a scale from 0 (blue) to 50 dB (red). It is seen that AF is smooth in regions where Bandwidth Imaging classify well. This coefficient seems linearly dependent on blood to white noise ratio and clutter to white noise ratio. The last column shows the best threshold level on a scale from 0 (blue) to 1 (red). Here we see that the threshold level seems smooth and not AF-dependent in regions where Bandwidth Imaging classify well.

3.3 Discussion of computer simulation

In this signal model we assumed one and the same pulsestrategy for Bandwidth Imaging, Knowledge Based Imaging and Fundamental Imaging. If different pulsestratgies were compared, the results would be very dependent on the signal model. In that case, the signal model had to be validated for every choice of pulse strategies. In our case, we simply have to assume that the backscattered signal can be described by these three components; signal from blood or tissue in a range cell, uncorrelated white noise and stationary clutter noise.

It can be argued that Fundamental Imaging does not have optimized pulse strategy and the comparison is therefore favoring Knowledge Based Imaging. Moreover, the state of art echocardiographic mode is Second-Harmonic Imaging, which is reported to be an improvement compared to Fundamental Imaging [6]. The aim of this comparison is therefore not to determinate whether Knowledge Based Imaging or Bandwidth Imaging are better than conventional methods. The aim is rather to outline differences in how Knowledge Based Imaging, Bandwidth Imaging and Fundamental Imaging classify in various types of noise.

For the same reason, the computer simulation covers only a subset of all types of signal and noise environments that can be expected in transthoracial echocardiography. This subset is limited in three ways.

First, the velocity distributions of scatterers in π_t and π_b are assumed Gaussian with standard deviation 0.025 m/s and 0.25 m/s. These distributions are chosen, because they seem reasonable at depth 7.5 cm from apical views. Other velocity distributions could be chosen as well. For instance, the velocity of the atrial ventricular plane is normally above 0.085 m/s in end systole and the velocity of the mitral flow yet can exceed 1 m/s. It is important to mention that pulse repetition frequency can be adjusted to get optimal classification for any two samples of blood and tissue

signal. Hence, the difference in velocity distributions is the governing parameter.

Next, blood flow in left ventricle is found to be turbulent by Schoephoerster and Chandran [43]. Turbulence comes into the model, by the assumption that the scatterers in a range cell have a Gaussian velocity distribution with standard deviation 0.1 m/s. This argument could be challenged, both because of the shape of the distribution and also the size of the standard deviation.

And third, the assumption that clutter noise comes only from stationary signal could be challenged. This is because clutter noise also comes from moving tissue.

In the experiment, apparent error rate is used to estimate the true optimal error rate. In [38] apparent error rate is reported to underestimate the true optimal error rate, because the data used to build the classification rule is also used to evaluate the rule. However, this underestimation is reduced by using a large sample size.

In transthoracial echocardiography the clutter level is high in the near-field, due to the penetration of inhomogeneous tissue. Also the level of white noise increases downward the beam, due to depth gain compensation. The above results indicate that the greatest potential of Knowledge Based Imaging is in the apical region, where high clutter to white noise ratio can be compensated by high blood to white noise ratio.

Bandwidth Imaging performed similar to Knowledge Based Imaging, but the general trend is that blood to white noise ratio had to be about 20 dB higher for the same level of apparent error rate. This can explain why the best results of Bandwidth Imaging were found in apical segments in the experiment in chapter 3 in part II . In column two in figure 3.1, AF is plotted in different types of noise. This coefficient seems linearly dependent of blood to white noise ratio and clutter to white noise ratio in the dB scale. This may explain why it seems reasonable to use a depth dependent clutter rejection filter prior to the Bandwidth Imaging calculation in chapter 2 in part II.

In the next section the attention is drawn back to Knowledge Based Imaging, where some premature images are discussed.

3.4 Discussion of instrumentation of Knowledge Based Imaging

The strategy for implementation of Knowledge Based Imaging is to use the pulse strategy of Table 2.1 on a scanner (Vivid 7, GE Vingmed Ultrasound AS (Horten)). If we use the generalized maximum likelihood definition of Knowledge Based Imaging with box constraints, there are 14 parameters to adjust. These are the upper and lower limits of σ_t,σ_b,σ_c,σ_n,v_t,v_b and σ_{v_b}. This section contains some examples of instrumentation of Knowledge Based Imaging with box constraints. In this case, the box constraints can be tuned so Knowledge Based Imaging can look similar to both Bandwidth Imaging and Fundamental Imaging.

Knowledge Based Imaging at one range cell is calculated in this way: A five

dimensional array of values of $\sigma_b, \sigma_c, \sigma_n, v_b$ and σ_{v_b} is created and limited by the box constraints. Next, all $P_b(\mathbf{z})$ are calculated and the maximum value determined. A similar path is followed to calculate maximum of $P_t(\mathbf{z})$. Finally, Knowledge Based Imaging is calculated by equation (2.11).

Fig. 3.3 shows six four-chamber view images of a healthy mature male with different echocardiographic modes. Fig. 3.3(a), 3.3(c) and 3.3(e) show Second-Harmonic Imaging, Fundamental Imaging and Bandwidth Imaging, respectively.

Fig. 3.3(b), 3.3(d) and 3.3(f) show three variants of Knowledge Based Imaging. In these images, σ_n is set to increase from 10 dB to 20 dB downward in the image. In Fig. 3.3(d) KBI 2 is shown. Here, v_b and v_t are set at 7 steps between - 1 to 1 m/s. Here, σ_{v_b} and σ_c are both set to zero. The only parameters separating $\hat{P}_t(\mathbf{z})$ and $\hat{P}_b(\mathbf{z})$, are σ_b and σ_t. These are given at 3 equally spaced steps from 50 to 100 dB in blood and 120 to 150 dB in tissue. We see that the KBI 2 is similar to Fundamental Imaging. They are related in the way that they both separate blood from tissue signal by their difference in power.

KBI 3 is shown in Fig. 3.3(f). Here there is no separation by power at all and σ_b and σ_t are set in three steps between 40 to 140 dB. The separation between blood and tissue signal is by velocity and velocity distribution. Here, v_b is set at seven steps between - 1 to 1 m/s. Further, the magnitude of velocity in tissue v_t is limited by 0.013 m/s in the apical region, and this magnitude is increased linearly to 0.13 m/s at 15 cm depth. This is because the radial velocities in myocardium are higher in the atrial ventricular plane region, than closer to apex. Moreover, the turbulence parameter σ_{v_b} is set to 0.12 m/s. It is important to mention that the image is enhanced by setting this parameter. Also the clutter parameter is set. The clutter parameter is set to decrease linearly downward in the image from 140 to 80 dB. The net effect of setting this parameter is similar to clutter filtering in Bandwidth Imaging. It is interesting that KBI 3 becomes similar to Bandwidth Imaging. The fact that Knowledge Based Imaging can be adjusted between the two extremes that look similar to Fundamental Imaging and Bandwidth Imaging, indicates that Knowledge Based Imaging can be used to find an optimal imaging method that compromises these two extremes.

KBI 1 is shown in Fig. 3.3(b). KBI 1 is a mixture of these two extreme ways of setting parameters of Knowledge Based Imaging. Here the velocity, velocity distributions and clutter parameter are the same as for KBI 3 and the power settings are the same as for KBI 2. This gives hope for finding an optimized imaging setup of Knowledge Based Imaging that balances the advantages of Bandwidth Imaging and Fundamental Imaging. More images are shown in Appendix D.

3.5 Conclusion

Knowledge Based Imaging is proposed as a Doppler-based method to distinguish left-ventricular blood pool from myocardial wall in echocardiographic images. A

computer simulation is used to outline differences in how Knowledge Based Imaging, Bandwidth Imaging and Fundamental Imaging classify in various types of noise. Fundamental Imaging classifies well in environment where tissue to blood signal ratio is high and clutter to white noise ratio is lower than tissue to white noise ratio. Knowledge Based Imaging classifies also well in this environment. In addition Knowledge Based Imaging classifies well as long as blood to white noise ratio is above 30 dB, regardless of the clutter to white noise ratio and the tissue to blood signal ratio. This motivates for a better tissue differentiation in apical areas.

Moreover, Bandwidth Imaging classifies similar to Knowledge Based Imaging, but blood to white noise ratio has to be 20 dB higher to get the same value of apparent error rate. Also, the simulations show that the optimal filter coefficient prior to the autocorrelation estimate is linearly dependent of blood to white noise ratio and clutter to white noise ratio. This argues for the linearly dependent filter coefficient suggested in chapter 2 in part II.

A few images of Knowledge Based Imaging are supplied in this paper, showing that Knowledge Based Imaging can be adjusted to look similar to both Fundamental Imaging and Bandwidth Imaging.

Finally, we acknowledge that more optimization and research are needed for a clinical valuable implementation of Knowledge Based Imaging. First, the implementation should be real time, and the challenges here are the maximizations in equation (2.12) or integrations in equation (2.10). In the case of maximisations in equation (2.12), the maximizations could be done by a Preconditioned Conjugate Gradient Method.

Second, the box constraints of Knowledge Based Imaging have to be set everywhere in the image. To some degree they could be found. The level of white noise could be measured, while the transmitter is turned off. The velocity and turbulence parameters in tissue and blood could be found from a priory knowledge. Further, the signal characteristic could potentially be estimated by for instance a Levenberg-Marquardt method with box constraints [45]. Also, the potential of manual adjustment of parameters may also be investigated.

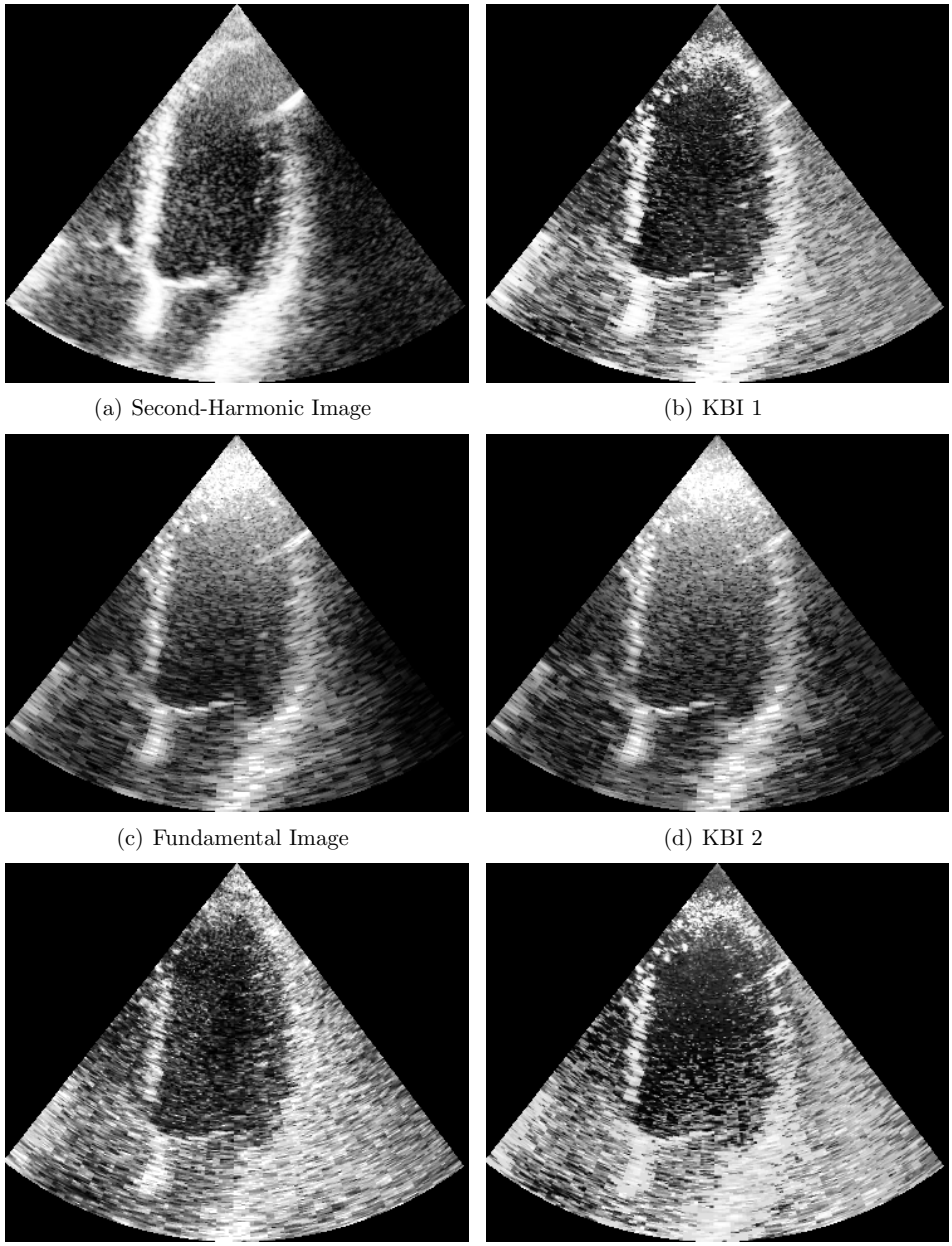

(a) Second-Harmonic Image (b) KBI 1

(c) Fundamental Image (d) KBI 2

(e) Bandwidth Image (f) KBI 3

Figure 3.3: Four-chamber views with different imaging modes. Fig. 3.3(a), 3.3(c) and 3.3(e) show Second-Harmonic Image, Fundamental Image and Bandwidth Image respectively. In Fig. 3.3(b), 3.3(d) and 3.3(f) three variants of Knowledge Bssed Images are shown. In Fig. 3.3(d) power differentiation is emphasized and this image is therefore similar to Fig. 3.3(c). In Fig. 3.3(f) velocity and turbulence differences are emphasized and this image is therefore similar to Fig. 3.3(e). Fig. 3.3(b) shows an image which is a combination of the settings in Fig. 3.3(d) and 3.3(f).

Part IV

Appendices

Appendix A

Spectral parameters of the power spectrum

In Color Flow Imaging power P, mean frequency shift ω_1 and bandwidth B are most commonly estimated from the autocorrelation function. These estimators can be defined from the zero, first and second order central moments of the power spectrum $G(\omega)$

$$\begin{aligned} P &= \frac{1}{2\pi}\int_{-\pi}^{\pi} \mathrm{d}\omega G(\omega) \\ 0 &= \int_{\omega_1-\pi}^{\omega_1+\pi} \mathrm{d}\omega G(\omega)(\omega-\omega_1) \\ B^2 &= \frac{1}{2\pi P}\int_{\omega_1-\pi}^{\omega_1+\pi} \mathrm{d}\omega G(\omega)(\omega-\omega_1)^2 \end{aligned} \tag{A.1}$$

Note that the integration limits are dependent and centered around ω_1. This is an important generalization from simply integrating from $-\pi$ to π as in [9].

A.1 Estimation of power spectrum

A well known estimation of the power spectrum is the periodogram which is defined as

$$G(\omega) = \frac{1}{N}|Z(\omega)|^2 = \frac{1}{N}\left|\sum_{n=0}^{N-1} z_n e^{-j\omega n}\right|^2 \tag{A.2}$$

where z_n are the signal samples and $Z(\omega)$ is the corresponding Fourier transform and N is the packet size. Another definition of $G(\omega)$ is

$$G(\omega) = \sum_{m=1-N}^{N-1} r(m)e^{-j\omega m} \tag{A.3}$$

where $r(m)$ is the autocorrelation function

$$\begin{aligned} r(m) &= \frac{1}{N}\sum_{n=0}^{N-m-1} \overline{z_n} z_{n+m} \qquad \text{for} \qquad 0 \leq m \leq N-1 \\ r(m) &= \frac{1}{N}\sum_{n=|m|}^{N-1} \overline{z_n} z_{n+m} \qquad \text{for} \qquad 1-N \leq m \leq -1 \end{aligned} \tag{A.4}$$

In this chapter the last estimator of $G(\omega)$ is chosen, and estimates for P, ω_1 and B are found from this estimator.

A.2 Estimators of power, mean frequency shift and bandwidth

We use the relation $r(-m) = \overline{r(m)}$, rearrange the sequence in the sum and use the cosine relation. This gives

$$\begin{aligned} G(\omega) =& r(0) + \sum_{m=1}^{N-1} r(m)e^{-j\omega m} + \overline{r(m)}e^{j\omega m} \\ =& r(0) + 2\sum_{m=1}^{N-1} |r(m)| \cos(m\omega - \angle r(m)) \end{aligned} \tag{A.5}$$

where $\angle r(m)$ indicates the complex phase of $r(m)$. Inserting the expression for $G(\omega)$ into (A.1) and performing the integration gives the following relations for

$$\begin{aligned} P =& r(0) \\ \omega_1 =& \omega_1 + \frac{2}{r(0)}\sum_{m=1}^{N-1} \frac{(-1)^m}{m} |r(m)| \sin(m\omega_1 - \angle r(m)) \\ B^2 =& \frac{\pi^2}{3} + \frac{2}{r(0)}\sum_{m=1}^{N-1} \frac{(-1)^m}{m^2} |r(m)| \cos(m\omega_1 - \angle r(m)) \end{aligned} \tag{A.6}$$

In the middle equation the alternating sum is equal to zero, yielding an expression for ω_1. The bandwidth estimator is similar to

$$B^2 = 2 - 2\frac{|r(1)|}{r(0)} \tag{A.7}$$

which was found by [9] and [8]. In the special case with packet size 3 the 2-tap Finite Impulse Response filter reduces N to 2, $G(\omega)$ becomes

$$G(\omega) = r(0) + |r(1)| \cos(\omega - \angle r(1)) \tag{A.8}$$

so the power spectrum is a phase shifted cosine plus a constant. It is quite intuitive that the bandwidth is dependent on the ratio of the cosine amplitude and the constant. The estimators of (A.6) reduce to

$$\begin{aligned} P &= r(0) \\ \omega_1 &= \angle r(1) + k\,\pi \qquad k \text{ is even} \\ B^2 &= \frac{\pi^2}{3} - 2\frac{|r(1)|}{r(0)} \end{aligned} \tag{A.9}$$

Note that in the last part of second equation of (A.9) k is restricted to even integers. This is because the odd solutions give a higher bandwidth estimate than the even. This ensures that ω_1 is at the "center of gravity of $G(\omega)$". Due to the ω_1 dependence of the integration limits of (A.1) ω_1 and B^2 are not distorted when scatterers are moving at a speed close to the Nyquist velocities. The ambiguity of ω_1 is the aliasing effect. It is interesting to see that for white noise we get the desired $\pi/\sqrt{3}$ RMS (root mean square) bandwidth instead of $\sqrt{2}$, which is thirty percent too low.

Appendix B

Discussion of classification criteria

A comprehensive discussion of classification theory can be found in [38]. The minimum total expected cost of misclassification MECM can be evaluated if prior probabilities, probability density functions and also the cost of misclassification are known. If we assume that the costs of misclassification in the blood population π_b and the tissue population π_t are equal, then MECM reduces to the total probability of misclassification TPM, which is given by

$$\begin{aligned} \text{TPM} &= P(\text{observation comes from } \pi_b \text{ and is misclassified}) \\ &\quad + P(\text{observation comes from } \pi_t \text{ and is misclassified}) \\ &= p_b \int_{R_t} f_b(\mathbf{x})\, \mathrm{d}\mathbf{x} + p_t \int_{R_b} f_t(\mathbf{x})\, \mathrm{d}\mathbf{x} \end{aligned} \tag{B.1}$$

where p_b and p_t are prior probabilities and $f_b(\mathbf{x})$ and $f_t(\mathbf{x})$ are probability densities associated with π_b and π_t. The optimal error rate is the value that minimizes TPM. If the probability densities $f_b(\mathbf{x})$ and $f_t(\mathbf{x})$ are known, then the regions R_b and R_t that minimizes TPM are determined by

$$R_b: \quad \frac{f_b(\mathbf{x})}{f_t(\mathbf{x})} \geq \frac{p_t}{p_b} \qquad R_t: \quad \frac{f_b(\mathbf{x})}{f_t(\mathbf{x})} < \frac{p_t}{p_b} \tag{B.2}$$

If we assume that the probability density functions of (B.1) are Gaussian with different means μ_b and μ_t, but the same variance σ, the allocation rule becomes: Allocate x_0 to π_b if

$$\frac{(\mu_t - \mu_b)}{\sigma}\, x_0 - \frac{1}{2}\, \frac{(\mu_t - \mu_b)(\mu_t + \mu_b)}{\sigma} \geq \ln\left(\frac{p_2}{p_1}\right) \tag{B.3}$$

Allocate x_0 to π_t otherwise. If the sample sizes of tissue and blood signal are equal, the prior possibilities are equal, and the allocation rule reduces to

$$x_0 \geq \frac{1}{2}\,(\mu_t + \mu_b) \tag{B.4}$$

This means that the allocation rule simply comes down to thresholding the classification functions when the parent populations are Gaussian. Further, if the means of the parent populations are known, the threshold level that minimizes TPM is also known.

Unfortunately, in Knowledge Based Imaging, Bandwidth Imaging and Second-Harmonic Imaging the parent populations are not known. However, if we assume they are similar to Gaussian, the above discussion indicates that a reasonable allocation rule is thresholding. This threshold is obviously not known and the optimal error rate can therefore not be calculated directly. In this manuscript the apparent error rate with the optimal threshold level is chosen, since the theoretical threshold is not available.

Appendix C

Discussion of the effect of reverberations from previous shots in Bandwidth Imaging

Let x_1 and x_2 be high-pass filtered signal samples obtained from equation (2.4) in part II. Let also s_1 and s_2 be highpass filtered signal that only comes from the range cell. If r is reverberations from the previous shot then a simple model for x_1 and x_2 is

$$\begin{aligned} x_1 &= s_1 + r \\ x_2 &= s_2 \end{aligned} \tag{C.1}$$

Furthermore $r(1)$ is the autocorrelation function with lag one

$$r(1) = x_1 \, \bar{x_2} \tag{C.2}$$

and $r(0)$ is the autocorrelation function without lag

$$r(0) = \frac{1}{2} \left(|x_1|^2 + |x_2|^2 \right) \tag{C.3}$$

By equation (2.3) in part II, Bandwidth Imaging is basically the normalized difference of $|x_1|$ and $|x_2|$. Obviously, $|x_1|$ is biased by the reverberation noise and in general the difference between $|x_1|$ and $|x_2|$ increases in this type of noise. This means that Bandwidth Imaging becomes darker in regions influenced by reverberations from previous shots.

Note that r comes from the whole acoustic focus of the reception beam and not only the range cell. Therefore, r is depth dependent. The rule of thumb is that radial resolution r_D of the acoustic focus of the reception beam is given by

$$r_D = 2 \, \frac{R^2}{a^2} \, \lambda \tag{C.4}$$

where the depth is R, a is aperture and λ is the wavelength. The acoustic focus of the reception beam has a radial resolution that increases with the square of the depth. Also larger reception beam focus increases the signal power of r. For the probe used in Table 2.1 in part II, the radial resolution is the same as the width of the range cell in the first 2.2 cm. The radial resolution is about 1 cm at 6 cm depth and at 10 cm it is about 4 cm. In Bandwidth Imaging, these artifacts are seen as shadowed regions close to the probe and further down as darkened lines. Dropouts in amplitude images are caused by energy absorptions, due to reverberations close to the probe. Artifact of reverberations from previous shots in Bandwidth Imaging can look similar to the dropout in amplitude images.

The influence of r is dependent on the attenuation factor at zero frequency in the Finite Impulse Response filter and the pulse repetition frequency. In Fig. C.1, Second-Harmonic Imaging is shown at six equally sparsed time steps in the cardiac cycle. In Fig. C.2, Bandwidth Imaging is shown where the pulse repetition frequency is set to 2750. The reverberation noise from previous shots is not visible. In Fig. C.3 the pulse repetition frequency is turned up to 4500, and this type of noise is seen as the septal wall is darkened. The septal wall is particularly vulnerable to this type of noise, since the smooth surface reflects much of the transmitted beam. In this case, sound is echoing back and forth between ventricle walls, and corrupting the signal in the next shots. It is therefore possible that pulse repetition frequency should be lower when imaging from the four-chamber view.

Notice also that the apex area is darker in Fig. C.3 than Fig. C.2. There can be two reasons for this. First, the clutter filter is dependent on pulse repetition frequency, and therefore signal shown in Fig. C.2 is filtered weaker than signal shown in Fig. C.3. This can to some degree be compensated for by adjusting AF. Second, reverberation noise from previous shots is also a possible reason. However, this is usually seen as flickering darker stripes, rather than dark smooth regions. The conclusion is that the pulse repetition frequency is limited upward by reverberations from previous shots and downward by transit time effect and clutter filter effect.

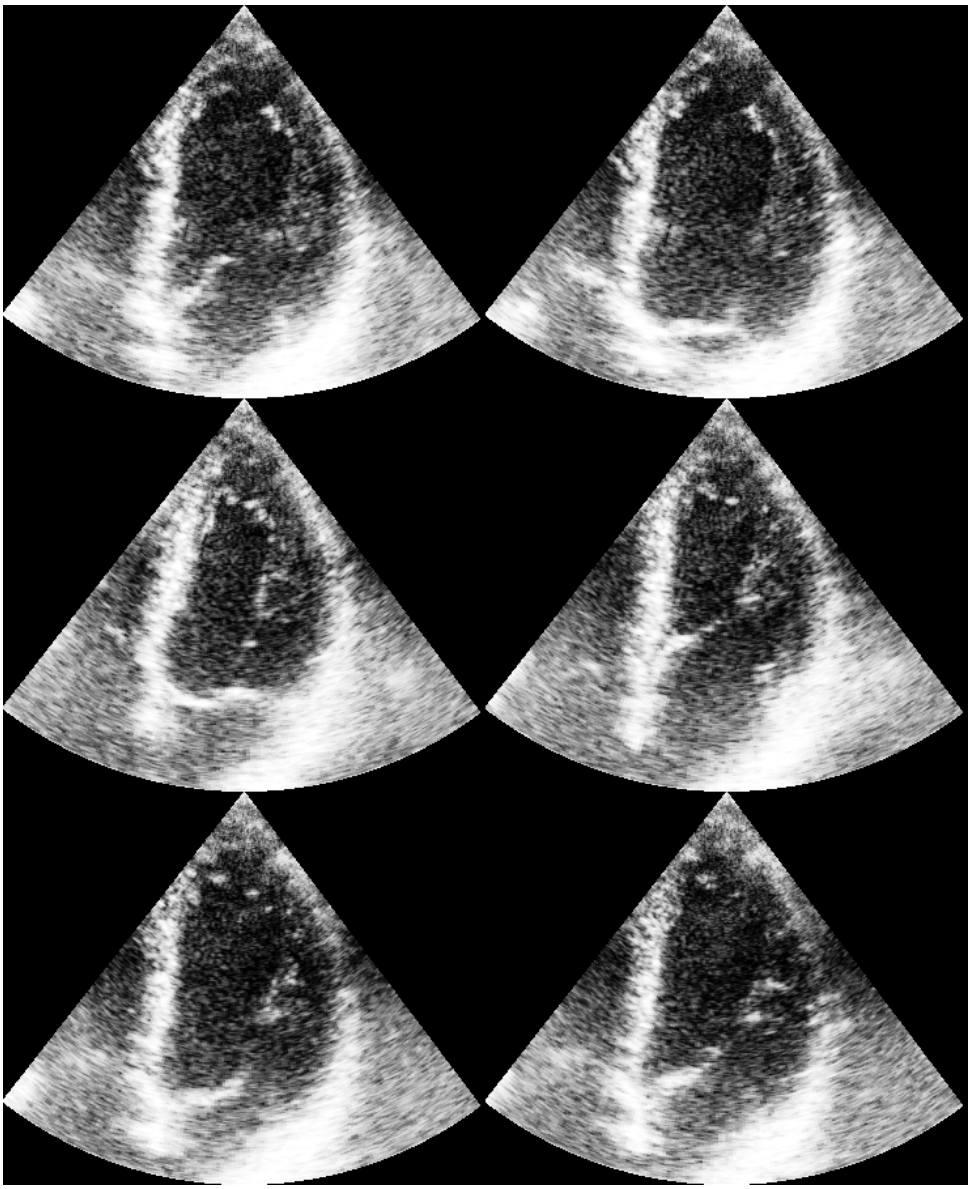

Figure C.1: Second-Harmonic Images is shown at six equally spaced time steps in the cardiac cycle. The images are added for comparison with C.2 and C.3.

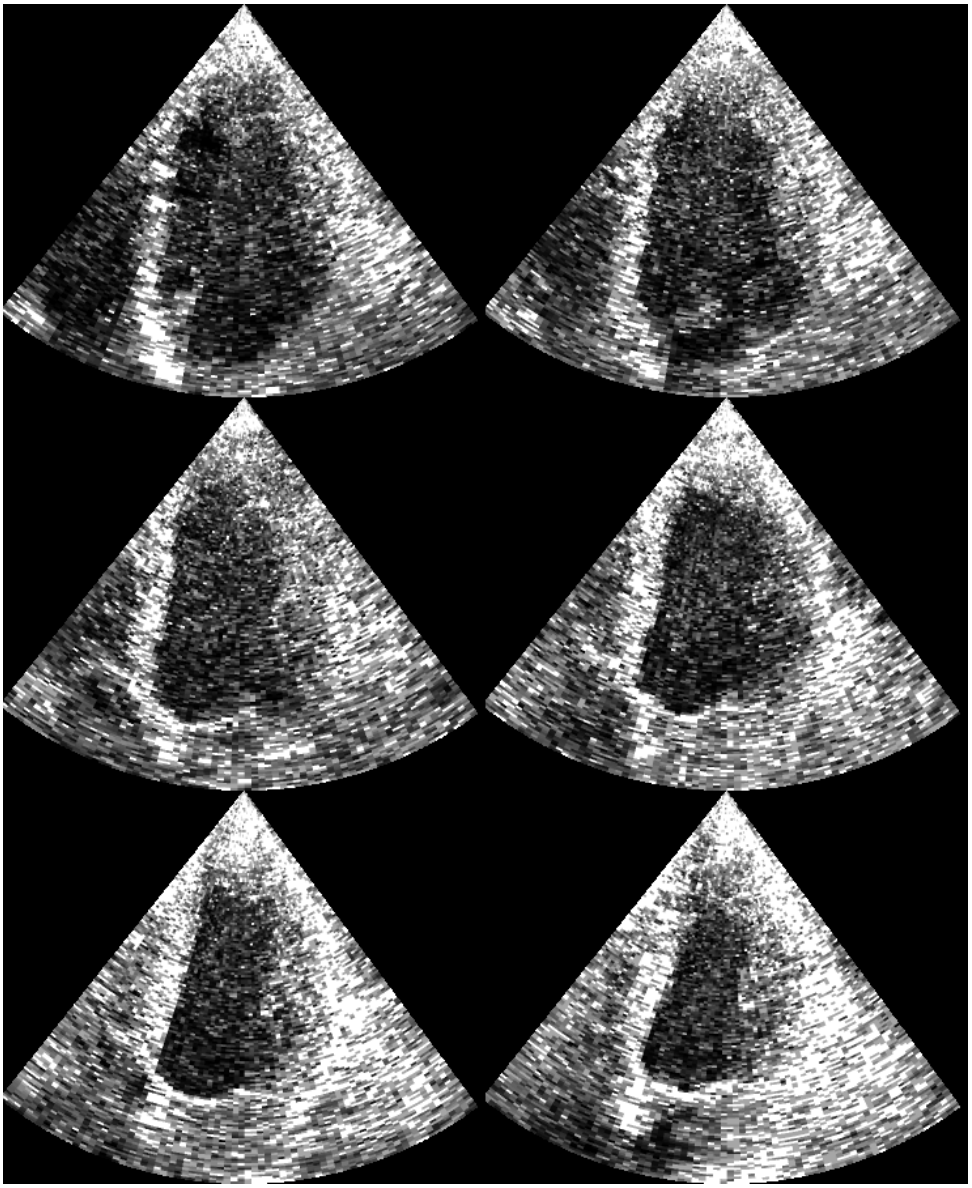

Figure C.2: Bandwidth Images is shown with a pulse repetition frequency of 2750. The reverberation noise from previous shots is not visible.

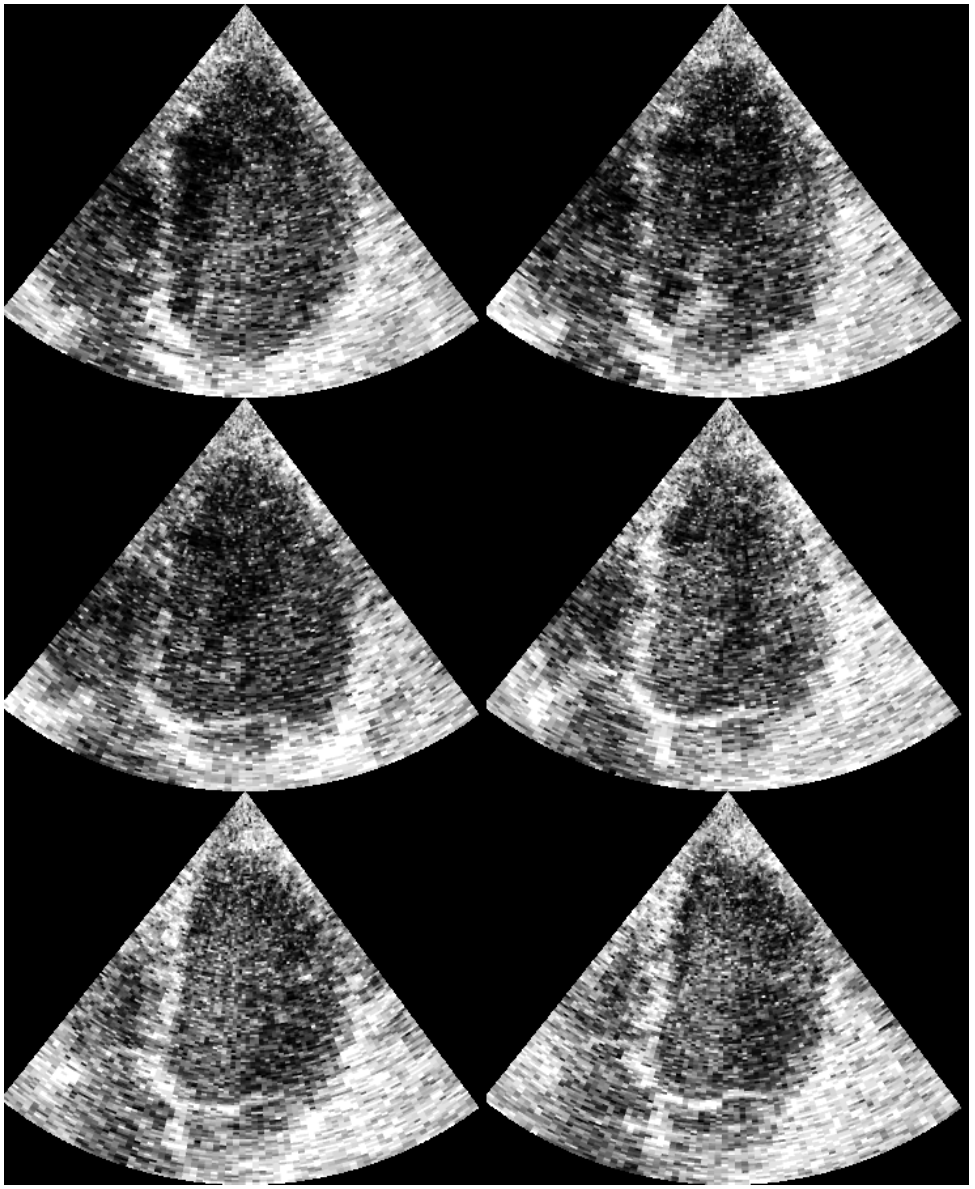

Figure C.3: Bandwidth Images with pulse repetition frequency of 4500. The reverberation noise from previous shots is seen as the septal wall is darkened. The septal wall is particularly vulnerable to this type of noise, since the smooth surface reflects much of the transmitted beam. Notice also that the apex area is darker in Fig. C.3 than in Fig. C.2. There can be two reasons for this. First, the clutter filter is dependent on pulse repetition frequency, and therefore the data in Fig. C.2 is filtered weaker than Fig. C.3. Second, reverberation noise from previous shots is also a possible reason.

Appendix D

Images of Knowledge Based Imaging, Bandwidth Imaging, Fundamental Imaging and Second-Harmonic Imaging

The next 18 pages contain four-chamber, two-chamber and long-axis views of six subjects in the study in chapter 3 in part II. On the left side of all the figures in this appendix, Second-Harmonic Imaging, Fundamental Imaging and Bandwidth Imaging are shown respectively. On the right side of all figures in this appendix, three variants of Knowledge Based Imaging are shown. Here the parameters of Knowledge Based Imaging are set in a similar manner as in Fig. 3.3 in part III. In KBI 2, blood and tissue signal are separated by their difference in power and the KBI 2 images are therefore similar to Fundamental Images. In KBI 3, blood and tissue signal are separated by their velocity and turbulence differences and the KBI 3 images is therefore similar to Bandwidth Images. KBI 1 are images with parameter settings, which are a combination of the settings of KBI 2 and KBI 3.

(a) Second-Harmonic Imaging

(b) KBI 1

(c) Fundamental Imaging

(d) KBI 2

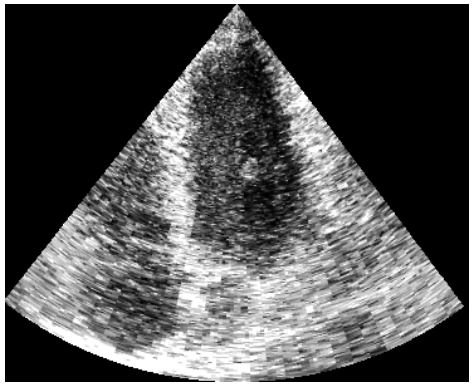

(e) Bandwidth Imaging

(f) KBI 3

Figure D.1: Four-chamber views of subject 1.

(a) Second-Harmonic Imaging

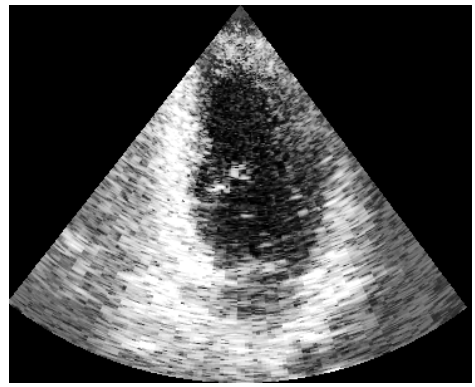

(b) KBI 1

(c) Fundamental Imaging

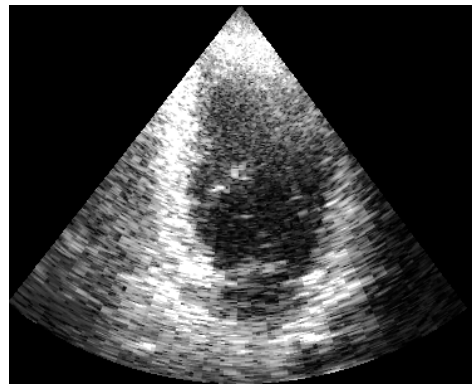

(d) KBI 2

(e) Bandwidth Imaging

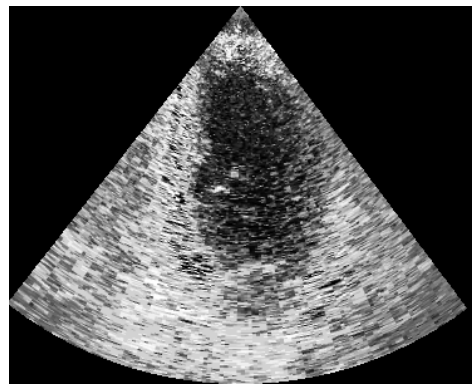

(f) KBI 3

Figure D.2: Two-chamber views of subject 1.

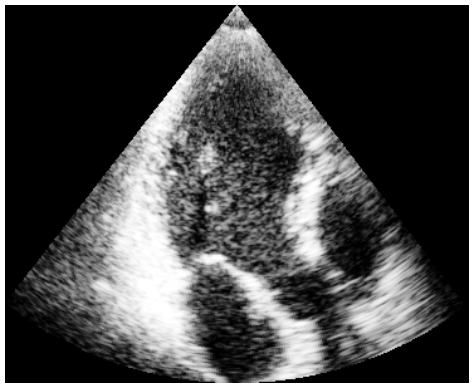

(a) Second-Harmonic Imaging

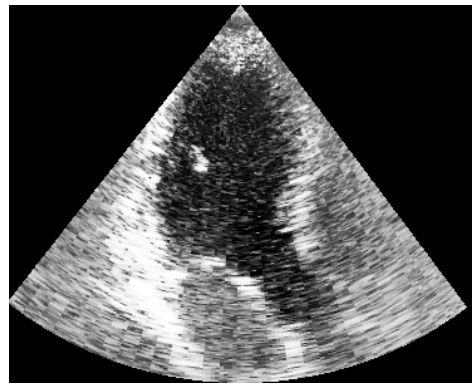

(b) KBI 1

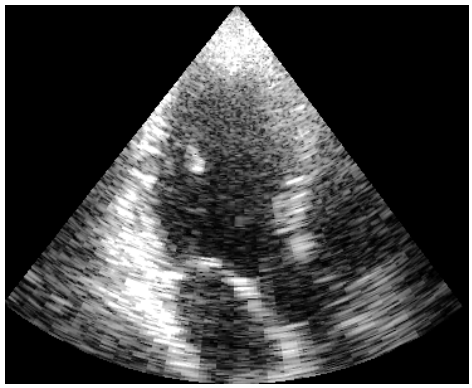

(c) Fundamental Imaging

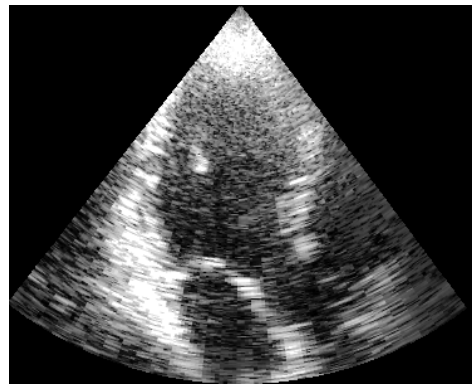

(d) KBI 2

(e) Bandwidth Imaging

(f) KBI 3

Figure D.3: Long-axis views of subject 1.

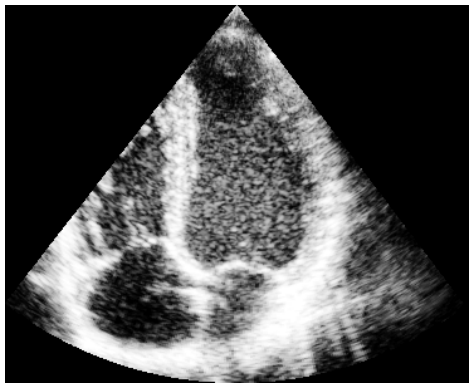

(a) Second-Harmonic Imaging

(b) KBI 1

(c) Fundamental Imaging

(d) KBI 2

(e) Bandwidth Imaging

(f) KBI 3

Figure D.4: Four-chamber views of subject 2.

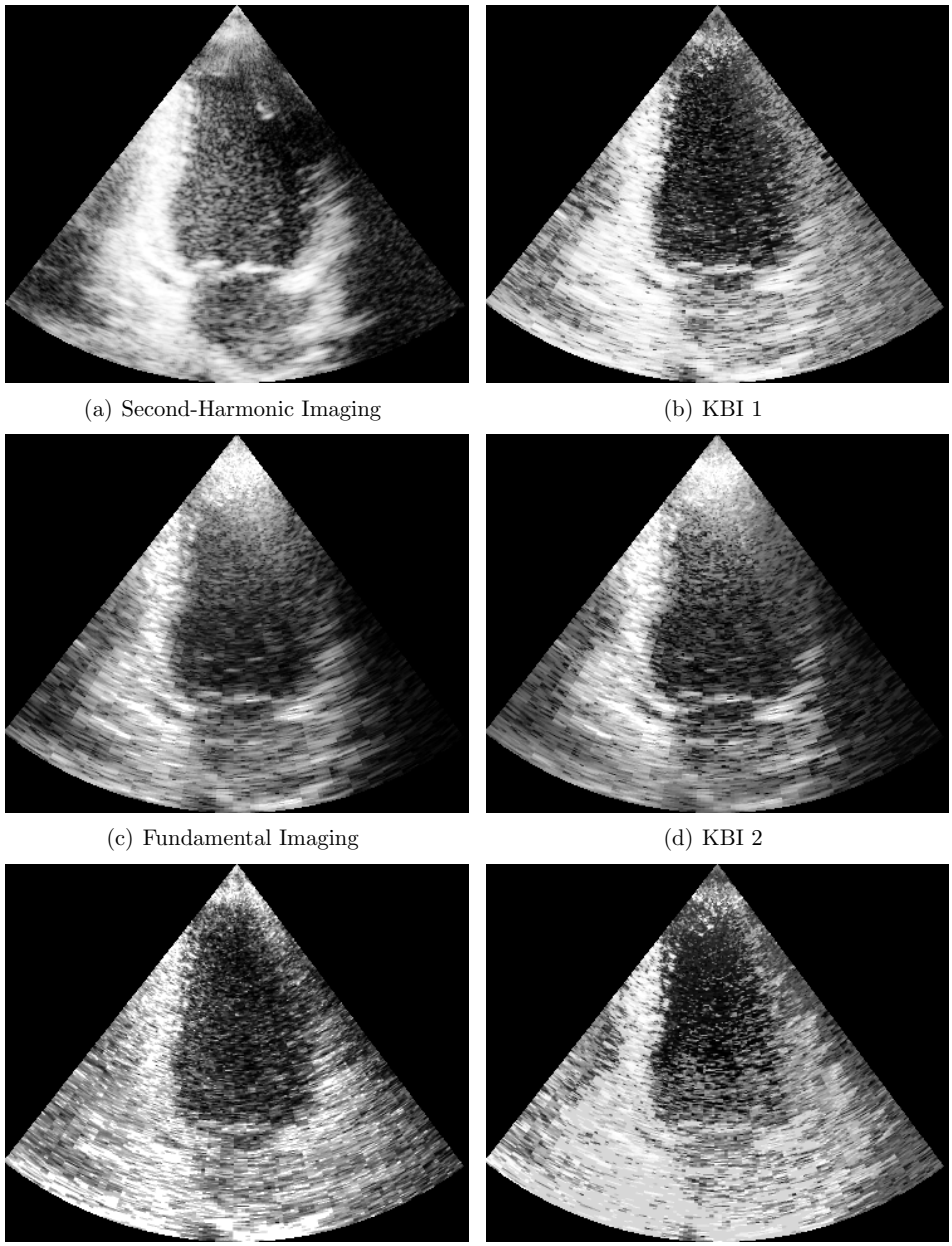

(a) Second-Harmonic Imaging

(b) KBI 1

(c) Fundamental Imaging

(d) KBI 2

(e) Bandwidth Imaging

(f) KBI 3

Figure D.5: Two-chamber views of subject 2.

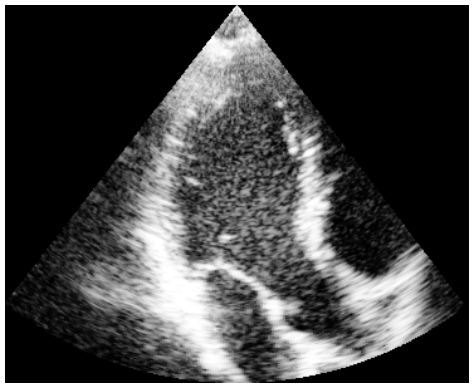

(a) Second-Harmonic Imaging

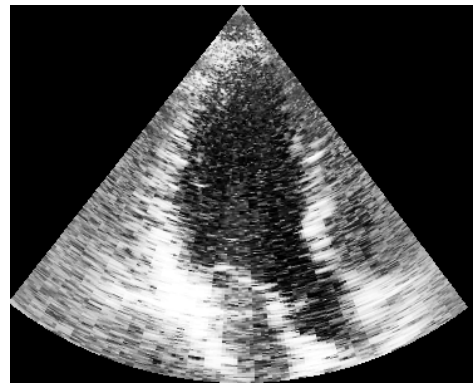

(b) KBI 1

(c) Fundamental Imaging

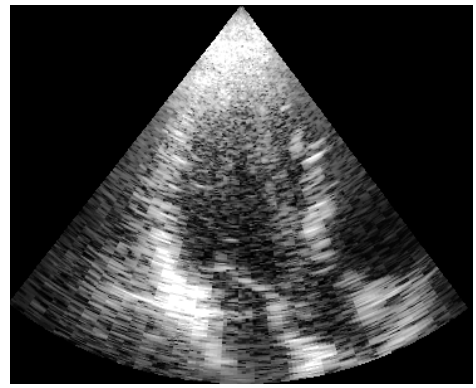

(d) KBI 2

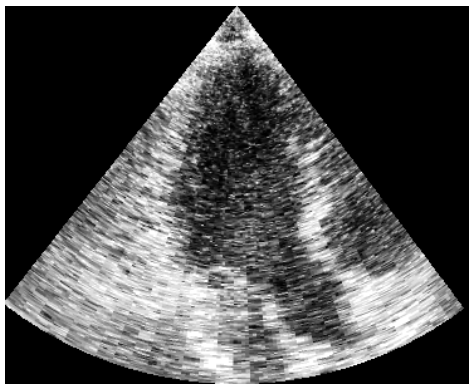

(e) Bandwidth Imaging

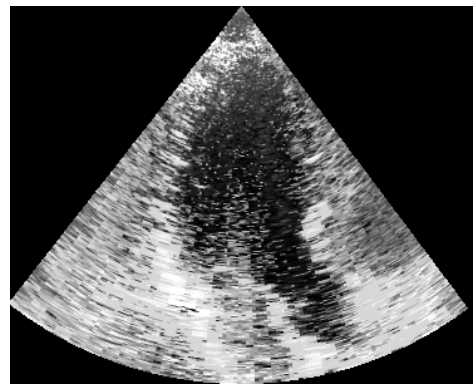

(f) KBI 3

Figure D.6: Long-axis views of subject 2.

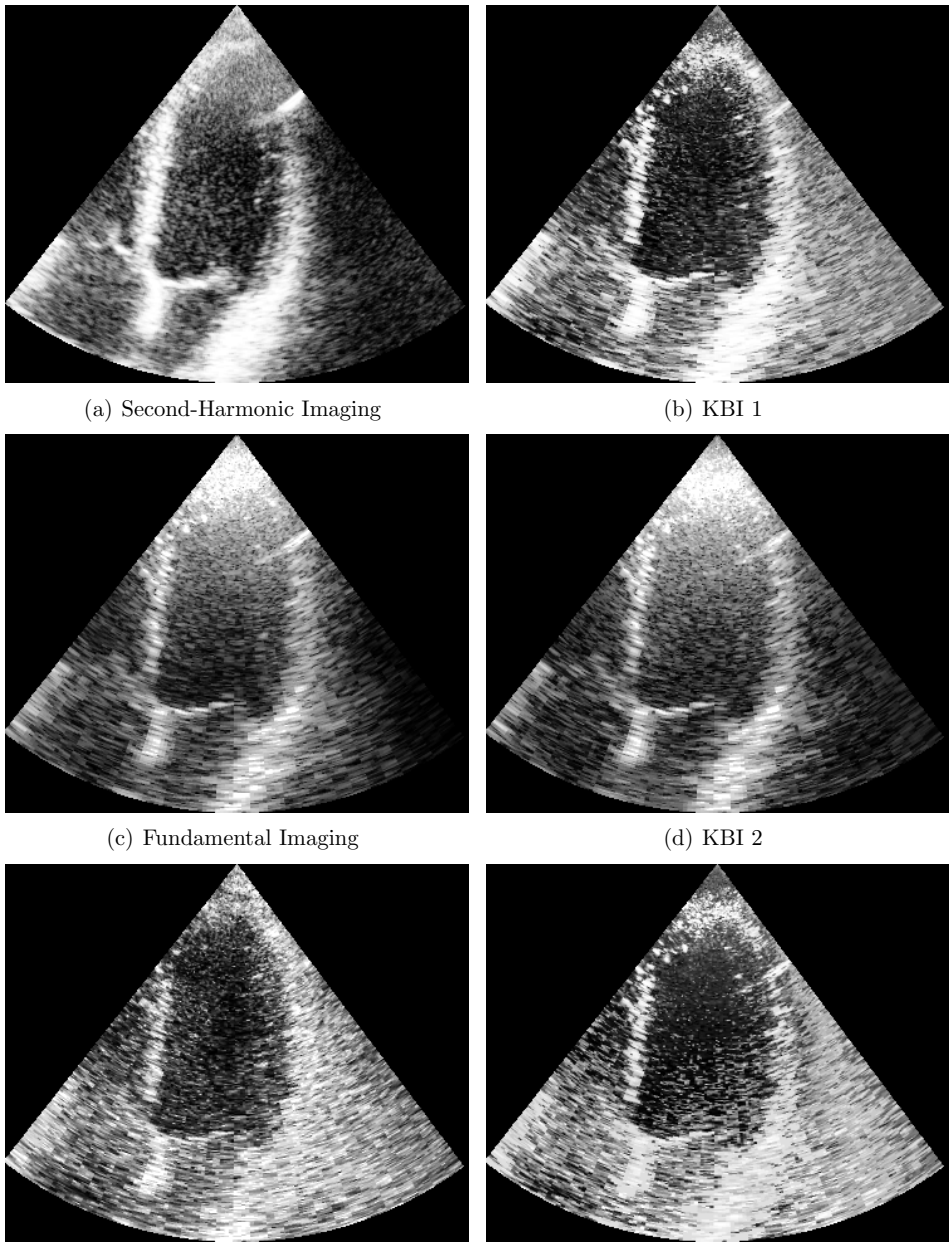

(a) Second-Harmonic Imaging

(b) KBI 1

(c) Fundamental Imaging

(d) KBI 2

(e) Bandwidth Imaging

(f) KBI 3

Figure D.7: Four-chamber views of subject 3.

(a) Second-Harmonic Imaging

(b) KBI 1

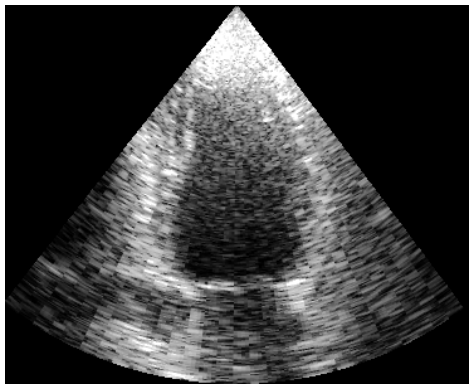

(c) Fundamental Imaging

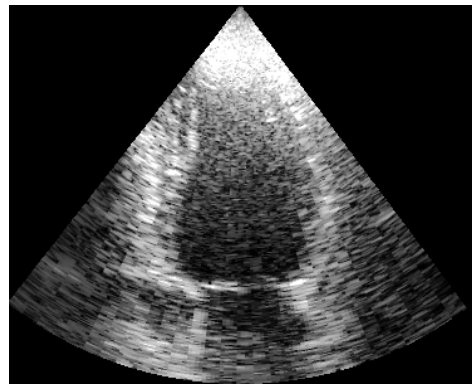

(d) KBI 2

(e) Bandwidth Imaging

(f) KBI 3

Figure D.8: Two-chamber views of subject 3.

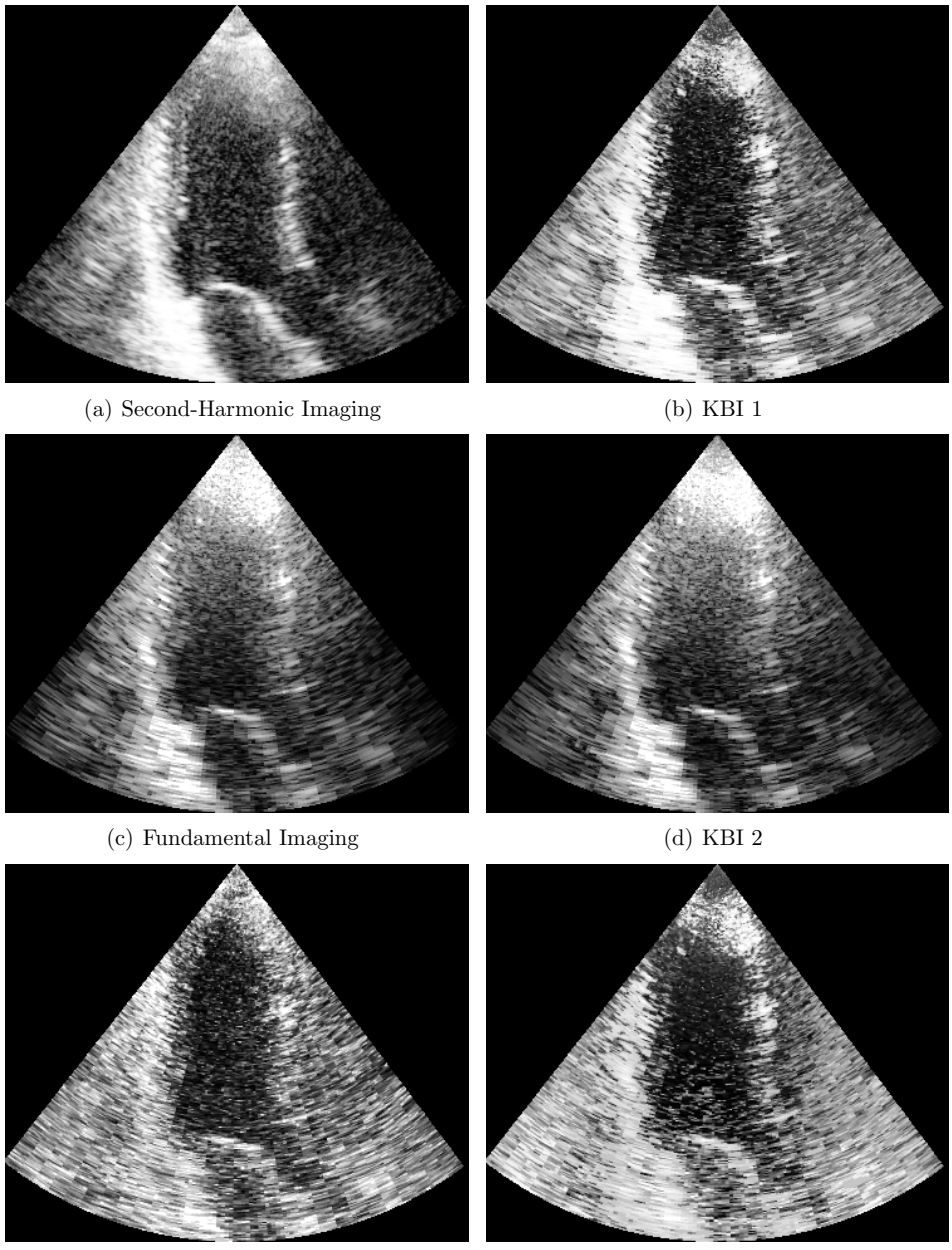

(a) Second-Harmonic Imaging

(b) KBI 1

(c) Fundamental Imaging

(d) KBI 2

(e) Bandwidth Imaging

(f) KBI 3

Figure D.9: Long-axis views of subject 3.

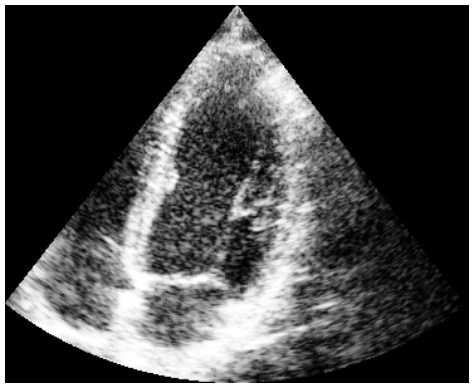

(a) Second-Harmonic Imaging

(b) KBI 1

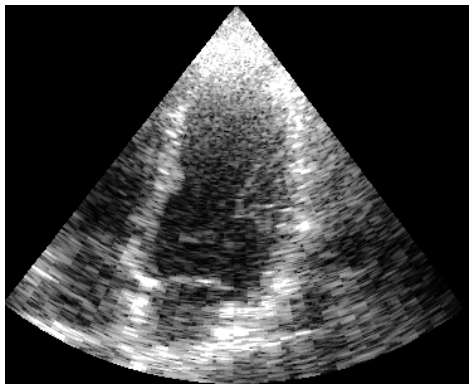

(c) Fundamental Imaging

(d) KBI 2

(e) Bandwidth Imaging

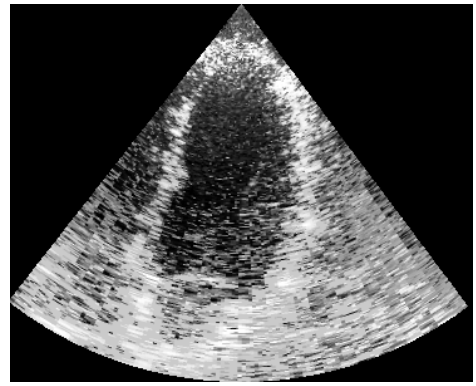

(f) KBI 3

Figure D.10: Four-chamber views of subject 4.

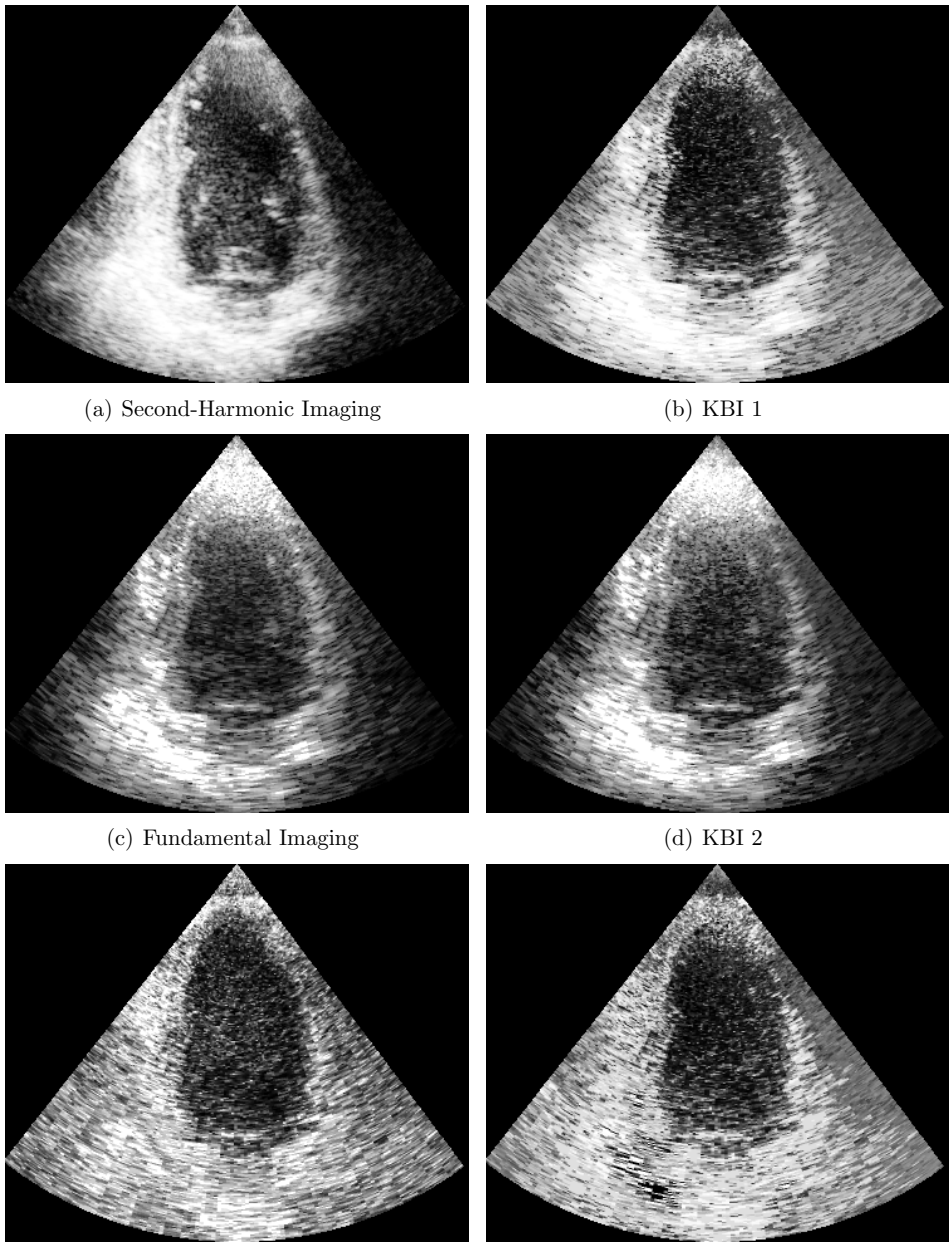

(a) Second-Harmonic Imaging

(b) KBI 1

(c) Fundamental Imaging

(d) KBI 2

(e) Bandwidth Imaging

(f) KBI 3

Figure D.11: Two-chamber views of subject 4.

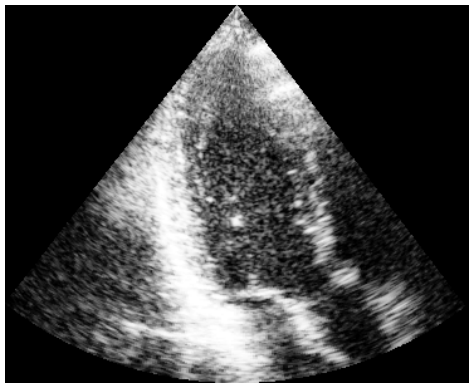

(a) Second-Harmonic Imaging

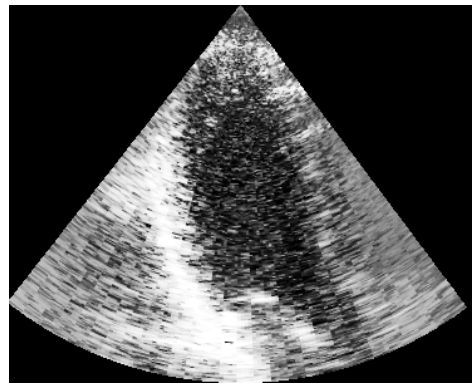

(b) KBI 1

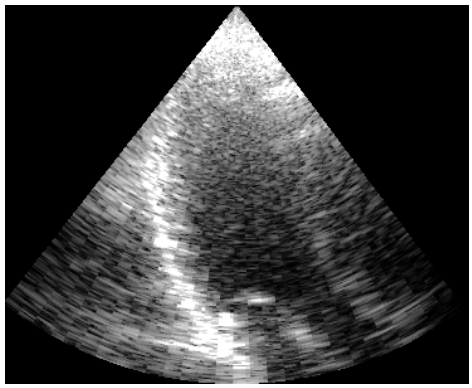

(c) Fundamental Imaging

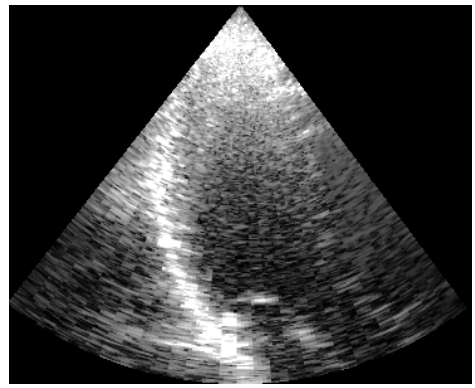

(d) KBI 2

(e) Bandwidth Imaging

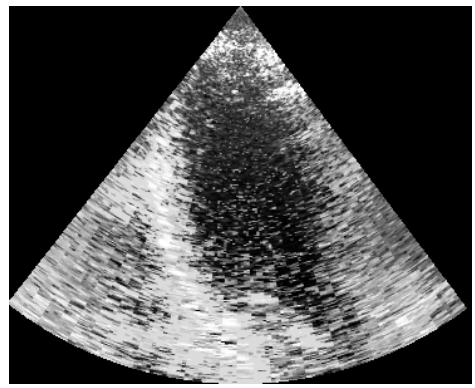

(f) KBI 3

Figure D.12: Long-axis views of subject 4.

(a) Second-Harmonic Imaging

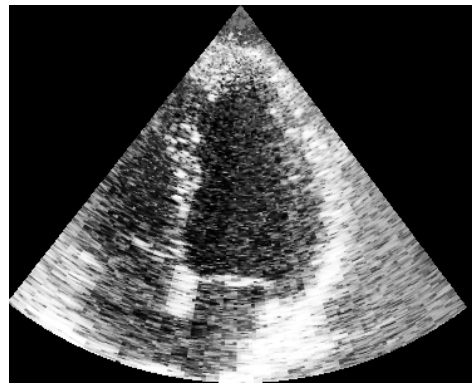

(b) KBI 1

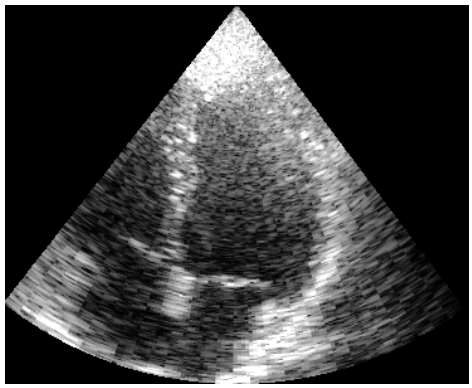

(c) Fundamental Imaging

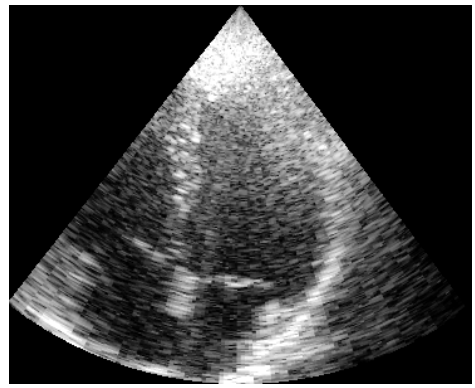

(d) KBI 2

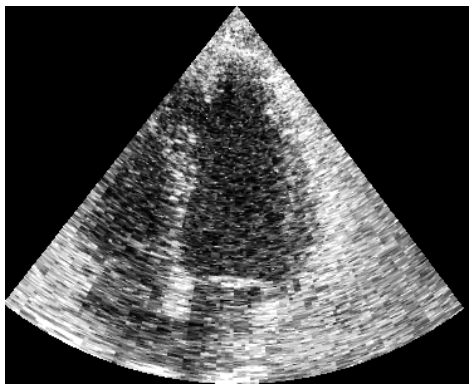

(e) Bandwidth Imaging

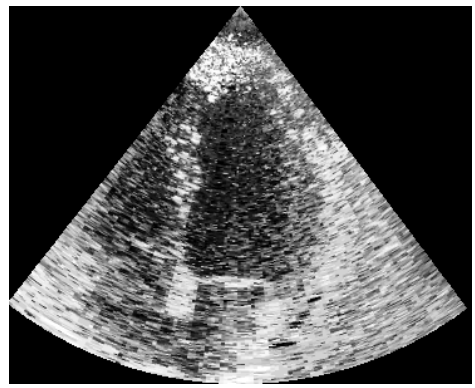

(f) KBI 3

Figure D.13: Four-chamber views of subject 5.

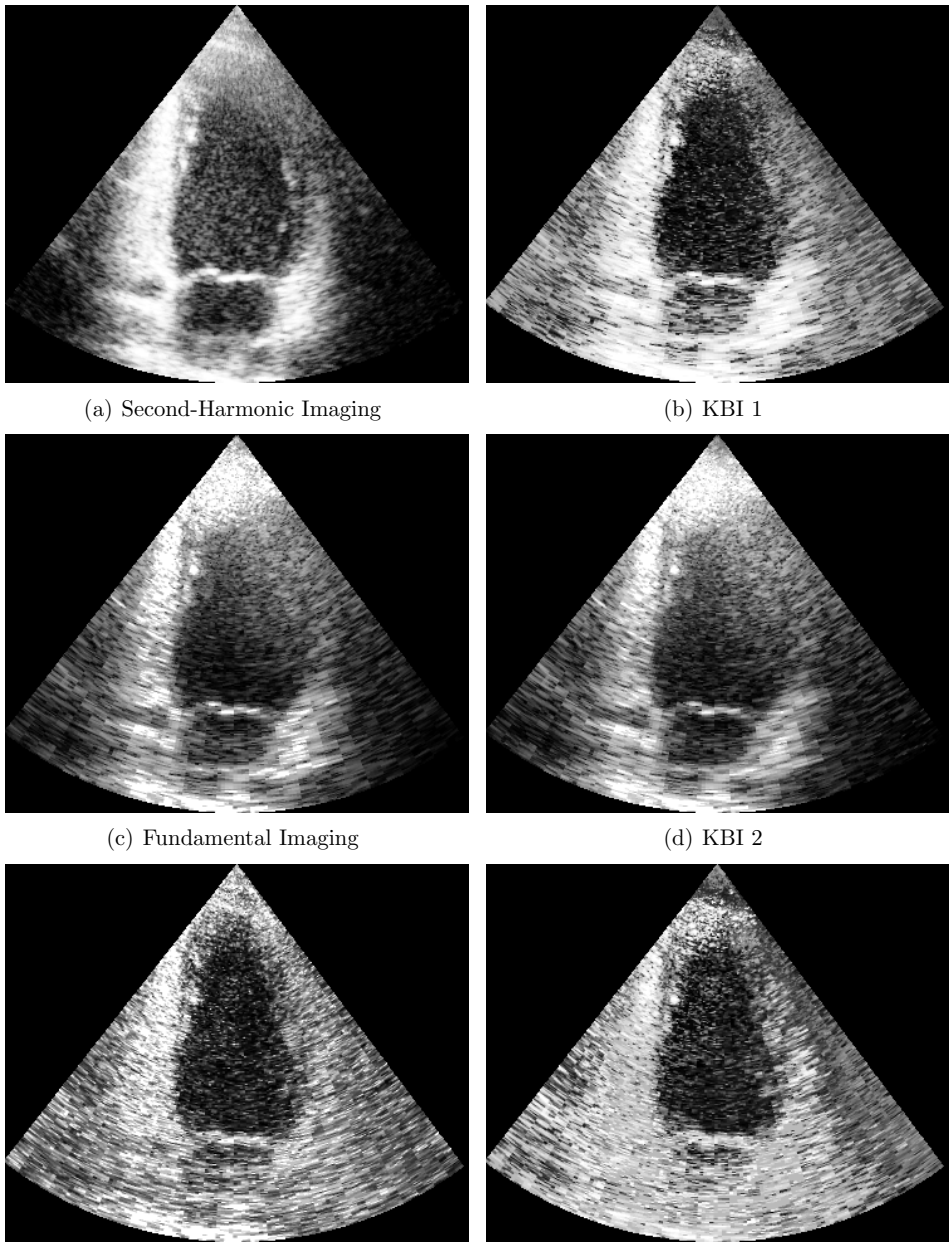

(a) Second-Harmonic Imaging (b) KBI 1

(c) Fundamental Imaging (d) KBI 2

(e) Bandwidth Imaging (f) KBI 3

Figure D.14: Two-chamber views of subject 5.

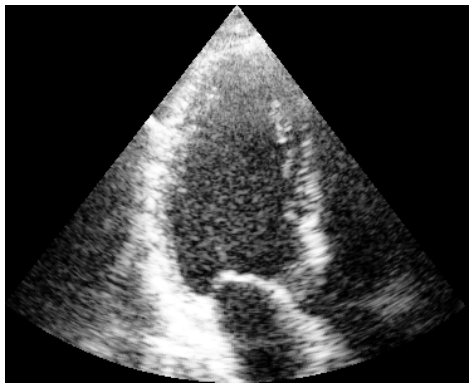

(a) Second-Harmonic Imaging

(b) KBI 1

(c) Fundamental Imaging

(d) KBI 2

(e) Bandwidth Imaging

(f) KBI 3

Figure D.15: Long-axis views of subject 5.

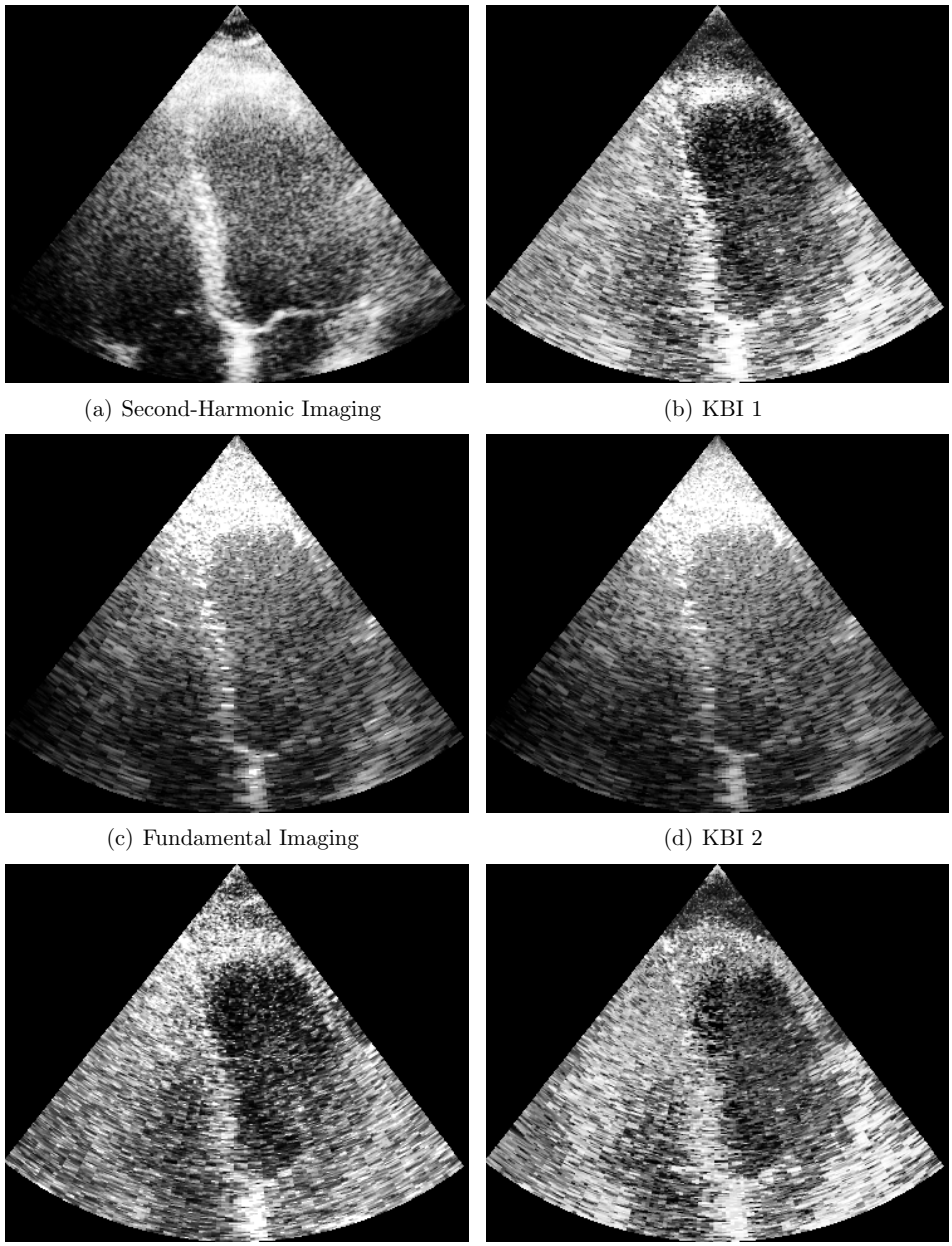

(a) Second-Harmonic Imaging

(b) KBI 1

(c) Fundamental Imaging

(d) KBI 2

(e) Bandwidth Imaging

(f) KBI 3

Figure D.16: Four-chamber views of subject 6.

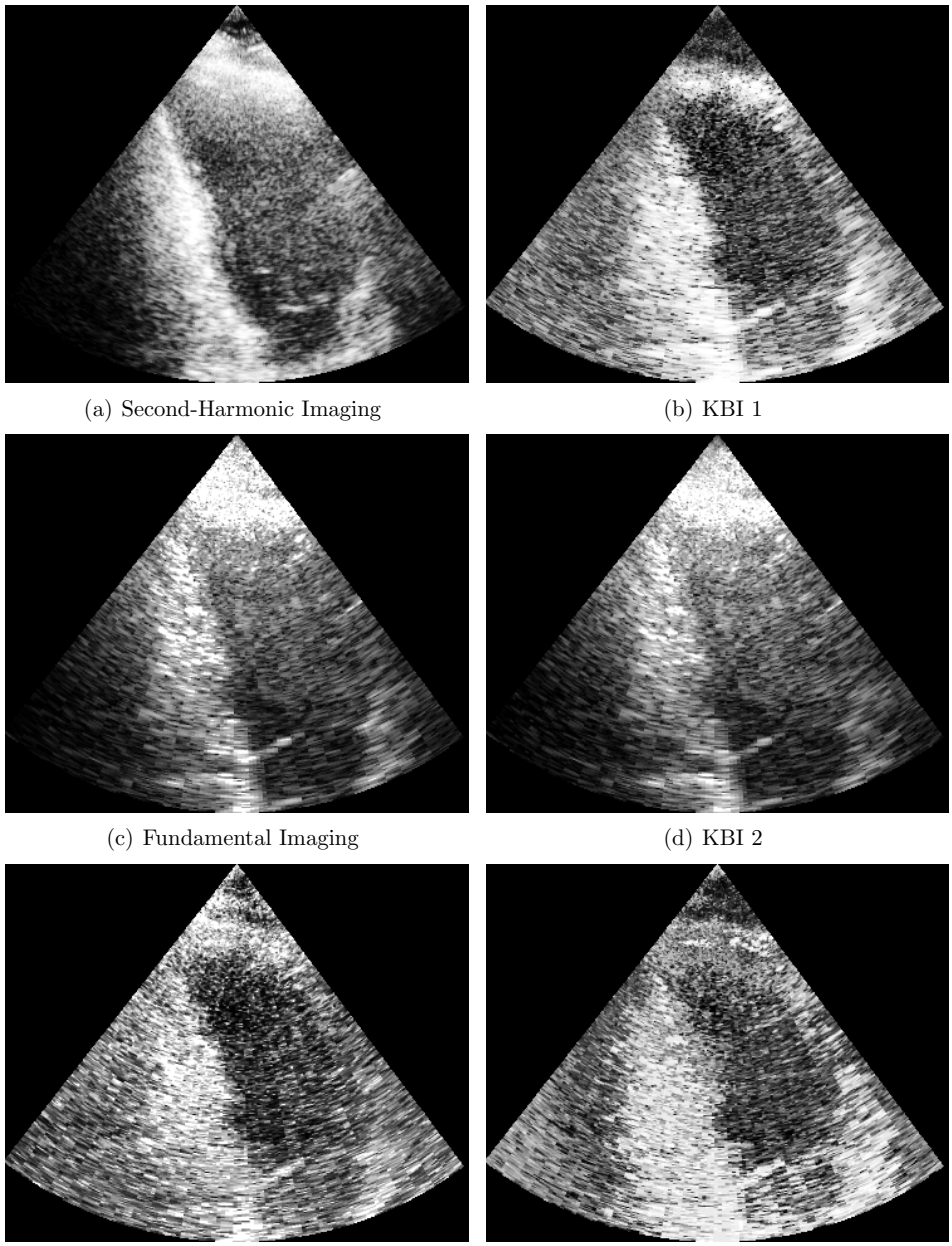

(a) Second-Harmonic Imaging (b) KBI 1

(c) Fundamental Imaging (d) KBI 2

(e) Bandwidth Imaging (f) KBI 3

Figure D.17: Two-chamber views of subject 6.

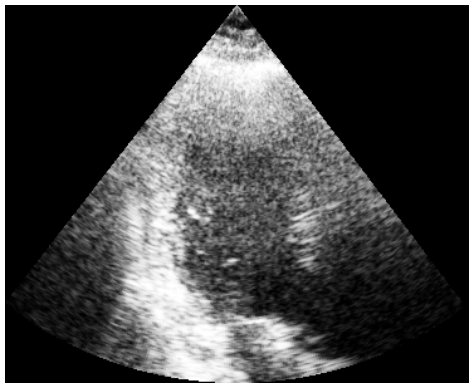

(a) Second-Harmonic Imaging

(b) KBI 1

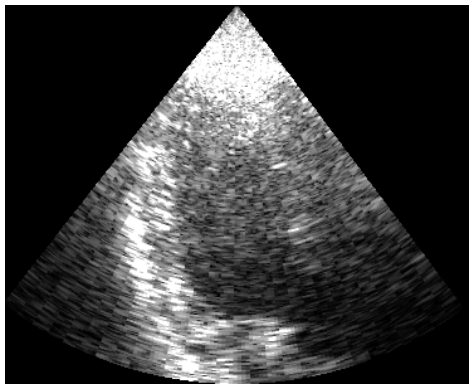

(c) Fundamental Imaging

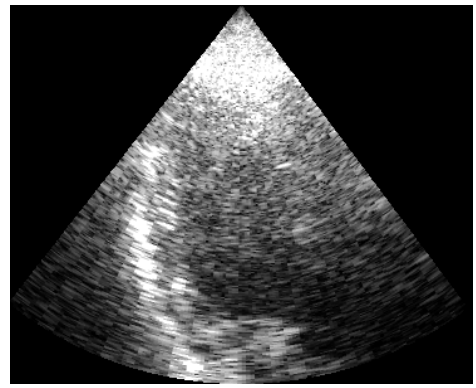

(d) KBI 2

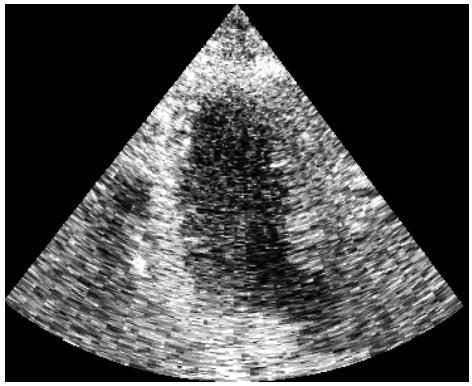

(e) Bandwidth Imaging

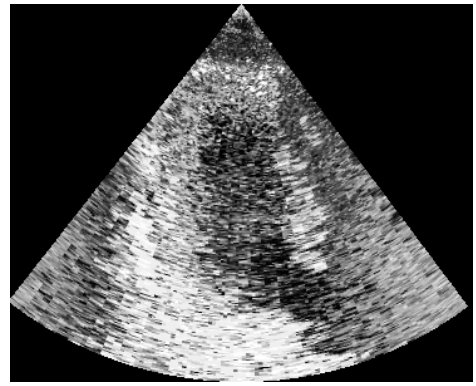

(f) KBI 3

Figure D.18: Long-axis views of subject 6.

Bibliography

[1] Cerqueira, M.D., Weissman, N.J., Dilsizian, V., A.K.Jacobs, S.Kaul, Laskey, W.K., D.J.Pennell, Rumberger, J.A., Ryan, T., Verani, M.S.: Standarized myocardial segmentation and nomencclature for tomographic imaging of the heart. Circulation (January 2002) 539 – 542

[2] Wild, J.J.: The use of ultrasonic pulses for the measurement of biological tissues and the detection of tissue density changes. Surgery **14(8)** (1950) 183–188

[3] Howry, D.H., Bliss, W.R.: Ultrasonic visualization of soft tissue structures of the body. J. Lab. Clin. Med. **40** (1952) 579–592

[4] Edler, I., Hertz, C.H.: The use of ultrasonic reflectoscope for the continuous recording of the movement of the heart wall. Kungl. Fysiogr. Sällskap. i Lund Förhandl. **24** (1954) 40–58

[5] Caidal, K., e. Kazzam, Lidberg, J., Andersen, G.N., Nordanstig, J., Dahlqvist, S.R., Waldenstrom, A., Wikh, R.: New concept in echocardiography: harmonic imaging of tissue without use of contrast agent. Lancet **352(9136)** (1998) 1264–1270

[6] Spencer, K.T., Bednarz, J., Rafter, P.G., Korcarz, C., Lang, R.M.: Use of harmonic imaging without echocardiographic contrast to improve two dimensional image quality. American Journal of Cardiology **82(6)** (1998) 794–799

[7] Satomura, S.: Ultrasonic doppler method for the inspection of cardiac function. J. Acoust. Soc. Am. **29** (1957) 1181–1185

[8] Jensen, J.A.: 6.5 and 7.5. In: Estimation of Blood Velocities Using Ultrasound. Cambridge University Press, New York, NY (1996)

[9] Angelsen, B.A.: 7.4 ,9,3 , 10.4. In: Ultrasound Imaging Wawes, Signals and Signal Processing. Emantec, Trondheim, Norway (2000)

[10] Baker, D.W., Watkins, D.W.: A phase coherent pulse doppler system for cardiovascular measurement. In: 20th Ann. Conf. on Eng. in Med. and Biol. Volume 27. (1967)

[11] Namekawa, K., Kasai, C., Tsukamoto, M., a. Koyano: Real-time blood flow imaging system utilizing autocorrelation technique. In: R. Lerski and P. Morley, editors, Ultrasound'82, Pergamon Press (1982) 203–208

[12] Kasai, C., Namekawa, K., Koyano, A., Omoto, R.: Real-time two-dimensional blood flow imaging using an autocorrelation routine. IEEE Transactions on Sonics Ultrason **32(3)** (Mar 1985) 458–464

[13] Ahn, Y.B., s. B. Park: Estimation of mean frequency and variance of ultrasonic doppler signal by using second- order autoregressive model. IEEE Transactions on Ultrasonics, Ferroelectriscs. and Frequency Control **38(3)** (May 1991) 172–182

[14] Bonnefous, O., Pesqué, P.: time domain formulation of pulse-doppler ultrasound and blood velocity estimation by cross correlation. Ultrasound imag. **8** (1986) 73–85

[15] Bohs, L.N., Freemel, B.H., McDermott, B.A., Trahey, G.E.: A real time system for quantifiying and displaying two-dimensional velocities using ultrasound. Ultrasound Med. Biol. **19** (1993) 715–761

[16] Ferrara, K.W., Algazi, V.R.: A new wideband spread targetmaximum likelihood estimator for blood velocity estimation -pat 1:theory. IEEE Transactions on Ultrasonics, Ferroelectriscs. and Frequency Control **38(1)** (Jan 1991) 1–16

[17] Kristoffersen, K.: Optimal receiver filtering in pulsed doppler ultrasound blood velocity measurements. IEEE Transactions on Ultrasonics, Ferroelectriscs. and Frequency Control **33(1)** (Jan 1986) 51–58

[18] Torp, H.: Clutter rejection filters in color flow imaging a theoretical approach. IEEE Transactions on Ultrasonics, Ferroelectriscs. and Frequency Control **44** (mar 1997) 417–424

[19] Bjærum, S., Torp, H., Kristoffersen, K.: Clutter filter design for color flow imaging. IEEE Transactions on Ultrasonics, Ferroelectriscs. and Frequency Control **49** (feb 2002) 204–217

[20] Otto, C.M., ed.: The practice of clinical echocardiography, second edition. W. D. Saunders Company, Philadelphia, Pennsylvania (2002)

[21] Yuille, A.L., Cohen, D.S., Hallinan, P.: Feature extraction from faces using deformable templates. Int. J. Comput. Vision **8** (1992) 99–112

[22] Lipton, P., Yuille, A.L., O'Keeffe, D., Cavanough, J., Taaffe, J., Rosenthal, D.: Deformable templates from medical images. In: First European Conference on Computer Vision (O. Faugeras ed.) Lecture Notes in Computer Science, Berlin / New York (1990)

[23] Beinglass, A., Volfson, H.J.: Articulated object recognition, or: How to generalise the generalised hough transform. In: IEEE Computer Society Conference on Computer Vision and Pattern Recognition, Berlin / New York (1991) 461–466

[24] Malassiotis, S., Strintzis, M.G.: Tracking the left ventricle in echocardiographic images by learning heart dynamics. IEEE Transactions on Medical Imaging **18(3)** (mar 1999) 280–290

[25] Kass, M., Witkin, A., Terzopoulos, D.: Snakes: Active contour models. In: First International Conference on Computer Vision. (1987) 259–268

[26] Olstad, B.: Active contours with grammatical descriptions. In: 6th International conference on Image analyses and Processing, Como Italy (sep 1991)

[27] Mikic, I., Krucinski, S., Thomas, J.D.: Segmentation and tracking in echocardiographic sequences; active contour guided by optical flow estimates. IEEE Transactions on Medical Imaging **17(2)** (apr 1998) 274–284

[28] Giachetti, A.: On-line analyses of echocardiographic image sequences. Med. Image anal. **2(3)** (sep 1998) 261–284

[29] Bosch, J.G., Savalle, L.H., van Burken, G., Reiber, J.H.: Evaluation of semiautomatic contour detection approach to sequences of short axes two-dimensional echocardiographic images. J. Am: Soc. Echocardiogr **8(6)** (nov 1995) 810–821

[30] Sonca, M., Zhang, X., Siebes, M., Bissing, M.S., DeJong, S.C., Collins, S.M., McKay, C.: Segmentation of intravascular ultrasound images: A knowledge-based approach. IEEE Transactions on Medical Imaging **14(4)** (des 1995)

[31] Bosch, H.G., Mitchell, S.C., Lelieveldt, B.P.F., Nijland, F., Kamp, O., Sonka, M., Reiber, J.H.C.: Active appearance-motion models for fully automated endocardial contour detection in time sequences of echocardiograms. International Congress Series **1230** (jun 2001) 941–947

[32] McEachenand-2nd, M.C., Duncan, J.S.: Shape-based tracking of left ventricular wall motion. IEEE Transactions on Medical Imaging **16(3)** (jun 1997) 270–283

[33] Jacob, G., Noble, A., Mulet-Parada, M., Blake, A.: Evaluation of a robust contour tracker in echocardiographic sequences. Med. Image Anal **3(1)** (1999) 63–75

[34] Cootes, T.F., Taylor, C.J., Cooper, T.H., Graham, J.: Active shape models - their training and application. Computer Vision and Image Understanding **61(1)** (jan 1995) 38–59

[35] Dove, E.I., Phillip, K., Gotteiner, N.L., Vonesh, M.J., Ramberger, J.A., Reed, J.E., Standford, W., McPherson, D.D., Chandran, K.B.: A method for automatic edge detection and volume computation of the left ventricle from ultrafast computed tomographic images. Investigative Radiology **29(11)** (nov 1994) 945–954

[36] Storaa, C., Grandell, A., Gustavi, T., Torp, A.H., Lind, B., Brodin, L.Å.: Simple algorithms for the automatic detection of predefined echocardiographic localisations. In: International Federation for Medical and Biological Engineering (IFMBE) Proceedings. The 12th Nordic Baltic Conference on Biomedical Engineering and Medical Physics, Berlin / New York (feb 2002) 106–107

[37] Malm, S., Frigstad, S., Sagberg, E., andT. Skjærpe, H.L.: Accurate and reproducible measurement of left ventricular volume and ejection fraction by contrast echocardiography. Journal of the American College of Cardiology **44** (Sept 2004) 1030–1035

[38] Johnson, R.A., Wichern, D.W.: Applied Multivariate Statistical Analysis. Prentice-Hall Inc (2002)

[39] Heimdal, A., Torp, H.: Ultrasound doppler measurements of low velocity blood flow limitations due to clutter signals form vibrating muscles. IEEE Transactions on Ultrasonics, Ferroelectriscs. and Frequency Control **44** (jul 1997) 873–881

[40] Torp, H., Kristoffersen, K., Angelsen, B.A.J.: Autocorrelation techniques in color flow imaging: Signal model and statistical properties of the autocorrelation estimates. IEEE Transactions on Ultrasonics, Ferroelectriscs. and Frequency Control (1994)

[41] Heimdal, A., Torp, H.: Detecting small blood vessels in colorflow ultrasound imaging> a statistical approach. IEEE Transactions on Ultrasonics, Ferroelectriscs. and Frequency Control (1999)

[42] Angelsen, B.A.J.: A theoretical study of the scattering of ultrasound from blood. IEEE Trans. Biomed. Eng. **27(2)** (Feb 1980) 61–67

[43] Schoephoerster, C., Chandran, K.B.: Velocity and turbulence measurements past mitral valve prostheses in a model left ventricle. Journal of Biomechanics **24**(7) (1991) 549–562

[44] Trees, H.L.V.: Detection, Estimation, and Modulation Theory. Volume 1. John Wiley and Sons, Inc. (1968)

[45] An, L.T.H., Tao, P.D.: A branch and bound method via d.c. optimization algorithms and ellipsoidal technique for box constrained nonconvex quadratic problems. Journal of Global Optimization **13**(2) (September 1998) 171–206

List of Symbols

Abbreviations

BEDS	Best Bandwidth Imaging end diastole segments, page 27
BESS	Best Bandwidth Imaging end systole segments, page 27
GM	Global measure, page 26
HEDS	Best Second-Harmonic Imaging end diastole segments, page 27
HESS	Best Second-Harmonic Imaging end systole segments, page 27
HUM	Histogram uniformity measure, page 26
LM	Local measure, page 26
TGC	Time gain compensator, page 4
TPM	Total probability for misclassification, page 73
UEDS	Undecidable end diastole segments, page 27
UESS	Undecidable end systole segments, page 27

Greek letters

$\alpha(m)$	Approximation of $\hat{\alpha}(m)$, page 53
$\hat{\alpha}(m)$	Turbulence parameter, page 53
β	Transit time parameter, page 76
$\beta(m)$	Transit time parameter (laminar), page 53
$\hat{\beta}(m)$	Transit time parameter (turbulence), page 53
λ	Wavelength, page 76
μ_b	Mean of classification estimator in blood, page 73

μ_t Mean of classification estimator in tissue, page 73

ϕ Phase shift of Doppler signal, page 76

Π_b Set of samples in all blood segments, page 25

Π_t Set of samples in all tissue segments, page 25

σ Variance of classification estimator, page 73

σ_1 Standard deviation of displacement or velocity in radial direction, page 52

σ_2 Standard deviation of displacement or velocity in lateral direction, page 52

σ_3 Standard deviation of displacement or velocity in elevation direction, page 52

σ_c^2 Power of clutter noise, page 53

σ_n^2 Power of white noise, page 53

σ_{v_b} Standard deviation of blood velocity profile inside one range cell, page 53

τ Time increment, page 51

Θ_1 Lateral resolution corresponding to -3.25 dB opening angle, page 52

Θ_2 Elevation resolution corresponding to -3.25 dB opening angle, page 52

$\boldsymbol{\Upsilon}(\mathbf{r}, t)$ Variance per unit volume in numbers of blood cells inside ΔV, page 51

ΔV Small volume element, page 51

ζ_1 Mean displacement or velocity in radial direction, page 52

ζ_2 Mean displacement or velocity in lateral direction, page 52

ζ_3 Mean displacement or velocity in elevation direction, page 52

$\zeta(\mathbf{r}, t, \tau)$ Displacement of fluid element, page 51

Roman letters

a Aperture, page 76

C_b Covariance matrix for blood signal, page 53

C_t Covariance matrix for tissue signal, page 53

C_{bi} Cost of a sample in Π_b, page 25

c_{bi}	Cost of a sample in π_b, page 25
C_{bMTi}	Cost of a misclassification of Π_b, where the threshold is T, page 25
c_{bMTi}	Cost of a misclassification in π_b, where the threshold is T, page 25
C_{ti}	Cost of a sample in Π_t, page 25
c_{ti}	Cost of a sample in π_t, page 25
C_{tMTi}	Cost of a misclassification of Π_t, where the threshold is T, page 25
c_{tMTi}	Cost of a misclassification in π_t, where the threshold is T, page 25
f_0	Center frequency of probe, page 4
$f_b(\mathbf{x})$	Probability density function associated with π_b, page 73
f_d	Doppler mean frequency shift, page 4
$f_t(\mathbf{x})$	Probability density function associated with π_t, page 73
$G(\omega)$	Power spectrum of Doppler signal, page 69
k	Wave number, page 52
L	Pulse length, page 52
$\mathbf{L_b}$	Lower triangular matrix obtained by Cholesky factorization of $\mathbf{C_b}$, page 58
$\mathbf{L_t}$	Lower triangular matrix obtained by Cholesky factorization of $\mathbf{C_t}$, page 58
N	Number of samples in simulation, page 58
N	Packet size, page 70
n_b	Sample size in π_b, page 24
N_b	Number of samples in Π_b, page 25
$n_b(\mathbf{r}, t)$	Fluctuation of blood cell concentration, page 51
n_t	Sample size in π_t, page 24
N_t	Number of samples in Π_t, page 25
n_{bMT}	Number of misclassifications of π_b given threshold T, page 25
N_{bMT}	Number of misclassifications of Π_b at threshold T, page 25
n_{bM}	Number of misclassifications in π_b, page 24

n_{tMT}	Number of misclassifications of π_t given threshold T, page 25
N_{tMT}	Number of misclassifications of Π_t at threshold T, page 25
n_{tM}	Number of misclassifications in π_t, page 24
ω_1	Doppler mean frequency shift, page 69
$\hat{P}_b$	Maximum of conditional probabilities for signal from blood, page 53
$\hat{P}_t$	Maximum of conditional probabilities for signal from tissue, page 53
B	Bandwidth of Doppler signal, page 19
P	Power of Doppler signal, page 69
p_b	Prior probability of π_b, page 73
P_b	Probability density functions for signal from blood, page 53
p_t	Prior probability of π_t, page 73
P_t	Probability density functions for signal from tissue, page 53
P_{σ_b}	Probability density function for σ_b, page 54
P_{σ_c}	Probability density function for σ_c, page 54
P_{σ_n}	Probability density function for σ_n, page 54
P_{σ_t}	Probability density function for σ_t, page 54
$P_{\sigma_{v_b}}$	Probability density function for σ_{v_b}, page 54
P_{v_b}	Probability density function for v_b, page 54
AF	Attenuation factor at zero frequency, page 19
r	Reverberations from previous shot, page 75
R	Depth in image, page 76
$r(m)$	Autocorrelation function with temporal lag, page 19
R_b	Classification region associated with π_b, page 73
R_b	Autocorrelation estimates of blood signal, page 53
r_D	Acoustic focus of the reception beam, page 76
R_t	Classification region associated with π_t, page 73

R_t	Autocorrelation estimates of tissue signal, page 53
$\mathbf{r}$	Position in blood cell, page 51
c	Speed of sound, page 4
s_1	Highpass filtered signal from sample one, page 75
s_2	Highpass filtered signal from sample two, page 75
T	Threshold level of classification criteria, page 25
t	Time, page 51
T	Repetition time, page 52
v_b	Radial velocity component in blood, page 53
v_e	Velocity component in elevation direction, page 52
v_l	Velocity component in lateral direction, page 52
v_r	Velocity component in radial direction, page 52
v_t	Radial velocity component in tissue, page 53
v_z	Velocity component in beam direction, page 4
x_1	Highpass filtered signal sample one, page 19
x_2	Highpass filtered signal sample two, page 19
$\mathbf{x_1}$	Normalized complex Gaussian signal created by a random generator, page 58
$\mathbf{x_2}$	Normalized complex Gaussian signal created by a random generator, page 58
$Z(\omega)$	Fourier transform of signal, page 70
z_n	Signal samples, page 70
$\mathbf{z_b}$	Simulated signal samples of blood, page 58
$\mathbf{z_t}$	Simulated signal samples of tissue, page 58

Part V

Papers

Paper A

Bandwidth of the Ultrasound Doppler Signal with Applications in Blood/Tissue Segmentation in the Left Ventricle

Sigve Hovda, Håvard Rue and Bjørn Olstad

Norwegian University of Science and Technology, Trondheim, Norway,
sigveh@idi.ntnu.no
http://idi.ntnu.no/~sigveh

Accepted in Proceedings of Medical Imaging and Informatics, Beijing 2007

Abstract. A new estimator, Bandwidth Imaging, related to the bandwidth of the ultrasound Doppler signal is proposed as a classification function of blood and tissue signal in transthoracial echocardiography of the left ventricle. An in vivo experiment is presented, where the apparent error rate of Bandwidth Imaging is compared with the apparent error rate of Second-Harmonic Imaging on 15 healthy men. The apparent error rates are calculated from the 16 myocardial wall segments defined in [1]. A hypothesis test of Bandwidth Imaging having lower apparent error rate than Second-Harmonic Imaging is proved for a p-value of 0.94 in 3 segments in end diastole and in 1 segment in end systole. When data was averaged by a structural element of 5 radial, 3 lateral and 4 temporal samples the numbers of segments increased to 9 in end diastole and to 6 in end systole. This experiment indicates that Bandwidth Imaging can supply additional information for automatic border detection routines on endocardium.

1 Introduction

The ejection fraction is one of the most commonly measured parameters in diagnosis and follow up of coronary heart decease, valve decease and heart failure. The ejection fraction is the ejected volume divided by the maximum volume of the left ventricle, and measuring ejection fraction involves defining the endocardial border, either automatically or by manual tracing.

In ejection fraction calculation, the endocardial border has to be traced in at least two scan planes in both end diastole and end systole. In stress echo examination, ejection fraction is commonly calculated at three levels of stress. A robust routine for detecting endocardium automatically is needed to save examination time.

Many approaches have been suggested to solve the endocardium tracking problem. We mention here briefly; active contour models (snakes) [2] to [6] , active shape models [7] to [10] , region-growing scheme [11] and Hough transform [12]. Common for all these approaches is that they are all applied on Second-Harmonic Imaging data.

However, GE Vingmed Ultrasound AS Vivid 7 has an automatic routine that uses Tissue Velocity Imaging data in addition to Second-Harmonic Imaging data. Prior to the border detection, the atrial ventricular plane and apex are detected using an algorithm that searches for points with desired gray scale intensity and tissue movement. A simple version of this apex and atrial ventricular plane detection algorithm is presented in Storaa et al. [13]. This is an interesting example of how robustness can be achieved by using other data sets than Second-Harmonic Imaging.

It is an important point, that Bandwidth Imaging is not the same as the Variance-mode, available on most conventional Color Flow Imaging systems. In the Variance-mode, the variance of the blood flow estimate is estimated by the square of the bandwidth divided by the packetsize [14] (page 10.20). Prior to the variance estimates, the signal is highpass filtered to remove clutter noise from surrounding tissue. This improves the variance estimates in the blood pool. Hence in tissue, the signal ends up containing mostly white noise, which is not at all related to the motion of the scatterers in the actual range cell. The variance estimates are therefore not suited for blood pool definition in Color Flow Imaging systems. In general, only the power of the highpass filtered Doppler signal is used for this purpose.

In Bandwidth Imaging contradictory, signal from tissue is only partially attenuated before the bandwidth estimate. The signal from tissue has therefore a narrow bandwidth, while signal from blood has broader bandwidth, since this signal is a mixture of blood signal and clutter noise. Bandwidth Imaging is therefore used as a classification function.

In Power Doppler the packetsize has to be at least 6 to achieve a useful stopband in the highpass filter [15]. However in Bandwidth Imaging, a 2-tap Finite Impulse Response highpass filter is sufficient and this filter is available with a packetsize of 3. The temporal resolution is proportional to the packetsize and this gives an important resolution gain compared to Power Doppler. Further, spatial resolution and framerate are increased by using Multi-Line acquisition. Multi-Line acquisition is reconstruction of multiple scan lines from sparsely transmitted scan lines. This means that Bandwidth Imaging is available at a temporal and spatial resolution that is interesting in endocardial border detection.

In order to discuss the usefulness of Bandwidth Imaging, an in vivo experiment on 15 healthy male is introduced. A similar experiment is suggested by Spencer et. al. in [16]. Here, the visualization of Second-Harmonic Imaging and Fundamental Imaging were rated by expert cardiologists in all myocardial segments outlined in [1]. However, the visual differences between Bandwidth Imaging and Second-Harmonic Imaging are more radical than the visual differences between Fundamental Imaging and Second-Harmonic Imaging. Therefore, a test which is less dependent on visual perception is introduced in this paper .

2 Bandwidth Imaging

The bandwidth estimator is found to be

$$B^2 = 2 - 2\frac{|r(1)|}{r(0)} \quad \text{where} \quad r(m) = \frac{1}{N}\sum_{n=0}^{N-m-1} \overline{z_n} z_{n+m} \quad \text{for} \quad 0 \leq m \leq N-1 \quad (1)$$

in [14] and [17]. Here $r(m)$ is the autocorrelation function z_n is the signal. In Bandwidth Imaging the packet size N is set to 3. Notice that the signal dependent part of B^2, is dependent on the absolute value of the normalized autocorrelation function with lag one. For simplicity Bandwidth Imaging is defined as:

$$\text{Bandwidth Imaging} = \frac{|r(1)|}{r(0)} \quad (2)$$

Bandwidth Imaging is therefore high when bandwidth is small and visa verse. This is because Bandwidth Images should be white in tissue and black in blood, similar to Second-Harmonic Images.

The appearance of white noise biases the estimate downward, while clutter noise biases the estimate upward. To compensate for the effect of clutter noise, a 2-tap Finite Impulse Response highpass filter prior to autocorrelation calculation is introduced

$$\begin{aligned} x_1 &= z_2 - 10^{-\frac{\text{AF}}{20}}\, z_1 \\ x_2 &= z_3 - 10^{-\frac{\text{AF}}{20}}\, z_2 \end{aligned} \quad (3)$$

where AF is the attenuation factor at zero frequency in dB. When AF is high the filter can be regarded as a stationary canceling filter and the transfer function is given in [17] (page 209). In apical views, the clutter noise level is high in the near field and the white noise level increases by depth due to depth gain compensation. We have therefore found it reasonable to let AF decrease linearly from 40 dB to 15 dB in images from apical views with depth 15 cm.

2.1 Instrumentation of Bandwidth Imaging

The strategy for implementation of Bandwidth Imaging is by trial and error of various pulse strategies on a scanner (Vivid 7, GE Vingmed Ultrasound AS (Horten)) . A reasonable pulse strategy for Bandwidth Imaging is given in Table 1. The pulse strategy for Second-Harmonic Imaging, which is used in section 3, is shown for comparison.

The center frequency for Bandwidth Imaging is a trade off between lateral resolution and penetration and is set to 2.5 MHz. The pulse length of 0.7 mm is chosen as a trade off between radial resolution and sensitivity. The pulse repetition frequency is set to 3750, as a trade of between reverberation noise from earlier shots and transit time effects in tissue. The transit time effect is the effect of decorrelation of signal due to movement of scatterer inside the range

Table 1. Parameters related to the transducer for Bandwidth Imaging and Second-Harmonic Imaging

Parameter	Bandwidth Imaging	Second-Harmonic Imaging
Center frequency trans./rec.	2.5/2.5 MHz	1.7/3.4 MHz
Pulse Repetition frequency	3.75 kHz	4.25 kHz
Multi-Line Aqusition	4	2
Packetsize	3	1
Radial resolution	$6.67 \cdot 10^{-4}$ m	$4.6 \cdot 10^{-4}$ m
Aperture	$2.2 \cdot 10^{-3} \times 2.0 \cdot 10^{-3}$ m^2	$2.2 \cdot 10^{-3} \times 2.0 \cdot 10^{-3}$ m^2
Depth	0.15 m	0.15 m
Focal point (single)	0.15 m	0.09 m
Framerate	44	44
Number of beams	127	193

cell. The packet size is 3, which is the lowest possible for calculating Bandwidth Imaging with the filter given by equation (3).

Note that the pulse length is about 50 % longer in Bandwidth Imaging than in Second-Harmonic Imaging. Also, Bandwidth Imaging contains approximately 33 % less beams per frame than Second-Harmonic Imaging. This is because the framerate of Bandwidth Imaging is equal to the framerate of Second-Harmonic Imaging, the packet size is three times higher, the Multi-Line acquisition parameter is doubled and pulse repetition frequency is about the same.

The In Quadrature (signal after complex demodulation in the signal chain) data is recorded and saved to a file for further post-processing in Matlab (The MathWorks Inc.). In Bandwidth Imaging, signal is highpass filtered by equation (3) and then calculated by equation (2). Second-Harmonic Imaging is calculated by log compressing the square root of $r(0)$. The images are then scan converted to get physical scale and histogram equalized to get comparable contrast.

3 Experiment for comparing Bandwidth Imaging with Second-Harmonic Imaging

3.1 Methods

The test included 15 healthy male persons aged 24 to 32. The image qualities were acceptable, which means that decent agreement with Magnetic Resonance Images [18] were expected. The three standard apical views, four-chamber, two-chamber and long-axis view were recorded in one loop each. The pulse strategy and the instrumentation details were the same as given in section 2.

The depth was set to 15 cm and a single transmit focus was chosen in both Second-Harmonic Imaging and Bandwidth Imaging to get better resolution. In this study all depth gain compensations were equalized for all depths to eliminate for this variability.

The subjects were asked to hold their breath and keep still during recording. This enabled the examiner to compare Second-Harmonic Imaging and Bandwidth Imaging from the same positions. The examiner traced endocardium in the Second-Harmonic Images in both end systole and end diastole in all three

views. Immediately after tracing in the Second-Harmonic Images, the same traces were shown in the corresponding Bandwidth Images. In cases where the subject moved under the examination, the examiner retraced on the Bandwidth Images.

In article [1], recommendations for nomenclature and standardized segmentation of myocardium are given. The sixteen segmentation model for echocardiography is shown in the bulls-eye diagram in Fig. 1(d).

From the manual traces of endocardium, the shape and position of myocardial segments are calculated. This is done by first finding the left ventricle long-axis. Then three perpendicular lines to the long axis line are calculated. These three lines intersect the long-axis at the bottom, one third up and two thirds up. These three lines also intersect the endocardium trace at six points. A seventh point is found as the intersection between the endocardium trace and the long-axis view trace. These seven points define the corner points of the myocardial segments along endocardium. The width of each myocardial segment is set to 20 % of the myocardial short axis. These segments are seen in figure 1(a), 1(b) and 1(c). Here corresponding blood segments are shown on the inside of endocardium. The number labels are denoted in the blood segments, corresponding to the myocardial segments.

All recorded data inside each myocardial segment and each blood segment were stored in an array, with labels of subject number, segment name, segment type (blood or tissue), method (Second-Harmonic Imaging of Bandwidth Imaging) and time instance (end diastole or end systole).

Evaluation criteria for classification functions A comprehensive discussion of classification theory can be found in [19]. The quantity apparent error rate is chosen to evaluate the performance of the classification functions Bandwidth Imaging and Second-Harmonic Imaging. Advantages of apparent error rate are that it is easy to implement and not dependent of the form of the parent populations.

Let the measured data from tissue be π_t and the measured data from blood be π_b, then we suggest this definition of apparent error rate

$$\text{Apparent error rate} = \min_{T} \left(\frac{\sum_{i=1}^{n_{bMT}} c_{bMTi} + \sum_{i=1}^{n_{tMT}} c_{tMTi}}{\sum_{i=1}^{n_b} c_{bi} + \sum_{i=1}^{n_t} c_{ti}} \right) \tag{4}$$

Here, n_t and n_b are the sizes of π_t and π_b, while, n_{tMT} and n_{bMT} are the number of misclassifications in π_t and π_b at the threshold is T. Further, the cost of a sample i in π_b or π_t are c_{bi} or c_{ti}. The costs of misclassifications in blood and in tissue are c_{bMTi} and c_{tMTi}. The values of c_{bi}, c_{ti}, c_{bMTi} and c_{tMTi} are equal to the area the measurements are representing in an image. The Apparent error rate is therefore the proportion of misclassified area, given the best possible threshold. It is important to emphasize that the threshold is constant only inside one segment. Prior to apparent error rate and GM calculation the images have either been non averaged, moderately averaged or strongly averaged. In moderate averaging, the structural element is 3 radial, 2 lateral and 3 temporal samples in Second-Harmonic Imaging. To account for the resolution loss in Bandwidth

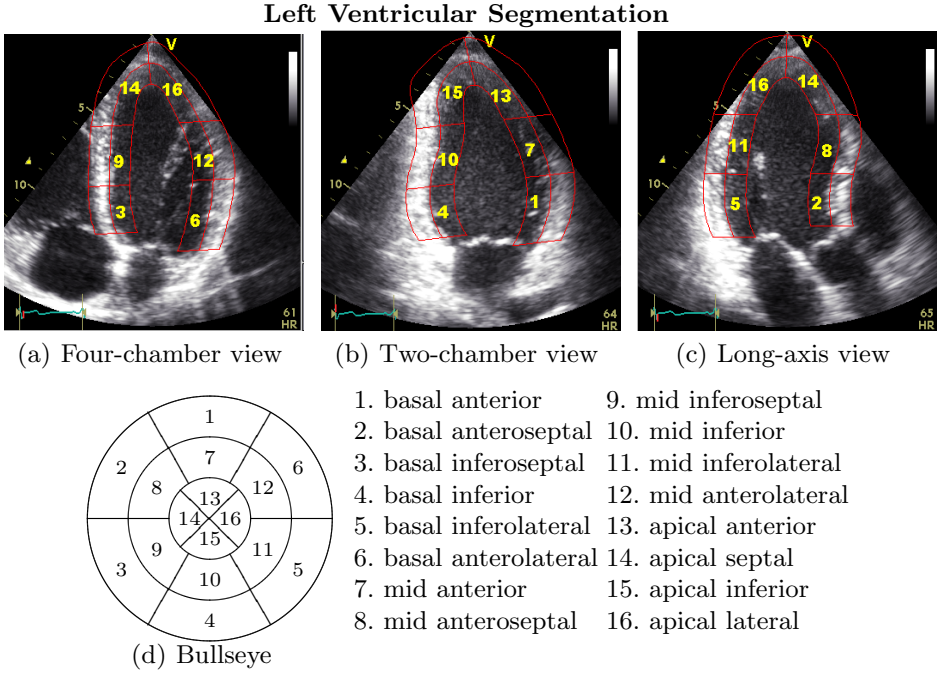

(a) Four-chamber view (b) Two-chamber view (c) Long-axis view

(d) Bullseye

Fig. 1. Display, on circumferential polar plot, of the 16 myocardial segments and recommended nomenclature recommended for echocardiography.

Imaging, the structural element in moderate averaging is reduced to 2 radial, 2 lateral and 2 temporal samples. In strong averaging, the structural element is 5 radial, 3 lateral and 4 temporal samples in Second-Harmonic Imaging and 4 radial, 2 lateral and 4 temporal samples in Bandwidth Imaging.

3.2 Results

The occasions where the apparent error rate of Bandwidth Imaging is smaller than apparent error rate of Second-Harmonic Imaging are counted in all segments. This number ranges from 0 to 15, since 15 subjects attended the study. The result is shown in column one and three in Fig. 4. If numbers are 11 or above, the p-values are higher than 0.94 on the hypothesis test; true apparent error rate of Bandwidth Imaging is equal or lower than true apparent error rate of Second-Harmonic Imaging.

This indicates that Bandwidth Imaging classifies better than Second-Harmonic Imaging in these segments, and these segments are therefore marked green. Segments with numbers four and below are marked red, because the test indicates that Second-Harmonic Imaging has a lower apparent error rate than Bandwidth Imaging in these segments. The first column shows results of end diastole and the third column shows results of end systole.

In apical septal and in apical lateral segments a super-index and a sub-index are given. The super-index tells us which view has the lowest mean apparent error

rate taken over subjects in Bandwidth Imaging. Correspondingly, the sub-index shows the best view of Second-Harmonic Imaging. Here 4 means four-chamber view and L means long-axis view. In these segments, the test compares the apparent error rate of Second-Harmonic Imaging and the apparent error rate of Bandwidth Imaging from their respective best views.

The top row shows apparent error rate calculated from not averaged data. In end diastole, the test indicates that Second-Harmonic Imaging has a smaller apparent error rate than Bandwidth Imaging in basal inferoseptal, basal inferior, basal inferolateral, basal anterolateral, mid inferoseptal and mid inferior. Contradictory, the test indicates that Bandwidth Imaging has a smaller apparent error rate than Second-Harmonic Imaging in mid anterior, mid anterolateral and apical lateral. The test can not indicate which method has the smallest apparent error rate in the other segments. In end systole, the high scores of Second-Harmonic Imaging are found in basal anteroseptal, basal inferoseptal, basal inferior, basal inferolateral, basal anterolateral, mid inferoseptal, mid inferior, mid inferolateral and mid anterolateral. The only high score of Bandwidth Imaging is found in the mid anterior segment. The test can not indicate which method has the lowest apparent error rate in the other segments.

In the mid and bottom row of Fig. 4 the test is performed on moderately and strongly averaged data, respectively. In end systole with moderate averaging, the basal anterior, mid anteroseptal, apical anterior and apical septal becomes green in addition to the green segments of the non averaged data. The basal anterolateral segment however, goes from red to undecidable. In strong averaging also basal anteroseptal and apical inferior become green, while mid inferior and basal inferolateral go from red to undecidable.

In end systole with moderate averaging, the apical anterior segment becomes green, while basal anteroseptal, basal inferolateral, mid inferolateral and mid anterolateral segments go from red to undecidable. In strong averaging basal anterior, mid anteroseptal, apical inferior and apical lateral go from undecidable to green. The mid inferior segment goes from red to undecidable.

The effect of averaging is therefore that the number of green segments is increased from 3 to 7 to 9 in end diastole and from 1 to 2 to 6 in end systole. Also, the number of red segments is reduced from 6 to 5 to 3 in end diastole and from 9 to 5 to 4 end systole.

In the second and fourth column of Fig. 4 mean apparent error rate taken over subjects is shown in percent for Bandwidth Imaging (top number) and Second-Harmonic Imaging (bottom number). Second column shows end diastole and fourth column shows end systole. In apical septal and apical lateral segments the minimum value is shown, corresponding to sub- and super-indexes of Fig. 4. Note that the apparent error rate decreases with averaging in every segment at any time instance (end diastole or end systole).

In column two and four in Fig. 4, we see that the apparent error rate is very different in various segments. On non averaged data, the apparent error rate of Bandwidth Imaging, varies from 0.21 to 0.37 in end diastole and 0.27 to 0.38 in end systole, while apparent error rate of Second-Harmonic Imaging, varies from

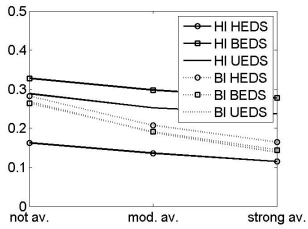

(a) End diastole segm.

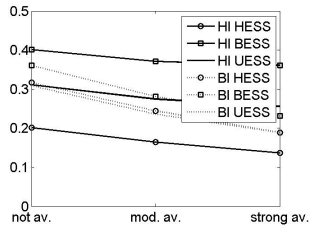

(b) End systole segm.

		Four-chamber	Two-chamber	Long-axis
End diastole	Raw	5	6	12
	Mod. av.	8	12	14
	Str. av.	11	15	14
End systole	Raw	0	6	7
	Mod. av.	1	14	10
	Str. av.	3	13	11

(c) GM result

Fig. 2. Fig. 2(a) and 2(b) show how the apparent error rate of HEDS, BEDS, UEDS, HESS, BESS und UESS behave in various averaging. Notice that the apparent error rate of the segments in Bandwidth Imaging BI are more collected and decrease faster in averaging. Notice the difference between end diastole and end systole in Bandwidth Imaging, while these differences are not present in Second-Harmonic Imaging HI. Fig. 2(c) shows the numbers of subjects were GM is lower in Bandwidth Imaging than in Second-Harmonic Imaging.

0.11 to 0.38 in end diastole and 0.16 to 0.40 in end systole. The smallest numbers of the apparent error rate are found in segments where Second-Harmonic Imaging works best, and the largest numbers of apparent error rate are found in segments where Bandwidth Imaging works best.

This effect is further investigated by grouping the segments. The segments with green numbers in top left figure in Fig. 4 are the best Bandwidth Imaging segments in end diastole BEDS. Similarly we have HEDS, which are the best Second-Harmonic Imaging segments in end diastole and the undecidable end diastole segments UEDS. In the systole we have correspondingly defined BESS, HESS and UESS from the top figure in the third column of Fig. 4.

Fig. 2(a) and 2(b) show mean apparent error rate of Second-Harmonic Imaging and Bandwidth Imaging, taken over subjects and segments in the above groups. The x axes of the figures show the level of averaging. It is clear that the Bandwidth Imaging groups are more collected than the Second-Harmonic Imaging groups. This indicates that the great regional differences seen in Fig. 4 are more a matter of regional differences of Second-Harmonic Imaging, rather than regional differences of Bandwidth Imaging. Furthermore, we see that Bandwidth Imaging decreases more rapidly by averaging than Second-Harmonic Imaging.

The result of GM is shown in the Table 2(c). Here, the occasions where GM of Bandwidth Imaging is smaller than GM of Second-Harmonic Imaging are counted for each view. This is done in end diastole and in end systole without

averaging, with moderate averaging and with strong averaging. Similarly to the result shown in Fig. 4, values above 11 are marked green and the values below 4 are marked red.

The test indicates that Second-Harmonic Imaging has a smaller GM than Bandwidth Imaging in four-chamber view in end systole in any type of averaging. On the other side, Bandwidth Imaging has a smaller GM in long-axis view in end diastole in any type of averaging. In moderate averaging two-chamber view and long-axis view are marked green in end diastole and two-chamber view is marked green in end systole. In strong averaging all views are marked green except the four-chamber view in end systole.

3.3 Discussion of the comparison experiment

In comparing Second-Harmonic Imaging and Bandwidth Imaging, the ground truth of the endocardial borders are found by manual traces on Second-Harmonic Images. It can be objected that there is a flaw in comparing two methods, when the ground truth is determined by one of them. On the other side, manual traces of endocardium on images of reasonable image quality as basis for ejection fraction measurements are reported to have reasonable agreement with ejection fraction measurements of Magnetic Resonance Imaging [18]. In this study the subjects had reasonable image qualities, and this votes for more trust to the manual traces as ground truth of endocardium. Moreover, if the manual traces are biased, it can be argued that they are biased in favor of Second-Harmonic Imaging, since they are drawn on Second-Harmonic Images. This would therefore only strengthen the results in favor of Bandwidth Imaging.

We have selected apparent error rate as the quantitative evaluation criteria of Bandwidth Imaging and Second-Harmonic Imaging. This measure is intuitive because it calculates the proportion of misclassified area, given the best threshold. In a practical clinical setting this threshold level is not known. However, automatic border detection routines are in general more dependent on a good tissue to blood contrast, rather than evenly distributed intensity levels in an image. We therefore postulate that the apparent error rate is related to the potential of an automatic detection routine of endocardium.

Further, one may argue that the threshold level is evaluated by the measured data, and therefore apparent error rate is underestimating the true optimal error rate. On the other side, it is suggested in [19] that apparent error rate is approaching the true optimal error rate when the sample sizes are high. In this experiment the sample sizes are above 1000 in all segments. And, even if apparent error rate is underestimating the true optimal error rate, the comparison of Bandwidth Imaging and Second-Harmonic Imaging may still be valid. This provides that apparent error rate is biased equally in Bandwidth Imaging and Second-Harmonic Imaging. The results of the hypothesis test, Bandwidth Imaging having lower apparent error rate than Second-Harmonic Imaging, is therefore emphasized in this paper.

In the experiment we found the lowest values of apparent error rate in segments where Second-Harmonic Imaging worked best, and the largest values of

apparent error in segments where Bandwidth Imaging worked best. This indicates that the great regional differences seen in Fig. 4 are more a matter of regional differences in Second-Harmonic Imaging, rather than regional differences in Bandwidth Imaging. This is also seen in Fig. 2(a) and 2(b).

Since the traces of endocardium in end diastole and end systole are needed for ejection fraction calculation, only these time instances are considered in this experiment. Notice also the difference between end diastole and end systole in Fig. 2(a) and 2(b). These differences are greater in Bandwidth Imaging than in Second-Harmonic Imaging.

Many automatic detection routines involve using several or all frames in a heart beat. Therefore averaged images have been considered in this study. It is important to notice from Fig. 4 that apparent error rate decreases with averaging in every segment at any time instance (end diastole or end systole). If this was not the case, it would not be fair to compare averaged data of Second-Harmonic Imaging with averaged data of Bandwidth Imaging. The result that averaging seems to favor Bandwidth Imaging can be taken as an argument for employing Bandwidth Imaging data in detection routines that use many frames.

In the experiment GM was introduced as the apparent error rate, with constant threshold value in the whole image. In prescreening methods, such as finding left ventricle center, atrial ventricular plane, apex or other features, an image with small regional variance in intensity and few dropouts are desired. We postulate that there is a relation between GM and the efficiency of prescreening algorithms in left ventricle. Here, robustness is often more important than accuracy.

3.4 Discussion of instrumentation of Bandwidth Imaging

In the process of instrumenting Bandwidth Imaging, we tried a variety of pulse repetition frequencies, pulse lengths, center frequencies and beam sizes. Also a great number of AF were tested. There is not room for a comprehensive discussion of parameter tuning in this paper. Fig. 3(b) shows Bandwidth Imaging from two-chamber view at six equally sparsed time steps in the heart cycle. Image 1 indicates end diastole and image 4 indicates end systole. In Fig. 3(a) the corresponding Second-Harmonic Images are shown. These effects are important in Bandwidth Imaging:

Tissue surrounding the cardiac muscle is more similar to tissue in the cardiac muscle in Bandwidth Imaging than in Second-Harmonic Imaging. This is because Bandwidth Imaging is more dependent on the motion of the scatterers, while Second-Harmonic Imaging is dependent on the reflection coefficient of the scatterers.

Next, the mitral valve and apparatus are not visible in Fig. 3(b). Signal from mitral valve and apparatus is a mixture of blood and tissue signal and has therefore a broader bandwidth. Moreover, signal from vibrating muscles such as in mitral apparatus is known to have broader bandwidth [20].

Further, Bandwidth Imaging is dependent of the movement of the scatterers and the image quality is therefore dependent on the acquisition time in the

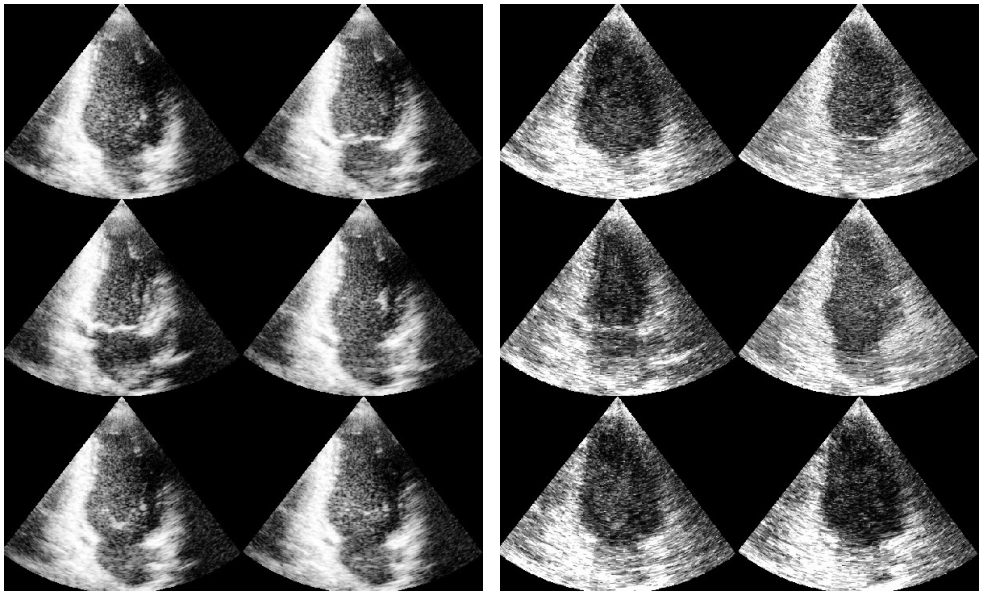

(a) Second-Harmonic Images (b) Bandwidth Images

Fig. 3. In Fig. 3(a) Second-Harmonic Images from two-chamber view are shown at six equally spaced time steps in the cardiac cycle. The end diastole is shown in the first image and the end systole is shown in the fourth image. In Fig. 3(b) the corresponding Bandwidth Images are shown.

cardiac cycle. This can be seen as image four is much brighter than image one. This can also explain the differences between end diastole and end systole seen in Fig. 2(a) and 2(b).

3.5 Conclusion

A new echocardiographic mode has been proposed, where the difference in Doppler signal from blood flow and tissue motion is utilized. A reasonable instrumentation setup of Bandwidth Imaging is outlined in this paper. A major difference between Bandwidth Imaging and conventional Power Doppler and Variance-modes on Color Flow Imaging systems is that Bandwidth Imaging does not require a long stop-band highpass filter. Bandwidth Imaging can therefore be implemented with a packetsize 3. This means that Bandwidth Imaging can be implemented with a temporal and spatial resolution that is interesting for endocardial border detection.

An experiment is added, where apparent error rate of Bandwidth Imaging is compared with apparent error rate of Second-Harmonic Imaging. The results indicate that Bandwidth Imaging can compete with Second-Harmonic Imaging in some segments, especially in apical and anterior regions. The test suggests that Bandwidth Imaging has less differences between segments, improves more by averaging and has a more uniform histogram throughout the image. This votes

for automatic routines using several time frames. In particular, we suggest using Bandwidth Imaging for prescreening methods for finding left ventricle features.

References

1. Cerqueira, M.D., Weissman, N.J., Dilsizian, V., A.K.Jacobs, S.Kaul, Laskey, W.K., D.J.Pennell, Rumberger, J.A., Ryan, T., Verani, M.S.: Standarized myocardial segmentation and nomencclature for tomographic imaging of the heart. Circulation (January 2002) 539 – 542
2. Olstad, B.: Active contours with grammatical descriptions. In: 6th International conference on Image analyses and Processing, Como Italy (sep 1991)
3. Mikic, I., Krucinski, S., Thomas, J.D.: Segmentation and tracking in echocardiographic sequences; active contour guided by optical flow estimates. IEEE Transactions on Medical Imaging **17(2)** (apr 1998) 274–284
4. Giachetti, A.: On-line analyses of echocardiographic image sequences. Med. Image anal. **2(3)** (sep 1998) 261–284
5. Bosch, J.G., Savalle, L.H., van Burken, G., Reiber, J.H.: Evaluation of semiautomatic contour detection approach to sequences of short axes two-dimensional echocardiographic images. J. Am: Soc. Echocardiogr **8(6)** (nov 1995) 810–821
6. Sonca, M., Zhang, X., Siebes, M., Bissing, M.S., DeJong, S.C., Collins, S.M., McKay, C.: Segmentation of intravascular ultrasound images: A knowledge-based approach. IEEE Transactions on Medical Imaging **14(4)** (des 1995)
7. McEachenand-2nd, M.C., Duncan, J.S.: Shape-based tracking of left ventricular wall motion. IEEE Transactions on Medical Imaging **16(3)** (jun 1997) 270–283
8. Jacob, G., Noble, A., Mulet-Parada, M., Blake, A.: Evaluation of a robust contour tracker in echocardiographic sequences. Med. Image Anal **3(1)** (1999) 63–75
9. Cootes, T.F., Taylor, C.J., Cooper, T.H., Graham, J.: Active shape models - their training and application. Computer Vision and Image Understanding **61(1)** (jan 1995) 38–59
10. Bosch, H.G., Mitchell, S.C., Lelieveldt, B.P.F., Nijland, F., Kamp, O., Sonka, M., Reiber, J.H.C.: Active appearance-motion models for fully automated endocardial contour detection in time sequences of echocardiograms. International Congress Series **1230** (jun 2001) 941–947
11. Dove, E.I., Phillip, K., Gotteiner, N.L., Vonesh, M.J., Ramberger, J.A., Reed, J.E., Standford, W., McPherson, D.D., Chandran, K.B.: A method for automatic edge detection and volume computation of the left ventricle from ultrafast computed tomographic images. Investigative Radiology **29(11)** (nov 1994) 945–954
12. Malassiotis, S., Strintzis, M.G.: Tracking the left ventricle in echocardiographic images by learning heart dynamics. IEEE Transactions on Medical Imaging **18(3)** (mar 1999) 280–290
13. Storaa, C., Grandell, A., Gustavi, T., Torp, A.H., Lind, B., Brodin, L.Å.: Simple algorithms for the automatic detection of predefined echocardiographic localisations. In: International Federation for Medical and Biological Engineering (IFMBE) Proceedings. The 12th Nordic Baltic Conference on Biomedical Engineering and Medical Physics, Berlin / New York (feb 2002) 106–107
14. Angelsen, B.A.: 7.4 ,9,3 , 10.4. In: Ultrasound Imaging Wawes, Signals and Signal Processing. Emantec, Trondheim, Norway (2000)
15. Torp, H.: Clutter rejection filters in color flow imaging a theoretical approach. IEEE Transactions on Ultrasonics, Ferroelectriscs. and Frequency Control **44** (mar 1997) 417–424

16. Spencer, K.T., Bednarz, J., Rafter, P.G., Korcarz, C., Lang, R.M.: Use of harmonic imaging without echocardiographic contrast to improve two dimensional image quality. American Journal of Cardiology **82(6)** (1998) 794–799
17. Jensen, J.A.: 6.5 and 7.5. In: Estimation of Blood Velocities Using Ultrasound. Cambridge University Press, New York, NY (1996)
18. Malm, S., Frigstad, S., Sagberg, E., andT. Skjærpe, H.L.: Accurate and reproducible measurement of left ventricular volume and ejection fraction by contrast echocardiography. Journal of the American College of Cardiology **44** (Sept 2004) 1030–1035
19. Johnson, R.A., Wichern, D.W.: Applied Multivariate Statistical Analysis. Prentice-Hall Inc (2002)
20. Heimdal, A., Torp, H.: Ultrasound doppler measurements of low velocity blood flow limitations due to clutter signals form vibrating muscles. IEEE Transactions on Ultrasonics, Ferroelectriscs. and Frequency Control **44** (jul 1997) 873–881

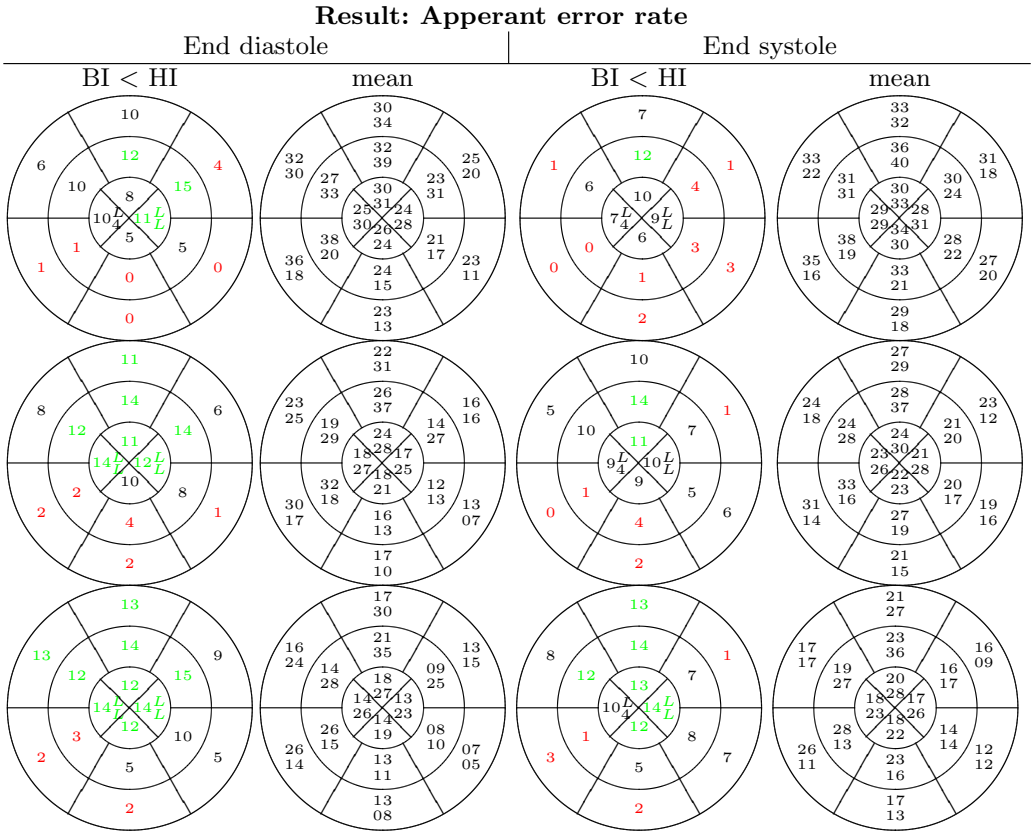

Fig. 4. Column one and three show numbers where apperant error rate is lower in Bandwidth Imaging BI than in Second-Harmonic Imaging HI in end diastole and end systole, respectively. If numbers are 11 and above they are marked green, because the hypothesis test; apperant error rate of Bandwidth Imaging is smaller than apperant error rate of Second-Harmonic Imaging is proved for a p-value is 0.94. Contradictively, numbers of 4 and below are marked red. In column two and four, the mean values of apperant error rate in percent are shown in end diastole and end systole. The top values are apperant error rate of Bandwidth Imaging and the bottom values are apperant error rate of Second-Harmonic Imaging. Top row shows result when images are not averaged, second row shows result for moderate averaging and last row shows result when data is strongly averaged.

Paper B

New Doppler-Based Imaging Method in Echocardiography with Applications in Blood/Tissue Segmentation

Sigve Hovda, Håvard Rue and Bjørn Olstad

Norwegian University of Science and Technology, Trondheim, Norway,
sigveh@idi.ntnu.no
http://idi.ntnu.no/~sigveh

Accepted in Proceedings of Medical Imaging and Informatics, Beijing 2007

Abstract. Knowledge Based Imaging is suggested as a method to distinguish blood from tissue signal in transthoracial echocardiography. This method utilizes the maximum likelihood function to classify blood and tissue signal. Knowledge Based Imaging and Bandwidth Imaging [1] are compared with Fundamental Imaging by a computer simulation. The apparent error rate is calculated in any reasonable tissue to blood signal ratio, tissue to white noise ratio and clutter to white noise ratio. Fundamental Imaging classifies well when tissue to blood signal ratio is high and tissue to white noise ratio is higher than clutter to white noise ratio. Knowledge Based Imaging classifies also well in this environment. In addition, Knowledge Based Imaging classifies well whenever blood to white noise ratio is above 30 dB, even when clutter to white noise ratio is higher than tissue to white noise ratio and tissue to blood signal ratio is small. Bandwidth Imaging performs similar to Knowledge Based Imaging, but in general blood to white noise ratio has to be 20 dB higher. Some images of Knowledge Based Imaging with different parameter settings are visually compared with Second-Harmonic Imaging, Fundamental Imaging and Bandwidth Imaging.

1 Introduction

The state of art echocardiographic modes for defining endocardium of left ventricle of the human heart are; Fundamental Imaging, Second-Harmonic Imaging and Left Ventricle Opacification. These methods distinguish blood signal from tissue signal by their differences in power [2].

Alternatively, Doppler signal from blood flow differs from tissue motion, since it is less coherent with depth. In Power Doppler, blood is distinguished from tissue signal by the power of the highpass filtered Doppler signal. Here a packetsize of above 6 is required to achieve the desired filter characteristics [3].

In paper [1], Bandwidth Imaging was introduced and the experiment indicated that tissue and blood could be distinguished with a packetsize as small as 3. The small packetsize enables a resolution that is interesting for endocardial

border definition. In this paper, we seek to discuss the theoretical potential of Knowledge Based Imaging and Bandwidth Imaging, where the pulse strategy of the optimized Bandwidth Imaging method is taken as a starting point.

In section 2 a parametric models for signal from blood and tissue are outlined and Knowledge Based Imaging is defined. In section 3, the apparent error rates of Knowledge Based Imaging, Bandwidth Imaging and Fundamental Imaging are calculated from computer generated signals in various types of noise. In section 4, some premature Knowlege based Images with different parameter settings are compared with a Fundamental Image, a Bandwidth Imaging and a Second-Harmonic Image.

2 Signal model and definition of Knowledge Based Imaging

Torp et. al. [4] introduced a parametric model for the autocorrelation functions in regions with rectilinear flow, under the assumption that signal is a complex Gaussian process. In this section, this model is expanded to yield turbulent flow as well. The signal model is also further expanded to include additive white noise and clutter noise in a similar manner as in Heimdal et. al. [5]. This is the theoretical framework for defining, instrumenting and discussing Knowledge Based Imaging and Bandwidth Imaging.

2.1 Parametric model for the autocorrelation function of signal from blood and tissue

As mentioned above the signal model of [4] is used. Here the authors assume a random continuum model for blood scattering [6]. The spatial fluctuation in mass density and compressibility, which determine the incoherent part of the scattering, is assumed proportional to the fluctuation of blood cell concentration $n_b(\mathbf{r}, t)$, where $\mathbf{r}$ is position and t is time. Here, $n_b(\mathbf{r}, t)$ is a zero mean random process. For a short correlation in space, for a fixed time and neglecting diffusion, the autocorrelation function of $n_b(\mathbf{r}, t)$ is approximated in [6] by

$$\begin{aligned} < n_b(\mathbf{r}, t), n_b(\mathbf{r} + \xi, t + \tau) > &= \boldsymbol{\Upsilon}(\mathbf{r}, t)\, \delta(\xi - \zeta(\mathbf{r}, t, \tau)) \\ \boldsymbol{\Upsilon}(\mathbf{r}, t) &= \frac{var(n_b(\mathbf{r})) \cdot \Delta V}{\Delta V} \end{aligned} \tag{1}$$

where $\zeta(\mathbf{r}, t, \tau)$ is the displacement of the fluid element in position $\mathbf{r}$ during the time interval t to $t + \tau$. The function $\boldsymbol{\Upsilon}(\mathbf{r}, t)$ is the variance per unit volume in numbers of blood cells inside a small volume ΔV, and this quantity is proportional to the backscattering coefficient in blood.

Assuming a Gaussian shaped beam profile and a rectangular shaped receiver filter impulse response, the authors outline an expression for the expected value of the two dimensional autocorrelation function for any time and radial lag. In general it is necessary to assume rectilinear flow, but in the case of no radial lag,

this assumption has to be valid inside only one range cell. The expected value of the autocorrelation function with only time lag for an electronically steered probe is

$$\begin{aligned} r(m) &= r(0)\beta(m)e^{2\mathrm{i}\,m\;k\,v_1\,T} \\ \beta(m) &= e^{-\frac{3}{2}\,m^2\left[\left(\frac{v_1\,T}{L}\right)^2+\left(\frac{v_2\,T}{\Theta_1}\right)^2+\left(\frac{v_3\,T}{\Theta_2}\right)^2\right]} \end{aligned} \tag{2}$$

according to [4]. Here the respective velocity components are v_1, v_2, v_3. Further, L is pulse length, and Θ_1 and Θ_2 are the lateral and elevation resolutions corresponding to -3.25 dB opening angle. The repetition time is T and k is the wave number, which is equal to 2π divided by the wavelength. This model yields for laminar flow. Moreover, flow in left ventricle is turbulent [7], and in the next subsection this model is expanded to yield for turbulent flow as well.

2.2 Model for turbulent blood flow

For turbulent flow we assume that the autocorrelation function for $n_b(\mathbf{r},t)$ is

$$< n_b(\mathbf{r},t), n_b(\mathbf{r}+\xi, t+\tau) >= \mathbf{\Upsilon}(\mathbf{r},t)\,\frac{1}{(2\pi)^{\frac{3}{2}}\sigma_1\sigma_2\sigma_3}\,e^{-\frac{1}{2}\left(\frac{(\xi_1-\zeta_1)^2}{\sigma_1^2}+\frac{(\xi_2-\zeta_2)^2}{\sigma_2^2}+\frac{(\xi_3-\zeta_3)^2}{\sigma_3^2}\right)} \tag{3}$$

where ζ_1, ζ_2 and ζ_3 are mean displacements and σ_1, σ_2 and σ_3 are standard deviations of displacements. Here we assume a Gaussian shaped velocity profile to describe turbulent flow. With this extra assumption, the development of the expected value of the autocorrelation function $r(m)$ can follow the same path as in paper [4]. The difference is to multiply $r(m)$ with the Gaussian probability density function of velocities and integrate over all velocities.

$$r(m) = r(0)\int_{-inf}^{inf} \partial v_x,\,\partial v_y\,\partial v_z \beta(m)\,e^{\mathrm{i}\,m\,2\,k\,v_1 T}\,e^{-\frac{1}{2}\left(\frac{(v_x-v_1)^2}{\sigma_1^2}+\frac{(v_y-v_2)^2}{\sigma_2^2}+\frac{(v_z-v_3)^2}{\sigma_3^2}\right)} \tag{4}$$

Here σ_1, σ_2 and σ_3 are redefined as the standard deviations of the velocity components. Further, v_1, v_2 and v_3 refer to the means of the velocity components. Integrating this gives

$$\begin{aligned} &r(m) = r(0)\hat{\beta}(m)\hat{\alpha}(m)\,e^{\mathrm{i}\frac{m\,2\,k\,v_1\,T}{a_1}} \qquad \text{where} \\ &\hat{\alpha}(m) = e^{-\frac{2\,m^2\,k^2\,T^2\,\sigma_1^2}{a_1^2}}, \qquad \hat{\beta}(m) = \frac{1}{a_1\,a_2\,a_3}\,e^{-\frac{3}{2}m^2\left[\left(\frac{v_1\,T}{L\,a_1}\right)^2+\left(\frac{v_2\,T}{\Theta_1\,a_2}\right)^2+\left(\frac{v_3\,T}{\Theta_2\,a_3}\right)^2\right]}, \\ &a_1 = \sqrt{3m^2\frac{\sigma_1^2\,T^2}{L^2}+1}, \quad a_2 = \sqrt{3m^2\frac{\sigma_2^2\,T^2}{\Theta_1^2}+1} \quad \text{and} \quad a_3 = \sqrt{3m^2\frac{\sigma_3^2\,T^2}{\Theta_2^2}+1} \end{aligned} \tag{5}$$

The coefficients a_1, a_2 and a_3 are close to one when $\sigma_1 T$ is small compared to L, $\sigma_2 T$ is small compared to θ_1 and $\sigma_3 T$ is small compared to θ_2. Therefore $\hat{\beta(m)}$

is close to $\beta(m)$. A simplified model for turbulent flow is therefore

$$r(m) = r(0)\beta(m)\alpha(m)\, e^{\mathrm{i}\, m\, 2\, k\, v_1\, T} \quad \text{where} \quad \alpha(m) = e^{-2\, m^2\, k^2\, T^2\, \sigma_1^2} \tag{6}$$

The effect of turbulence is covered in the $\alpha(m)$ parameter, which is a function of the radial velocity distribution alone.

2.3 Model including white noise and clutter noise

Signal is assumed to be described by three components in Heimdal's model [5]. These three components are the signal from the range cell, additive white noise with power σ_n^2 and DC clutter noise from stationary echo with power σ_c^2. We assume the same, and the autocorrelation estimate for blood $r_b(m)$ and for tissue $r_t(m)$ is modeled as:

$$\begin{array}{ll} r_b(0) = \sigma_b^2 + \sigma_c^2 + \sigma_n^2 & r_t(0) = \sigma_t^2 + \sigma_c^2 + \sigma_n^2 \\ r_b(1) = \sigma_b^2\, \beta(m)\alpha(m)\, e^{\,2\, k\, v_1\, T} + \sigma_c^2 & r_t(1) = \sigma_t^2\, \beta(m)\, e^{\,2\, k\, v_1\, T} + \sigma_c^2 \\ r_b(2) = \sigma_b^2\, \beta(m)^4 \alpha(m)^4\, e^{\,4\, k\, v_1\, T} + \sigma_c^2 & r_t(2) = \sigma_t^2\, \beta(m)^4\, e^{\,4\, k\, v_1\, T} + \sigma_c^2 \end{array} \tag{7}$$

Notice that the power terms of white noise are zero for $r_b(1)$, $r_t(1)$, $r_b(2)$ and $r_t(2)$. This is because white noise from different shots are uncorrelated. Transversing velocities are neglected in the tissue model and taken into account by the turbulent parameter in the blood model.

The probability density function for a signal $\mathbf{z}$ in blood is P_b and the probability density function for a signal $\mathbf{z}$ in tissue P_t is

$$\begin{aligned} P_b(\mathbf{z}|\sigma_b,\, \sigma_c,\, \sigma_n,\, v_b,\, \sigma_{v_b}) &= \frac{1}{\pi^N\, |\mathbf{C_b}|}\, e^{\bar{\mathbf{z}}\, \mathbf{C_b^{-1}}\, \mathbf{z}} \\ P_t(\mathbf{z}|\sigma_t,\, \sigma_c,\, \sigma_n,\, v_t) &= \frac{1}{\pi^N\, |\mathbf{C_t}|}\, e^{\bar{\mathbf{z}}\, \mathbf{C_t^{-1}}\, \mathbf{z}} \end{aligned} \tag{8}$$

where v_b and v_t are the radial velocity components in blood and tissue and σ_{v_b} is the standard deviation of the velocity profile inside one range cell in blood. Here $\mathbf{C_b}$ and $\mathbf{C_t}$ are:

$$\mathbf{C_b} = \begin{bmatrix} r_b(0) & \overline{r_b(1)} & \overline{r_b(2)} \\ r_b(1) & r_b(0) & \overline{r_b(1)} \\ r_b(2) & r_b(1) & r_b(0) \end{bmatrix} \qquad \mathbf{C_t} = \begin{bmatrix} r_t(0) & \overline{r_t(1)} & \overline{r_t(2)} \\ r_t(1) & r_t(0) & \overline{r_t(1)} \\ r_t(2) & r_t(1) & r_t(0) \end{bmatrix} \tag{9}$$

In general the parameters defining P_b and P_t are not known. If their distributions are known then

$$\begin{aligned} P_b(\mathbf{z}) &= \int_{-\inf}^{\inf} \mathrm{d}\sigma_b, \mathrm{d}\sigma_c, \mathrm{d}\sigma_c, \mathrm{d}v_b, \mathrm{d}\sigma_{v_b} P_b(\mathbf{z}|\sigma_b,\, \sigma_c,\, \sigma_n,\, v_b,\, \sigma_{v_b})\, P_{\sigma_b}\, P_{\sigma_c}\, P_{\sigma_n}\, P_{v_b}\, P_{\sigma_{v_b}} \\ P_t(\mathbf{z}) &= \int_{-\inf}^{\inf} \mathrm{d}\sigma_t, \mathrm{d}\sigma_c, \mathrm{d}\sigma_c, \mathrm{d}v_t, P_t(\mathbf{z}|\sigma_t,\, \sigma_c,\, \sigma_n,\, v_t)\, P_{\sigma_t}\, P_{\sigma_c}\, P_{\sigma_n}\, P_{v_t} \end{aligned} \tag{10}$$

where P_{σ_b} P_{σ_c} P_{σ_n} P_{v_b} $P_{\sigma_{v_b}}$ P_{σ_t} and P_{v_t} are the probability density functions for the σ_b, σ_c, σ_n, v_b, σ_{v_b}, σ_t and v_t. In practice, these probability density functions can potentially be found from a priory knowledge, estimation or experimental trial and error.

2.4 Knowledge Based Imaging

The echocardiographic mode Knowledge Based Imaging is proposed as

$$\text{Knowledge Based Imaging} = 20 \cdot \log_{10}\left[\ln\left(\frac{P_t(\mathbf{z}) + P_b(\mathbf{z})}{P_t(\mathbf{z})}\right)\right] \tag{11}$$

Here $\mathbf{z}$ is the measured complex signal vector with length equal to packet size. Knowledge Based Imaging is basically a histogram manipulated version of the maximum likelihood ratio of a signal sample. The maximum likelihood ratio is $P_t(\mathbf{z})/P_b(\mathbf{z})$, and this is described in Van Trees [8].

The histogram manipulation can be argued for in the following way: The expression $(P_t(\mathbf{z}) + P_b(\mathbf{z}))/P_t(\mathbf{z})$ is close to 1 when $P_t(\mathbf{z})$ is dominating, equal to 2 when $P_t(\mathbf{z}) = P_b(\mathbf{z})$ and approaches infinity when $P_b(\mathbf{z})$ is dominating. The natural logarithm of this becomes a number between zero and infinity. Notice that this number is dominated by the difference of the exponents in equation (8). These exponents are dominated by the power of the signal, and this motivates for the final log compression. This histogram becomes reasonably uniform.

Another interesting method is the generalized likelihood ratio test that is also described in Van Trees. In the case of Knowledge Based Imaging, this is the same as calculating Knowledge Based Imaging from equation (11), where $P_t(\mathbf{z})$ and $P_b(\mathbf{z})$ are substituted with $\hat{P}_t(\mathbf{z})$ and $\hat{P}_b(\mathbf{z})$;

$$\begin{aligned}
\hat{P}_b(\mathbf{z}) &= \max_{R_b}(P_b(\mathbf{z}|\sigma_b, \sigma_c, \sigma_n, v_b, \sigma_{v_b})) \quad \text{where} \quad (\sigma_b, \sigma_c, \sigma_n, v_b, \sigma_{v_b}) \,\epsilon\, R_b \\
\hat{P}_t(\mathbf{z}) &= \max_{R_t}(P_t(\mathbf{z}|\sigma_t, \sigma_c, \sigma_n, v_t)) \quad \text{where} \quad (\sigma_t, \sigma_c, \sigma_n, v_t) \,\epsilon\, R_t
\end{aligned} \tag{12}$$

Obviously, Knowledge Based Imaging requires definition of parameter space in tissue R_t and blood R_b. In this manuscript, this is done by defining the upper and lower limits of the parameters. This is hereby referred to as Knowledge Based Imaging with box constraints.

2.5 Fundamental Imaging

In the computer simulation, Fundamental Imaging is defined as

$$\text{Fundamental Imaging} = 20\log_{10}(r(0)) \quad \text{where} \quad r(m) = \frac{1}{3}\sum_{n=0}^{3-m-1} \overline{z_n} z_{n+m} \tag{13}$$

Note that no highpass filter is used prior to Fundamental Imaging calculation.

Table 1. Parameters related to the transducer for Fundamental Imaging, Bandwidth Imaging, Knowledge Based Imaging and Second-Harmonic Imaging

Parameter	Fundamental Imaging Bandwidth Imaging Knowledge Based Imaging	Second-Harmonic Imaging
Center frequency trans./rec.	2.5/2.5 MHz	1.7/3.4 MHz
Pulse repetition frequency	3.75 kHz	4.25 kHz
Multi-Line Acquisition	4	2
Packetsize	3	1
Radial resolution	$6.67 \cdot 10^{-4}$ m	$4.6 \cdot 10^{-4}$ m
Aperture	$2.2 \cdot 10^{-3} \times 2.0 \cdot 10^{-3}\,\mathrm{m}^2$	$2.2 \cdot 10^{-3} \times 2.0 \cdot 10^{-3}\,\mathrm{m}^2$
Depth	0.15 m	0.15 m
Focal point (single)	0.15 m	0.09 m
Framerate	44	44
Number of beams	127	193

2.6 Bandwidth Imaging

In paper [1] Bandwidth Imaging is defined as

$$\text{Bandwidth Imaging} = \frac{|r(1)|}{r(0)} \tag{14}$$

and prior to the autocorrelation estimate the signal is filtered with this 2-tap Finite Impulse Response filter

$$\begin{aligned} x_1 &= z_2 - 10^{-\frac{\mathrm{AF}}{20}}\, z_1 \\ x_2 &= z_3 - 10^{-\frac{\mathrm{AF}}{20}}\, z_2 \end{aligned} \tag{15}$$

where AF is the attenuation factor at zero frequency.

2.7 Pulse strategy

The pulse strategy of Bandwidth Imaging, Knowledge Based Imaging and Fundamental Imaging is given in Table 1. The center frequency for Bandwidth Imaging, Knowledge Based Imaging and Fundamental Imaging is a trade off between resolution and penetration and is set to 2.5 MHz. The pulse length (0.7 mm) is chosen as a trade off between radial resolution and sensitivity. The pulse repetition frequency is set to 3750 , as a trade off between reverberation noise from earlier shots and transit time effects in tissue. The transit time effect is the effect of decorrelation of signal due to movement of scatterers in the range cell. The packet size is 3, which is the lowest possible for calculating Bandwidth Imaging with the filter given by equation (15).

3 Evaluation of Knowledge Based Imaging, Bandwidth Imaging, Fundamental Imaging by computer simulation

3.1 Methods

In this chapter the classification functions Knowledge Based Imaging, Bandwidth Imaging and Fundamental Imaging are evaluated and compared using the quantity apparent error rate. A comprehensive discussion of classification theory can be found in [9]. Here apparent error rate is defined as

$$\text{Apparent error rate} = \min_{T} \left(\frac{n_{bMT} + n_{tMT}}{n_b + n_t} \right) \tag{16}$$

where, n_t and n_b are the sizes of measured data from tissue π_t and from blood π_b. Further, n_{tMT} and n_{bMT} are the number of misclassifications of π_t and π_b at threshold T. Apparent error rate is simply the proportion of misclassifications, given the best threshold level.

In this experiment, 2000 signal samples from blood and 2000 signal samples from tissue are generated from a random generator. Here the pulse strategy is given in Table 1, which is the same pulse strategy as in paper [1]. Speed of sound c is 1540m/s. Blood signal $\mathbf{z_b}$ and tissue signal $\mathbf{z_t}$ are created by

$$\begin{aligned} \mathbf{z_b} &= \mathbf{L_b}\,\mathbf{x_1} \qquad & \mathbf{C_b} &= \mathbf{L_b}^T\mathbf{L_b} \\ \mathbf{z_t} &= \mathbf{L_t}\,\mathbf{x_2} \qquad & \mathbf{C_t} &= \mathbf{L_t}^T\mathbf{L_t} \end{aligned} \tag{17}$$

where $\mathbf{x_1}$ and $\mathbf{x_2}$ are normalized complex Gaussian signal created by the random generator. Moreover, $\mathbf{L_t}$ and $\mathbf{L_b}$ are the lower triangular matrices, obtained by Cholesky factorization of $\mathbf{C_b}$ and $\mathbf{C_t}$ given in equation (9). Fundamental Imaging is calculated by equation (13), Knowledge Based Imaging by equation (11), and Bandwidth Imaging by equation (14).

For simplicity $\mathbf{C_b}$ and $\mathbf{C_t}$ are divided by σ_n^2, so that apparent error rate is discussed for various blood to white noise ratio, tissue to white noise ratio, and clutter to white noise ratio. It is also interesting to discuss the ratio between tissue and blood signal.

The parameters v_t and v_b are picked randomly from two Gaussian distributions with mean zero and standard deviation 0.025 m/s and 0.25 m/s, respectively. The parameter σ_{v_b} is set to zero in simulations where laminar flow is assumed. In simulations where turbulent flow is assumed σ_{v_b} is chosen to 0.1 m/s.

3.2 Results

In column one through four in Fig. 1, the apparent error rate is color coded to show its level at any tissue to white noise ratio, clutter to white noise ratio and tissue to blood signal ratio. The color bar goes from 0 (red) to 0.5 (blue). All these subplots show tissue to white noise ratio (y-axis) versus clutter to white

noise ratio (x-axis) from 0 to 140 dB. In the bottom row tissue to blood signal ratio is 0 db, and this ratio increases by increment of 10 dB in the next rows.

In the first column, blood and tissue signal are separated by Fundamental Imaging. Obviously apparent error rate is dependent on tissue to blood signal ratio, and it is necessary that clutter to white noise ratio is lower than tissue to white noise ratio for reasonable classification.

In column two, blood and tissue signal are separated by Knowledge Based Imaging. Here the velocity distributions of tissue and blood have standard deviations of 0.025 m/s and 0.25 m/s, respectively. The turbulence parameter is set to zero. We see that Knowledge Based Imaging classifies better than Fundamental Imaging everywhere. Note that a reasonable classification is possible whenever blood to white noise ratio is above 30 db, regardless of tissue to blood signal ratio and clutter to white noise ratio. This can be seen by noting the relation tissue to white noise ratio = tissue to blood signal ratio + blood to white noise ratio. This effect is even stronger in the third column, where the turbulence parameter in blood is turned up to 0.1 m/s.

In the case of Bandwidth Imaging, only one parameter has to be set, namely AF. The same signal as in third column , is highpass filtered by different AF ranging from 0 to 50 dB. The AF that minimizes apparent error rate is chosen, and the best value of apparent error rate is shown in the fourth column Bandwidth Imaging performs similar to Knowledge Based Imaging, but the general trend is that blood to white noise ratio has to be 20 dB higher for the same level of apparent error rate. It is also important to mention that Bandwidth Imaging performs worse than Fundamental Imaging in regions where tissue to blood signal ratio is high, tissue to white noise ratio low and clutter to white noise ratio smaller than tissue to white noise ratio.

The fifth column shows the best possible AF on a scale from 0 (blue) to 50 dB (red). It is seen that AF is smooth in regions where Bandwidth Imaging classify well. This coefficient seems linearly dependent on blood to white noise ratio and clutter to white noise ratio. The last column shows the best threshold level on a scale from 0 (blue) to 1 (red). Here we see that the threshold level seems smooth and not AF-dependent in regions where Bandwidth Imaging classify well.

3.3 Discussion of computer simulation

In this signal model we assumed one and the same pulsestrategy for Bandwidth Imaging, Knowledge Based Imaging and Fundamental Imaging. If different pulsestratgies were compared, the results would be very dependent on the signal model. In that case, the signal model had to be validated for every choice of pulse strategies. In our case, we simply have to assume that the backscattered signal can be described by these three components; signal from blood or tissue in a range cell, uncorrelated white noise and stationary clutter noise.

It can be argued that Fundamental Imaging does not have optimized pulse strategy and the comparison is therefore favoring Knowledge Based Imaging. Moreover, the state of art echocardiographic mode is Second-Harmonic Imaging, which is reported to be an improvement compared to Fundamental Imag-

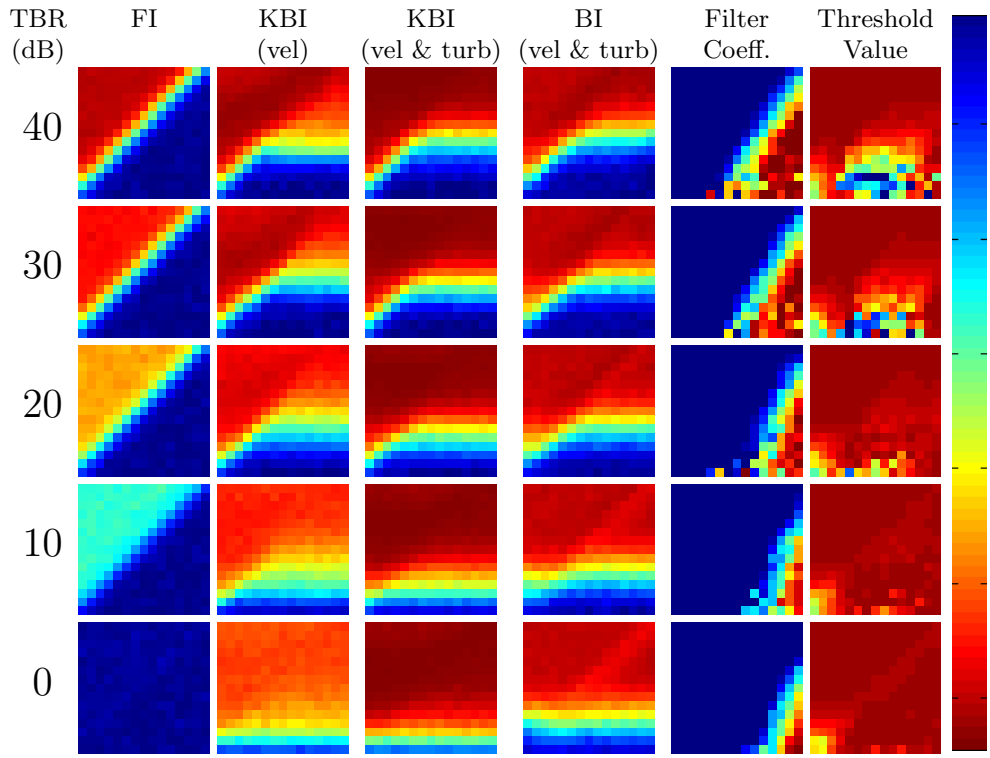

Fig. 1. In column one through four, the apparent error rate is color coded to show its level at any tissue to white noise ratio, clutter to white noise ratio and tissue to blood signal ratio TBR. The color bar goes from 0 (red) to 0.5 (blue). All subplots show tissue to white noise ratio versus clutter to white noise ratio from 0 to 140 dB. In the first row tissue to blood signal ratio is 0 db and in the next rows tissue to blood signal ratio increases by increment of 10 dB to 40 dB. In the first column blood and tissue signal are separated by Fundamental Imaging FI. Obviously, the apperant error rate is dependent on tissue to blood signal ratio. Furthermore, it is necessary that clutter to white noise ratio is lower than tissue to white noise ratio for a reasonable classification. In column two blood and tissue signal are separated by Knowledge Based Imaging KBI. Here the velocity distributions of tissue and blood have standard deviations of 0.025 m/s and 0.25 m/s, respectively. We see that Knowledge Based Imaging classified better than Fundamental Imaging everywhere. It is interesting to see that a reasonable classification is possible when blood to white noise ratio is above 30 dB, regardless of tissue to blood signal ratio and clutter to white noise ratio. This effect is even stronger in the next column, where the turbulence parameter in blood is turned up from 0 to 0.1 m/s. In column four, the same signal as in column three is classified by Bandwidth Imaging BI. The fifth column shows the best AF, where the color bar varies from 0 (blue) to 50 dB (red). The last column shows the best threshold level for the BI classification, on the scale from 0 (blue) to 1 (red).

ing [10]. The aim of this comparison is therefore not to determinate whether Knowledge Based Imaging or Bandwidth Imaging are better than conventional methods. The aim is rather to outline differences in how Knowledge Based Imaging, Bandwidth Imaging and Fundamental Imaging classify in various types of noise.

For the same reason, the computer simulation covers only a subset of all types of signal and noise environments that can be expected in transthoracial echocardiography. This subset is limited in three ways.

First, the velocity distributions of scatterers in π_t and π_b are assumed Gaussian with standard deviation 0.025 m/s and 0.25 m/s. These distributions are chosen, because they seem reasonable at depth 7.5 cm from apical views. Other velocity distributions could be chosen as well. For instance, the velocity of the atrial ventricular plane is normally above 0.085 m/s in end systole and the velocity of the mitral flow yet can exceed 1 m/s. It is important to mention that pulse repetition frequency can be adjusted to get optimal classification for any two samples of blood and tissue signal. Hence, the difference in velocity distributions is the governing parameter.

Next, blood flow in left ventricle is found to be turbulent by Schoephoerster and Chandran [7]. Turbulence comes into the model, by the assumption that the scatterers in a range cell have a Gaussian velocity distribution with standard deviation 0.1 m/s. This argument could be challenged, both because of the shape of the distribution and also the size of the standard deviation.

And third, the assumption that clutter noise comes only from stationary signal could be challenged. This is because clutter noise also comes from moving tissue.

In the experiment, apparent error rate is used to estimate the true optimal error rate. In [9] apparent error rate is reported to underestimate the true optimal error rate, because the data used to build the classification rule is also used to evaluate the rule. However, this underestimation is reduced by using a large sample size.

In transthoracial echocardiography the clutter level is high in the near-field, due to the penetration of inhomogeneous tissue. Also the level of white noise increases downward the beam, due to depth gain compensation. The above results indicate that the greatest potential of Knowledge Based Imaging is in the apical region, where high clutter to white noise ratio can be compensated by high blood to white noise ratio.

Bandwidth Imaging performed similar to Knowledge Based Imaging, but the general trend is that blood to white noise ratio had to be about 20 dB higher for the same level of apparent error rate. This can explain why the best results of Bandwidth Imaging were found in apical segments in the experiment in paper [1] . In column five in figure 1, AF is plotted in different types of noise. This coefficient seems linearly dependent of blood to white noise ratio and clutter to white noise ratio in the dB scale. This may explain why it seems reasonable to use a depth dependent clutter rejection filter prior to the Bandwidth Imaging calculation in [1].

In the next section the attention is drawn back to Knowledge Based Imaging, where some premature images are discussed.

4 Discussion of instrumentation of Knowledge Based Imaging

The strategy for implementation of Knowledge Based Imaging is to use the pulse strategy of Table 1 on a scanner (Vivid 7, GE Vingmed Ultrasound AS (Horten)) . If we use the generalized maximum likelihood definition of Knowledge Based Imaging with box constraints, there are 14 parameters to adjust. These are the upper and lower limits of σ_t,σ_b,σ_c,σ_n,v_t,v_b and σ_{v_b}. This section contains some examples of instrumentation of Knowledge Based Imaging with box constraints. In this case, the box constraints can be tuned so Knowledge Based Imaging can look similar to both Bandwidth Imaging and Fundamental Imaging.

Knowledge Based Imaging at one range cell is calculated in this way: A five dimensional array of values of $\sigma_b, \sigma_c, \sigma_n, v_b$ and σ_{v_b} is created and limited by the box constraints. Next, all $P_b(\mathbf{z})$ are calculated and the maximum value determined. A similar path is followed to calculate maximum of $P_t(\mathbf{z})$. Finally, Knowledge Based Imaging is calculated by equation (11).

Fig. 2 shows six four-chamber view images of a healthy mature male with different echocardiographic modes. Fig. 2(a), 2(b) and 2(c) show Second-Harmonic Imaging, Fundamental Imaging and Bandwidth Imaging, respectively.

Fig. 2(d), 2(e) and 2(f) show three variants of Knowledge Based Imaging. In these images, σ_n is set to increase from 10 dB to 20 dB downward in the image. In Fig. 2(e) KBI 2 is shown. Here, v_b and v_t are set at 7 steps between - 1 to 1 m/s. Here, σ_{v_b} and σ_c are both set to zero. The only parameters separating $\hat{P}_t(\mathbf{z})$ and $\hat{P}_b(\mathbf{z})$, are σ_b and σ_t. These are given at 3 equally spaced steps from 50 to 100 dB in blood and 120 to 150 dB in tissue. We see that the KBI 2 is similar to Fundamental Imaging. They are related in the way that they both separate blood from tissue signal by their difference in power.

KBI 3 is shown in Fig. 2(f). Here there is no separation by power at all and σ_b and σ_t are set in three steps between 40 to 140 dB. The separation between blood and tissue signal is by velocity and velocity distribution. Here, v_b is set at seven steps between - 1 to 1 m/s. Further, the magnitude of velocity in tissue v_t is limited by 0.013 m/s in the apical region, and this magnitude is increased linearly to 0.13 m/s at 15 cm depth. This is because the radial velocities in myocardium are higher in the atrial ventricular plane region, than closer to apex. Moreover, the turbulence parameter σ_{v_b} is set to 0.12 m/s. It is important to mention that the image is enhanced by setting this parameter. Also the clutter parameter is set. The clutter parameter is set to decrease linearly downward in the image from 140 to 80 dB. The net effect of setting this parameter is similar to clutter filtering in Bandwidth Imaging. It is interesting that KBI 3 becomes similar to Bandwidth Imaging. The fact that Knowledge Based Imaging can be adjusted between the two extremes that look similar to Fundamental Imaging

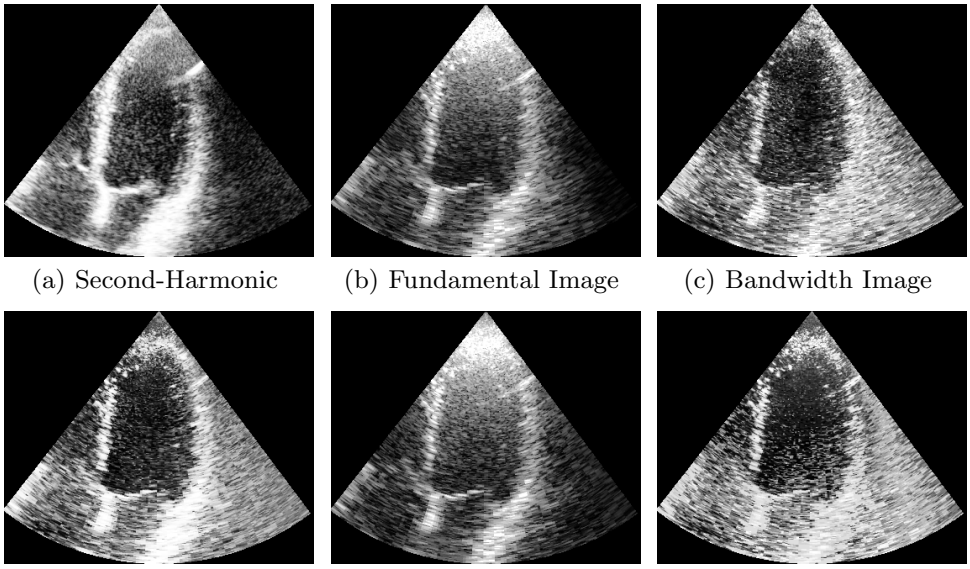

(a) Second-Harmonic (b) Fundamental Image (c) Bandwidth Image

(d) KBI 1 (e) KBI 2 (f) KBI 3

Fig. 2. Four-chamber views of a healthy heart with different imaging modes. Fig. 2(a), 2(b) and 2(c) show Second-Harmonic Image, Fundamental Image and Bandwidth Image, respectively. In Fig. 2(e) Knowledge Based Imaging is adjusted so that blood and tissue signal are separated by their differences in power. This image (KBI 2) is therefore similar to Fig. 2(b). In Fig. 2(f) (KBI 3) parameters are adjusted so that blood and tissue signal are separated by their differences in velocities and turbulence parameters. This image is therefore similar to Fig. 2(c). Fig. 2(d) (KBI 1) shows a Knowledge Based Image, which is a combination of the parameter settings of KBI 2 and KBI 3.

and Bandwidth Imaging, indicates that Knowledge Based Imaging can be used to find an optimal imaging method that compromises these two extremes.

KBI 1 is shown in Fig. 2(d). KBI 1 is a mixture of these two extreme ways of setting parameters of Knowledge Based Imaging. Here the velocity, velocity distributions and clutter parameter are the same as for KBI 3 and the power settings are the same as for KBI 2. This gives hope for finding an optimized imaging setup of Knowledge Based Imaging that balances the advantages of Bandwidth Imaging and Fundamental Imaging.

5 Conclusion

Knowledge Based Imaging is proposed as a Doppler-based method to distinguish left-ventricular blood pool from myocardial wall in echocardiographic images. A computer simulation is used to outline differences in how Knowledge Based Imaging, Bandwidth Imaging and Fundamental Imaging classify in various types of noise. Fundamental Imaging classifies well in environment where tissue to blood signal ratio is high and clutter to white noise ratio is lower than tissue to white

noise ratio. Knowledge Based Imaging classifies also well in this environment. In addition Knowledge Based Imaging classifies well as long as blood to white noise ratio is above 30 dB, regardless of the clutter to white noise ratio and the tissue to blood signal ratio. This motivates for a better tissue differentiation in apical areas.

Moreover, Bandwidth Imaging classifies similar to Knowledge Based Imaging, but blood to white noise ratio has to be 20 dB higher to get the same value of apparent error rate. Also, the simulations show that the optimal filter coefficient prior to the autocorrelation estimate is linearly dependent of blood to white noise ratio and clutter to white noise ratio. This argues for the linearly dependent filter coefficient suggested in [1].

A few images of Knowledge Based Imaging are supplied in this paper, showing that Knowledge Based Imaging can be adjusted to look similar to both Fundamental Imaging and Bandwidth Imaging.

Finally, we acknowledge that more optimization and research are needed for a clinical valuable implementation of Knowledge Based Imaging. First, the implementation should be real time, and the challenges here are the maximizations in equation (12) or integrations in equation (10). In the case of maximisations in equation (12), the maximizations could be done by a Preconditioned Conjugate Gradient Method.

Second, the box constraints of Knowledge Based Imaging have to be set everywhere in the image. To some degree they could be found. The level of white noise could be measured, while the transmitter is turned off. The velocity and turbulence parameters in tissue and blood could be found from a priory knowledge. Further, the signal characteristic could potentially be estimated by for instance a Levenberg-Marquardt method with box constraints [11]. Also, the potential of manual adjustment of parameters may also be investigated.

References

1. Hovda, S., Rue, H., Olstad, B.: Bandwidth of the ultrasound doppler signal to distinguish blood from tissue signal in the left ventricle. In: Not Submitted. (2007)
2. Angelsen, B.A.: 7.4 ,9,3 , 10.4. In: Ultrasound Imaging Wawes, Signals and Signal Processing. Emantec, Trondheim, Norway (2000)
3. Torp, H.: Clutter rejection filters in color flow imaging a theoretical approach. IEEE Transactions on Ultrasonics, Ferroelectriscs. and Frequency Control **44** (mar 1997) 417–424
4. Torp, H., Kristoffersen, K., Angelsen, B.A.J.: Autocorrelation techniques in color flow imaging: Signal model and statistical properties of the autocorrelation estimates. IEEE Transactions on Ultrasonics, Ferroelectriscs. and Frequency Control (1994)
5. Heimdal, A., Torp, H.: Detecting small blood vessels in colorflow ultrasound imaging¿ a statistical approach. IEEE Transactions on Ultrasonics, Ferroelectriscs. and Frequency Control (1999)
6. Angelsen, B.A.J.: A theoretical study of the scattering of ultrasound from blood. IEEE Trans. Biomed. Eng. **27(2)** (Feb 1980) 61–67

7. Schoephoerster, C., Chandran, K.B.: Velocity and turbulence measurements past mitral valve prostheses in a model left ventricle. Journal of Biomechanics **24**(7) (1991) 549–562
8. Trees, H.L.V.: Detection, Estimation, and Modulation Theory. Volume 1. John Wiley and Sons, Inc. (1968)
9. Johnson, R.A., Wichern, D.W.: Applied Multivariate Statistical Analysis. Prentice-Hall Inc (2002)
10. Spencer, K.T., Bednarz, J., Rafter, P.G., Korcarz, C., Lang, R.M.: Use of harmonic imaging without echocardiographic contrast to improve two dimensional image quality. American Journal of Cardiology **82(6)** (1998) 794–799
11. An, L.T.H., Tao, P.D.: A branch and bound method via d.c. optimization algorithms and ellipsoidal technique for box constrained nonconvex quadratic problems. Journal of Global Optimization **13**(2) (September 1998) 171–206